The low field, magnetoresistivity tensor and the fermi surface of arsenic

Alan Paul Jeavons

THE LOW FIELD, MAGNETORESISTIVITY TENSOR AND THE FERMI SURFACE OF ARSENIC.

A thesis by

Alan Paul Jeavons B.Sc.(Dunelm)

in candidature for the degree of Doctor of Philosophy at the University of Durham

June 1969

Department of Applied Physics and Electronics

University of Durham

ACKNOWLEDGMENTS

I am greatly indebted to Dr. G. A. Saunders for initially planning this research topic and enthusiastically and financially guiding its progress.

My grateful thanks also go to Professor D. A. Wright for providing many facilities; to Mrs. S. Jobling for most cheerfully and efficiently typing this thesis, despite my somewhat erratic presentation of material; to Miss. C. Guyll for her meticulous preparation of the diagrams; and to the technical staff led by Mr. F. Spence for their most friendly and invaluable service: in particular I wish to mention Mr. R. Waite and Mr. P. Wilson.

I am grateful to the Science Research Council for financial support.

Finally, I thank my wife, for her understanding and patient help in many ways.

ABSTRACT

A technique has been developed for growing large, strain-free, single crystals of the rhombohedral (α) semimetallic form of arsenic from the vapour phase. Previously, only small crystals have been obtained: large crystals can only be grown when the deposition temperature is above a critical value of 700^{o}C. Temperature fluctuations must be kept within 0.2^{o}C to prevent the development of a severe mosaic structure. Dislocations have been examined by etching techniques. Due to the 'puckered layer' structure of arsenic, either trigonal or hexagonal pits may be produced at the same site of emergence of dislocations on the (111) cleavage plane; the etch determines the pit shape.

Galvanomagnetic effects in arsenic have been studied for the low-field condition $\mu H << 1$ by systematically measuring the twelve coefficients that define the isothermal magnetoresistivity tensor to second order in magnetic field, at selected temperatures between 77^{o}K and 305^{o}K. Because the effects are small, their measurement requires certain experimental refinements: the measuring system has a resolution of 10^{-9}V; electronic systems have been

designed to stabilize a sample current of 5 amps. to 1 in 10^6 and the sample temperature to $0.001^{\circ}K$.

A two carrier, multivalley ellipsoidal model of the energy bands of arsenic is invoked to interpret the galvanomagnetic measurements and so determine carrier densities and mobilities and tilt angles of the Fermi ellipsoids. To solve the consequent twelve equations in nine unknowns, a new method of computation, incorporating a least-mean-squares criterion, has been devised. The electrons are sited in pockets tilted at $+82^{\circ}$ to the trigonal axis and holes in pockets tilted at $+40^{\circ}$; equal carrier densities are essentially temperature independent, ranging from 1.9×10^{20} cm.$^{-3}$ at $77^{\circ}K$ to 2.1×10^{20} cm.$^{-3}$ at $305^{\circ}K$. These findings are in close agreement to recent theoretical calculations and measurements of the de Haas-van Alphen effect. Carrier mobility temperature dependences are close to $T^{-1.7}$, considerably greater than the expected $T^{-1.0}$, probably owing to intervalley scattering.

A measurement of the two components of the thermoelectric-power tensor has shown that S_{33} is negative, not positive, as reported previously.

CONTENTS Page

CHAPTER I.

INTRODUCTION

I.1. Arsenic : Biological Aspects 1

I.2. Narrow-gap Semiconductors

a. Infra-red lasers 2

b. Refrigeration and energy conversion 3

I.3. The Group V Semimetals

a. Basic electronic structure 3

b. Galvanomagnetic effects 4

I.4. Thesis Content 7

CHAPTER II.

THE CRYSTAL AND BAND STRUCTURE OF ARSENIC

II.1. Crystal Structure

a. Derivation from the cubic lattice 9

b. The three symmetry axes 13

c. Pseudo-symmetry 15

d. The puckered layer structure 15

e. The Brillouin zone 17

II.2. The Fermi Surface of Arsenic 19

Page

CHAPTER III

GROWTH AND EXAMINATION OF ARSENIC SINGLE CRYSTALS

III.1. Melt Growth 31

III.2. Vapour-Phase Growth

a. Preliminary experiments 34

b. The critical temperature 35

c. The growth furnace 37

d. The silica growth tube 41

e. Experimental details 45

III.3. Crystalline Perfection

a. X-ray examination 47

b. Etch-pits in arsenic 49

c. Slip lines 49

d. Etch-pits - dislocations 53

e. Pit shape 53

CHAPTER IV

THE THEORY OF THE GALVANOMAGNETIC EFFECTS IN ARSENIC

IV.1 Specification of Effects, in Tensor Notation.

a. The isothermal, electrical resistivity tensor 58

Page

b. The isothermal, low field, magnetoresistivity tensor 60

c. The low-field magnetoconductivity tensor 66

IV.2. A Derivation of the Magneto-conductivity Tensor from Band Theory.

a. The Boltzmann equation 69

b. Electrical conductivity in the absence of a magnetic field 71

c. Anisotropic, isothermal, galvano-magnetic effects in arsenic 75

CHAPTER V.

EXPERIMENTAL APPARATUS AND PROCEDURE

V.1. Problems Involved in Measuring the Galvanomagnetic Potentials 86

V.2. The Measuring System

a. General description 89

b. Modifications to the millimicrovoltmeter 91

V.3. Sample Current Control : the Current Regulator 93

Page

V.4. The Temperature Control System

a. Description 96

b. The cryostat 99

c. Resistance thermometer and electrical heater 101

d. Wheatstone bridge 101

e. Amplification (a.c.), phase detection 102

f. The class-D d.c. amplifier 103

g. Operating the temperature control system 110

V.5. Experimental Technique

a. Sample preparation 111

b. The magnet:field alignment 114

c. Field reversals 114

d. Measurement procedure 118

CHAPTER VI.

EXPERIMENTAL CONFIGURATIONS AND RESULTS

VI.1. Crystal Configurations for Determining the Twelve Coefficients 121

VI.2. Details of Calculations 130

VI.3. Experimental Results 135

VI.4. An Assessment of the Two Identities Imposed by the Ellipsoidal Band Model 144

Page

CHAPTER VII

THE COMPUTATION OF THE BAND PARAMETERS AND CARRIER MOBILITIES

VII.1. Previous Methods of Computation

a. Direct solution 153

b. Freedman and Juretschke's technique 154

VII.2. The Least-Mean-Squares Solution

a. Basic method 157

b. Computer programme 160

VII.3. Results

a. Reassessment of the antimony data. 169

b. Application to the arsenic data 170

CHAPTER VIII

GALVANOMAGNETIC EFFECTS AND THE FERMI SURFACE OF ARSENIC

VIII.1. A Comparison between Quantum Resonance and Galvanomagnetic Data 177

VIII.2. Fermi Energies : The Seebeck Effect 182

Page

VIII.3. Carrier Scattering in Arsenic

a. Theoretical considerations 191

b. The validity of an isotropic relaxation time 194

c. The dependence of mobility on temperature 195

VIII.4. Further Observations

a. The Fermi surface 'necks' 200

b. Interband transitions 201

c. Electronic specific heat 201

VIII.5. Conclusion 202

REFERENCES 205

PUBLICATIONS 212

CHAPTER I

INTRODUCTION

I.1 Arsenic : Biological Aspects.

Arsenic, or more exactly arsenic oxide, is poisonous. This fact, known for hundreds of years, has presumably stimulated the interest that has led to the most obscure and macabre investigations (see Mellor 1929): chemical analyses for arsenic content have been reported of all conceivable substances, ranging from sea water 19,500 ft. down off the Azores (Gautier 1903) to remnants of corpses "in great numbers" (Sonnenschein 1869).

The habit of arsenic eating is supposed to prevent decomposition of bodies in the grave. "Many people suppose that the finding of such bodies is the origin of the story of the vampire" (Johnson 1855). Johnson also records that arsenic is eaten, in India, as an aphrodisiac and to heighten feminine beauty; arsenic eaters are peculiarly exempt from infectious diseases, but a sudden cessation of the daily dose is speedily followed by death.

The element, arsenic, has atomic number 33 and belongs to the fifth group of the periodic table. Three allotropic forms are recognised : grey or amorphous, yellow and (semi-)metallic or rhombohedral. This thesis is concerned with a systematic investigation of the anisotropic galvanomagnetic effects in single crystals of semimetallic arsenic, to determine details of the Fermi surface. Some may argue that this is the most obscure investigation of arsenic of all. I hope to show otherwise.

I.2. Narrow-Gap Semiconductors.

Considerable interest in materials with energy gaps close to zero has been aroused by their potential device applications.

(a) Infra-red lasers.

The absorption of electromagnetic waves by the earth's atmosphere shows a 'window' in the wavelength range 8μ-14μ : laser communication techniques are vitally concerned with this infra-red band. The wavelength of a semiconductor injection laser is close to that corresponding to the band edge energy; PbSe (band gap 175 meV) lases at a wavelength of 8.5μ, just inside the atmospheric window. Solid solution systems of PbTe-SnTe and

PbSe-SnSe alloys exhibit a decrease in band gap with increasing tin content; the gap goes through zero for $Pb_{0.65}Sn_{0.35}Te$ and $Pb_{0.865}Sn_{0.135}Se$ (Calawa et al. 1968). These materials afford a means of fabricating tunable infra-red lasers and detectors. Diode lasers have now been constructed from $Pb_{0.73}Sn_{0.27}Te$ to radiate at a wavelength of 28μ (Butler et al. 1966).

(b). Refridgeration and energy conversion.

Generally, charge carrier mobility increases with decreasing band gap (Wright 1959). When both carriers have a high mobility in intrinsic material, the bipolar transport effects become prominent. Thermoelectric and thermomagnetic effects may be enhanced ; refridgeration or energy conversion may be possible. Bi and Bi-Sb alloys have been much studied in this respect (see Harman et al. 1965 a,b).

I.3. The Group V Semimetals.

(a) Basic electronic structure.

By certain distortions (see page 9), the cubic lattice that characterizes the lead-tin chalcogonides is transformed to the rhombohedral A7 structure (point group $\bar{3}m$) of the group V elements arsenic, antimony and bismuth. The unit cell contains two atoms and thus

donates ten electrons to the energy bands. Since there are as many energy states in a band as there are unit cells, and each state accomodates two electrons, it follows that five full bands should exist. Depending on the width of the conduction to valence band gap, insulating or semiconducting electrical behaviour will result. However, the A7 crystal structure produces an indirect band overlap between the fifth and sixth bands: it increases in size for the sequence bismuth, antimony, arsenic. Equal populations of electrons and holes result; in the case of antimony and arsenic they obey degenerate statistics. The three elements are semimetals.

Like the narrow-gap semiconductors, carrier transport in these semimetals is characterised by high mobilities and long relaxation times. In addition to device applications, the semimetals are most suitable for experimental studies of band structure and for testing new aspects of electron transport theory. In bismuth the carriers are particularly mobile and transport effects dramatic: the findings of a large field dependent Hall coefficient and of oscillations in the magnetic susceptibility (de Haas-van Alphen effect) at helium temperatures were signposts to earlier explorers of solid state physics.

(b) Galvanomagnetic effects.

Galvanomagnetic effects in the group V semimetals

are markedly anisotropic and simple energy band models fail to provide a quantitative explanation.

The simplest model is that of spherical energy-wave vector (ε-$\underline{k}$) symmetry for free electrons and holes. If the carrier properties are denoted by densities N, P; effective masses m_e^*, m_h^* and mobilities μ, ν, then a Hall coefficient may be defined (see Ziman 1964):-

$$R = \frac{\sigma_e^2 R_e + \sigma_h^2 R_h}{(\sigma_e + \sigma_h)^2} \qquad (1.1)$$

and transverse magnetoresistance is predicted :-

$$\frac{\Delta\rho}{\rho} = \frac{\sigma_e \sigma_h (\mu-\nu)^2 H^2}{(\sigma_e+\sigma_h)^2 + H^2(\mu\sigma_e+\nu\sigma_h)^2}$$

Here $\sigma_e = Ne\mu$; $\sigma_h = P|e|\nu$; $R_e = \frac{1}{Nec}$; $R_h = \frac{1}{P|e|c}$;

$$\mu = \frac{e\tau_e}{m_e^* c} \; ; \qquad \nu = \frac{|e|\tau_e}{m_h^* c} \; .$$

If there are equal numbers of electrons and holes (N = P) which suffers similar scattering processes ($\tau_e = \tau_h$) and have similar effective masses ($m_e^* = m_h^*$) then $\mu = -\nu$ and $R_e = -R_h$: from equation (1.1), R vanishes. Physically, this is because equal numbers

of electrons and holes are deflected by the magnetic field to the same side of the specimen. Magnetoresistance is essentially positive and vanishes only if $\mu=\nu$, when the sets of carriers behave identically and the system effectively reduces to the one-carrier case.

This model is of limited quantitative application as it fails to explain any anisotropy of conductivity or Hall effect, or the existence of longitudinal magnetoresistance. Some form of non-spherical ε-$\underline{k}$ relationship must be invoked. Some success in explaining the anisotropic galvanomagnetic effects in bismuth resulted from the assumption of single valley ellipsoidal model (Jones 1936). In particular, the large transverse magnetoresistance was explained, but still no longitudinal magnetoresistance was predicted. By tilting the ellipsoids with respect to the $\bar{3}$ axis, a multivalley model is produced because the threefold symmetry is then only satisfied by three, six or twelve ellipsoids for each band. On this basis, quantitative interpretations of the galvanomagnetic effects in bismuth (Abeles and Meiboom 1956) and antimony (Freedman and Juretschke 1961, Epstein and Juretschke 1963)

have resulted. Recently, attention has been concentrated on antimony. Its Fermi surface has been determined experimentally from the de Haas-van Alphen effect (Windmiller 1966) and theoretically from pseudopotential band structure calculations (Falicov and Lin 1966). The galvanomagnetic effects, studied over a wide temperature range, (Oktu and Saunders 1967) fit the predicted model.

Here a detailed study of the galvanomagnetic effects in the remaining element, arsenic, is presented. Previous information is sparse: the resistivity temperature dependence (McLennan et al. 1928) and the anisotropy of resistivity (Bridgman 1932, Taylor et al. 1965) have been measured; magnetoresistance, first looked at by Kapitza (1929), has been examined at helium temperatures (Sybert et al, 1968).

I.4. Thesis Content.

The galvanomagnetic effects have been studied for the low-field condition $\mu H << 1$ by systematically measuring the twelve coefficients that define the isothermal magnetoresistivity tensor to second order in magnetic field (see chapter IV) at selected temperatures between $77^{o}K$ and $305^{o}K$, on single crystals of arsenic grown by a new technique from the vapour

phase (chapter III). Because the effects are small their measurement has required considerable experimental refinements which are described here in detail (chapter V). Results are presented in chapter VI and an improved method of computation of band and mobility parameters is described in chapter VII. Chapter VIII presents a comparison of these parameters to values obtained from quantum resonance experiments and theoretical calculations. But now the nature of Fermi surface of arsenic is discussed.

CHAPTER II

THE CRYSTAL AND BAND STRUCTURE OF ARSENIC

II.1 Crystal Structure.

a. Derivation from the cubic lattice.

Of the three allotropic forms of arsenic, the α-form crystallizes, like bismuth and antimony, in the rhombohedral A7 structure (figure 2.1) of point group $\bar{3}m$ with two atoms per unit cell. This structure is best illustrated by reference to the cubic lattice in the form of two interpenetrating face-centred cells (figure 2.2.). Then lattice symmetry is lowered from cubic to $R\bar{3}m$ by applying two small, but highly significant, distortions.

1. The rhombohedral cell is sheared to reduce the rhombohedral angle α from its cubic value of 60°. This is equivalent to 'stretching' one body diagonal.

2. The atom at the centre of the cell is displaced in the body-diagonal direction by moving the two face-centred cells apart.

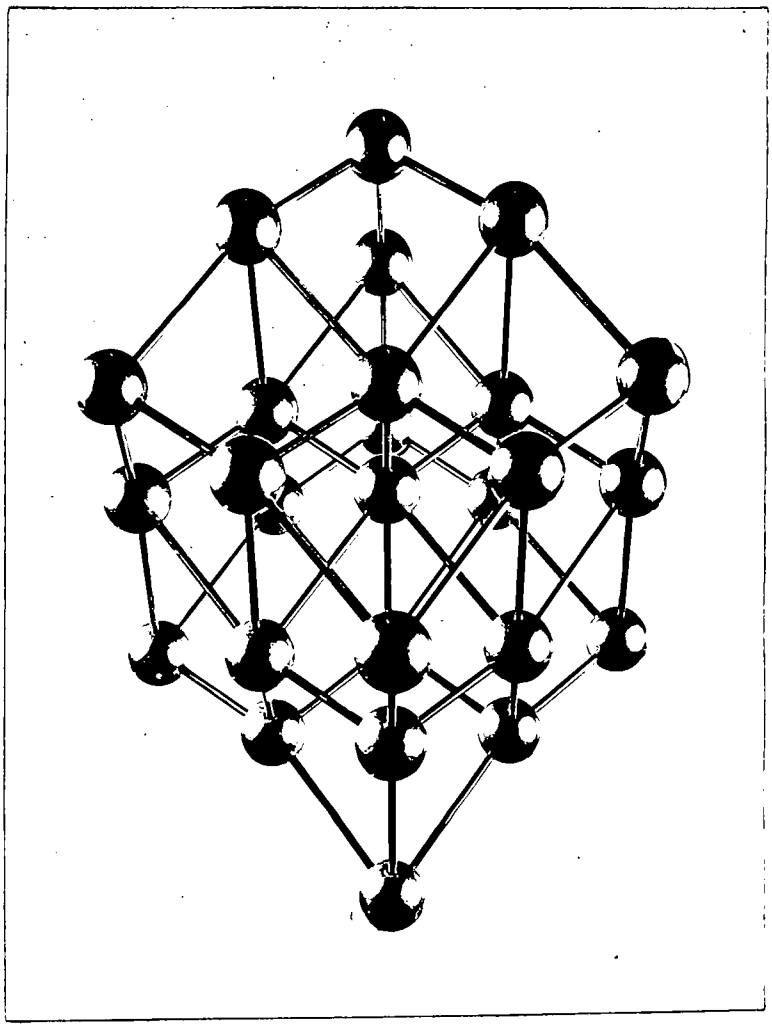

Figure 2.1

The rhombohedral ($\bar{3}$m), A7 crystal structure of arsenic, viewed along the bisectrix (y) axis. 'Puckered layers' are clearly visible.

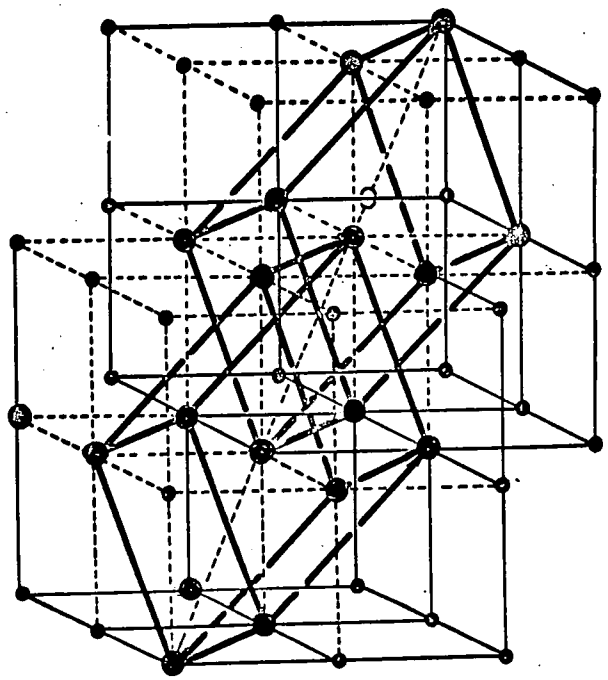

Figure 2.2

The relationship between the cubic lattice and the rhombohedral unit cell of the A7 structure, which is obtained by 'stretching' the body diagonal and displacing the two rhombohedra drawn in heavy lines.

The amount of distortion may be tabulated by:-

1. The value of α (extent of shear).

2. A parameter u, defined as τ/d, which measures the displacement. 2τ is the smaller distance between the interpenetrating cells in the body-diagonal direction and d is the length of the body diagonal.

For the three isomorphous elements, arsenic, antimony and bismuth these two quantities are:-

Element	α	u
As	54° 10'	0.226
Sb	57° 14'	0.234
Bi	57° 7'	0.237
Note: Cubic	60°	0.250

The significance of these distortions is that the {221} planes* now introduce an energy discontinuity in the band structure since their structure factor is no longer zero as it is for the cubic lattice (Mott and Jones 1936). The effect on the electrical properties is most pronounced; Cohen et al. (1964) have shown that the distortions lead to a band overlap and consequently semimetallic electrical conduction.

* The Miller indices refer to the rhombohedron axes.

b. The three symmetry axes.

Certain symmetry elements are retained from the cubic lattice (figure 2.3): three diad (x) axes normal to three mirror planes, mutually orientated at 120°, which intersect in an inversion triad (z) axis: the body diagonal in figure 2.2. Bisectrix (y) axes, one in each mirror plane, complete three orthogonal x-y-z sets, any one of which affords a most convenient Cartesian reference system. The nomenclature is :

Axis	Name	Cartesian System	Numerical System.
Diad	Binary	x	1
In mirror plane	Bisectrix	y	2
Triad	Trigonal	z	3

A useful mnemonic to avoid confusion between binary and bisectrix notation is that the last letter of either name denotes the other axis. The numerical order follows the alphabetic order.

It is significant that the binary axis cannot be chosen uniquely. Two distinct choices exist; each one has three equivalent positions (figure 2.3) The two sets can be distinguished by reference to

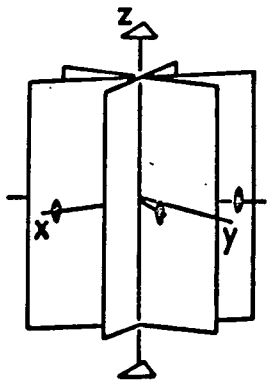

The symmetry elements of the arsenic structure.

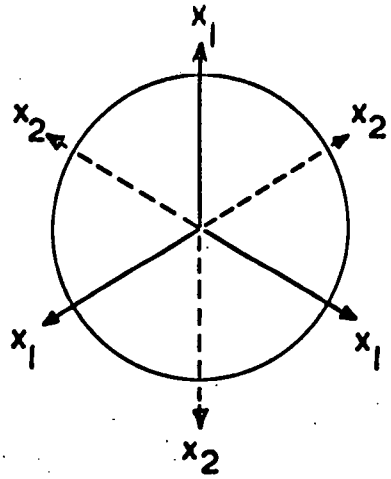

The two choices of binary axis.

Figure 2·3.

the other symmetry elements; this point will be clarified later.

c. Pseudo-symmetry.

Because the A7 structure is so close to cubic, certain directions approximate to the symmetry that they possess in the cubic lattice: they are axes of pseudosymmetry. Figure 2.4 shows an X-ray back reflection Laue photograph taken in the pseudotrigonal direction. It can be seen that care is required to avoid confusion with the trigonal axis. Fortunately, the (111) (x-y) plane cleaves readily to reveal the true trigonal direction.

d. The puckered layer structure.

One further aspect of A7 structure is its approximation to a hexagonal layer structure. Each atom in arsenic has three neighbours at 2.51 Å (the short bond) and three others at 3.15 Å (the long bond) which reflects as a pairing of layers. Each pair can be considered as one puckered, hexagonal

layer; see figure 2.1. For bismuth and antimony, since α is closer to 60^{o}, the long and short bonds are nearly equal and the puckered-layer structure is less marked. This feature is evident from the ease with which arsenic cleaves; bismuth will cleave only with difficulty at liquid nitrogen temperature.

e. The Brillouin zone.

Figure 2.5 shows the first Brillouin zone of the A7 structure; symmetry points and one binary-bisectrix-trigonal system are labelled. Just as the crystallographic structure may be considered as a distortion of the cubic lattice so the A7 Brillouin zone is a distorted form of the face-centred cubic zone; the square faces are now rectangular and only the hexagonal faces perpendicular to the trigonal axis (ΓT) remain regular. ΓK, ΓN are one pair of binary and bisectrix axes; TZLNXUΓ denotes a mirror plane. ΓX and ΓL correspond to the pseudo-four-fold and pseudo-three-fold axes.

The distinction between the two sets of binary axes is now clear: depending on which choice of binary axis is made to form the x-y-z system, either the centre (X) of a rectangular face or the centre (L) of an irregular hexagonal face may lie in the first

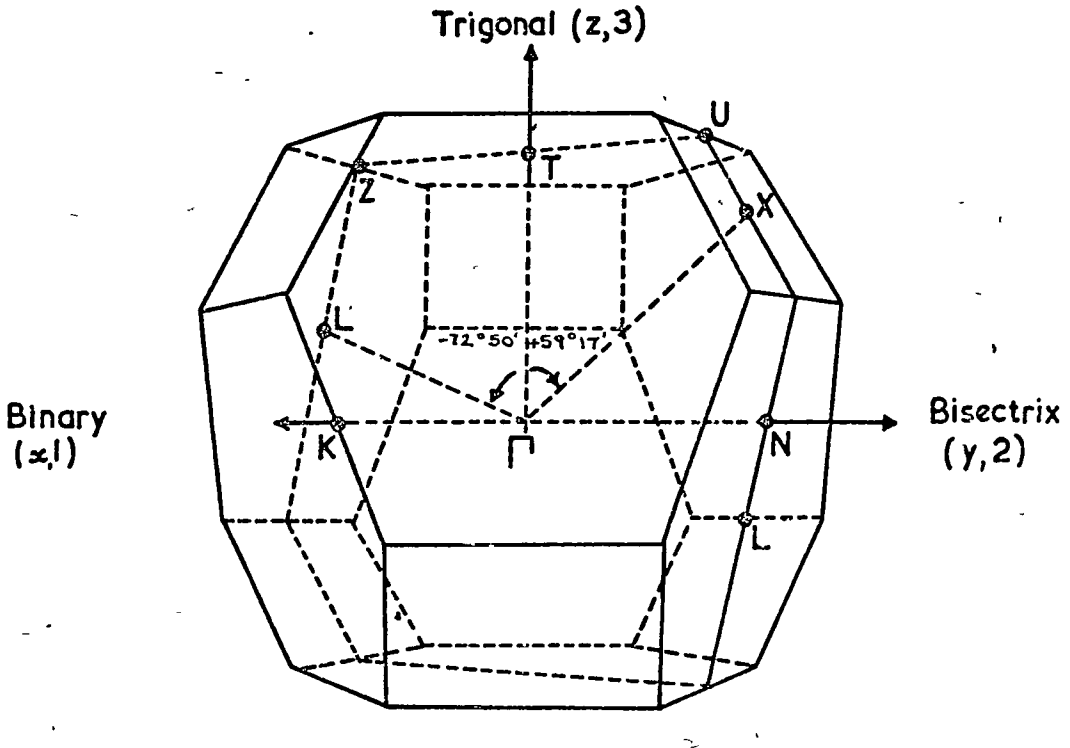

Figure 2.5

The first Brillouin zone of the arsenic lattice. The three axes binary, bisectrix and trigonal form a right-handed orthogonal set; the positive sense of rotation is towards X in the first y-z quadrant.

y-z quadrant. In this work the convention adopted by Windmiller (1966) is followed: the binary axis is chosen to form a right-handed x-y-z system with X in the first y-z quadrant. Then ΓX is at + 59° 17' from ΓT and rotations towards ΓL are negative. The pseudo-symmetry directions ΓX and ΓL may be resolved by X-ray methods to distinguish the choice of binary axis. This point is important as certain galvanomagnetic coefficients have opposite signs for each system as is shown later (page 85).

II.2. The Fermi Surface of Arsenic

Carrier populations in arsenic obey degenerate statistics: only that portion of the band structure close to the Fermi level, namely the Fermi surface, is relevant to this work. As has been shown earlier, an ellipsoidal band model is required to analyse quantitatively the galvanomagnetic effects in arsenic. This means that the Fermi surface should approximate to ellipsoids; their location in the Brillouin zone may be determined by experiment coupled with considerations of crystal symmetry: in general, the Fermi surface must reflect the symmetry of the reciprocal lattice. Detailed pseudopotential and orthogonalised-plane-wave calculations are now available (Falicov

and Golin 1965, Golin 1965, Lin and Falicov 1966). These accord with the results of quantum resonance experiments: the de-Haas-van Alphen effect (Berlincourt 1955, Priestley et al 1967), cyclotron resonance (Datars and Vanderkooy 1966) and ultrasonic attenuation (Ketterson and Eckstein 1965); the essential features of the Fermi surface are established. There are three electron pockets centred on each L point in the Brillouin zone and a multiply-connected hole surface around T.

Electron surface.

Each electron pocket can be considered as a prolate ellipsoid. One principal axis is parallel to the binary direction and the other two lie in the mirror plane. One of these is the longest axis; it is tilted away from the trigonal axis, ΓT, by approximately $+80^{\circ}$. Figure 2.6 shows a cross-section with the mirror plane. Table 2.1 (from Priestley et al. 1967) summarises the experimental to theoretical agreement. Some deviation from ellipsoidal shape is apparent in that planes of minimum and maximum area are not exactly perpendicular.

The Hole Surface.

This surface, called a "crown" (figure 2.7), may be thought of as six carrot-shaped pockets joined by six

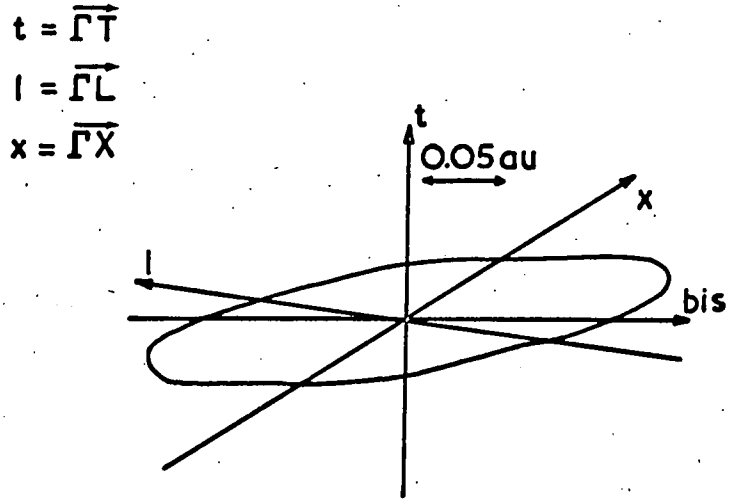

Figure 2·6. A cross section of an electron pocket with the mirror plane (after Lin and Falicov 1966)

Table 2.1

Details of the Electron Fermi Surface of Arsenic

	De Haas-van Alphen Effect (Priestley et al)	Pseudopotential Calculation (Lin and Falicov)
Number of pockets	3	3
Location of Brillouin zone	L or X	L
Tilt in yz plane for:		
(a) minimum area	$+86.4 \pm 0.1^{\circ}$	$\sim +80^{\circ}$
(b) maximum area	$+171.0 \pm 0.2^{\circ}$	$\sim +171^{\circ}$
Minimum area for H in yz plane	$(5.695 \pm 0.005) \times 10^{-3}$	5.5×10^{-3}*
Area for H $\parallel$ to x (binary)	$(2.050 \pm 0.007) \times 10^{-2}$	1.8×10^{-2}
Area for H $\parallel$ to z (trigonal)	$(2.088 \pm 0.005) \times 10^{-2}$	1.6×10^{-2}
Total number of electrons	$(2.12 \pm 0.01) \times 10^{20}$ cm^{-3}	
	$(4.60 \pm 0.05) \times 10^{-3}$ per atom	

* The electron Fermi energy was fitted to this value.

continued.

Table 2.1 (continued).

	De Haas-van Alphen Effect (Priestley et al)	Pseudopotential Calculation (Lin and Falicov)
Principal effective masses in ellipsoidal approximation		
(a) along binary axis	0.163	0.11
(b) in yz plane	0.105	0.038
	2.11	0.94
Fermi energy (Ry)	0.0140**	0.0270

** Derived in a parabolic approximation.

thin cylinders or "necks". Each pocket and neck is bisected by a mirror plane. The main pocket is tilted by about $+40^{o}$ away from the trigonal axis and the necks by -10^{o}. Cross sections of the "crown" are shown in figure 2.8 and experimental-theoretical agreement is shown in table 2.2. It is clear that the hole pockets deviate considerably from ellipsoids.

The volume of each main hole pocket is one half that of an electron ellipsoid. The volume of each neck is about 1% of the main hole pocket.

Figure 2.9 is a photograph of a simplified model of Lin and Falicov's surface - three electron ellipsoids and six hole ellipsoids - used in this work to analyse the low field galvanomagnetic effects. In chapter IV equations are derived connecting this model to the twelve coefficients that define the magnetoresistivity tensor. Before this, the method of growing single crystals of arsenic is described.

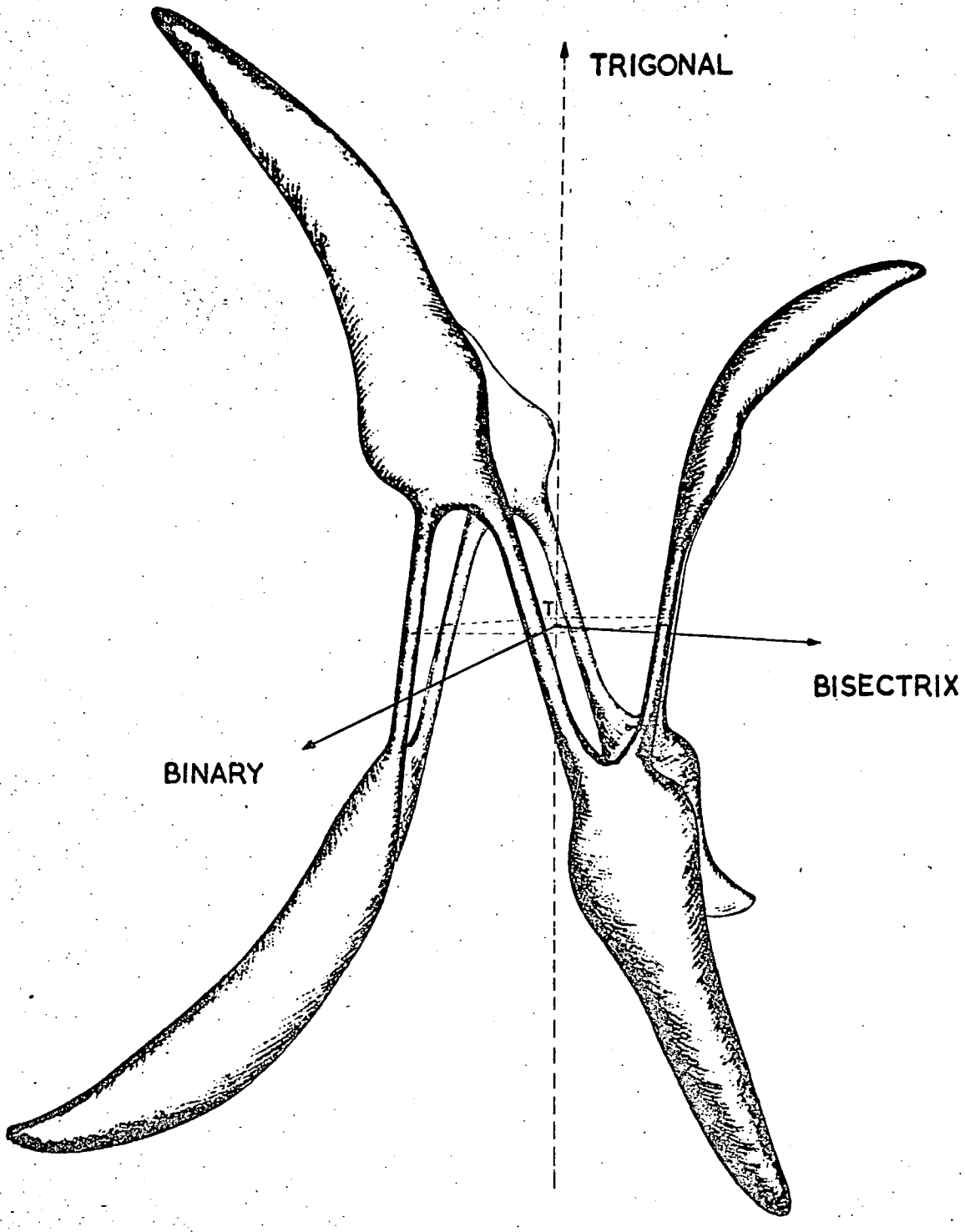

Figure 2.7

The hole surface or 'crown' of arsenic. It is centred on the T point of the Brillouin zone (after Lin and Falicov 1966).

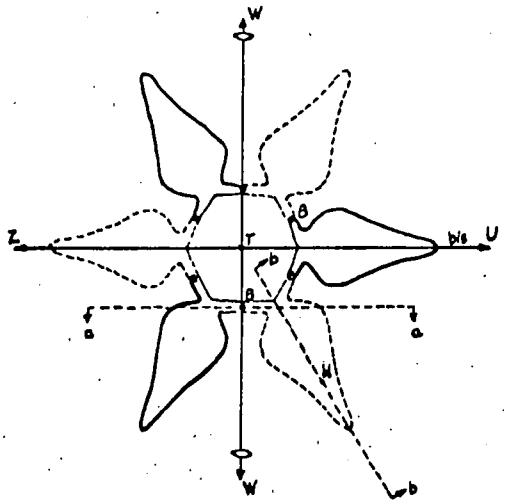

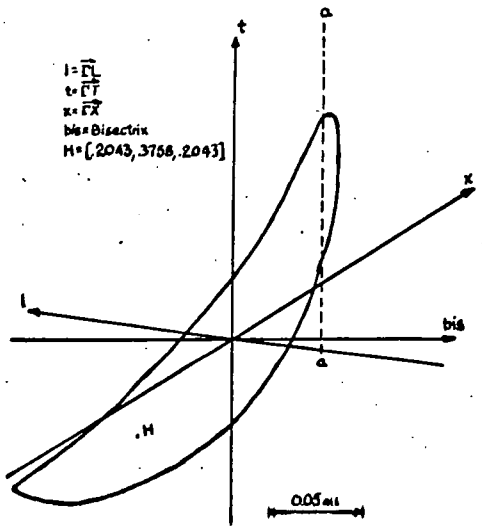

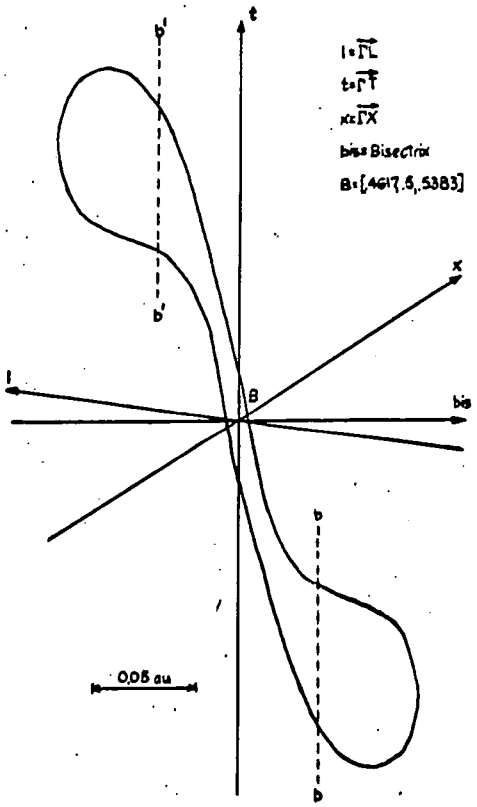

Figure 2·8. Various cross sections of the hole pockets (after Lin and Falicov 1966)

Table 2.2.

Details of the Hole Fermi Surface of Arsenic

	De Haas-van Alphen Effect (Priestley et al)	Pseudopotential Calculation (Lin and Falicov)
(1) 'Necks'		
Number :	6	6
Location in BZ	on binary axis through Γ or T	on binary axis through T(TW)
Tilt from ΓT in yz plane	-9.6 ± 0.1^{o}	$\sim -11^{o}$
Minimum area	$(6.87 \pm 0.02) \times 10^{-5}$	6.9×10^{-5}*
Minimum effective mass	0.028 ± 0.001	
Fermi energy (rydbergs)	7.8×10^{-4}**	

* The Fermi energy for holes was adjusted to fit this value.

** Derived in a parabolic approximation.

continued.

Table 2.2 (continued.)

	De Haas-van Alphen Effect (Priestley et al)	Pseudopotential calculation (Lin and Falicov).
(2) Main Pockets		
Number:	6	6
Location in BZ	in mirror plane through Γ and T	near T in mirror plane through Γ and T.
Minimum area in yz plane	$(3.981 \pm 0.004) \times 10^{-3}$	difficult to calculate.
Tilt angle of minimum area	$+37.25 \pm 0.1^{o}$	$\sim +44^{o}$
Fermi energy (Ry)	0.013**	$\sim$ 0.0266

** Derived in a parabolic approximation.

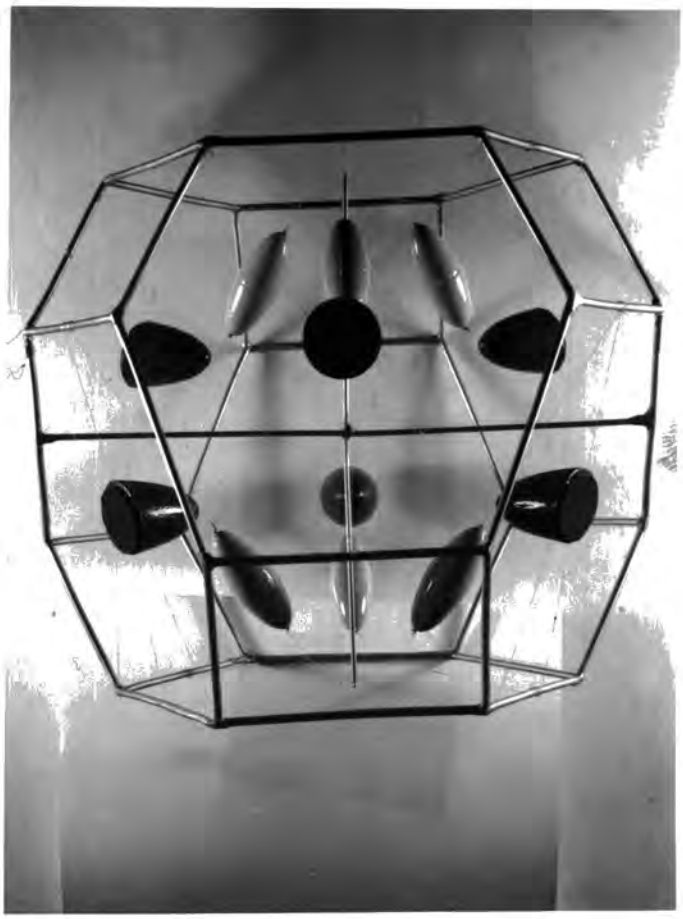

Figure 2.9a.

The ellipsoidal approximation to the Fermi surface of arsenic, used in this thesis to analyse the low-field galvanomagnetic effects. The photograph is taken in the bisectrix direction. The six half ellipsoids (dark colour) are the electron pockets and the six full ellipsoids (light colour) are the hole pockets. Surfaces are not ellipsoids of revolution.

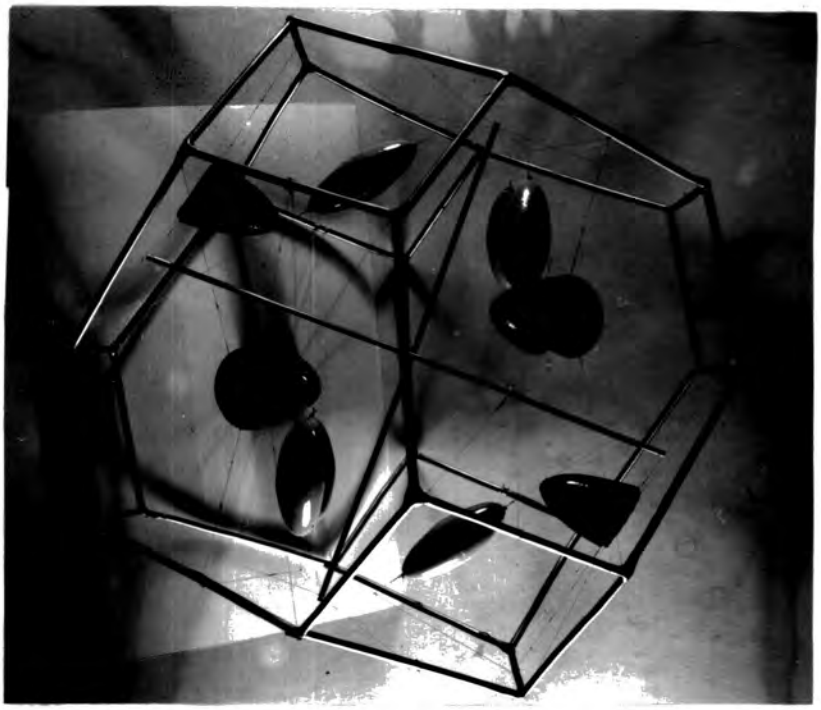

b. Photograph taken along the binary axis

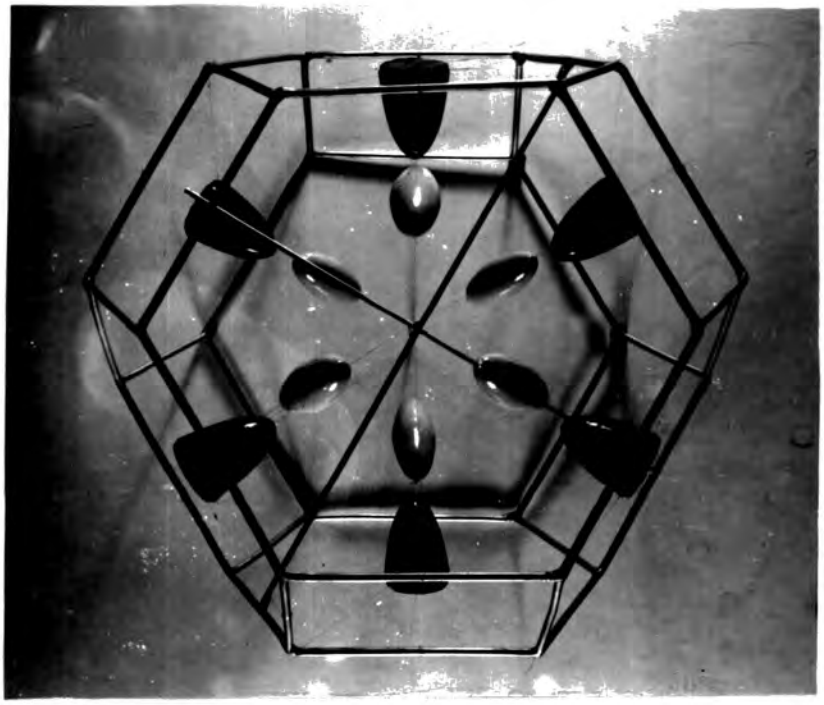

c. Photograph taken along the trigonal axis.

Figure 2.9.b,c.

Further views of the ellipsoidal Fermi surface.

CHAPTER III

GROWTH AND EXAMINATION OF ARSENIC SINGLE CRYSTALS

III.1 Melt Growth.

Work on arsenic has been hindered generally by the difficulty of growing single crystals. The usual Bridgman technique (Brice 1965a) is not straightforward as arsenic sublimes readily: its triple point is at 817°C under a pressure of 35 atmospheres (figure 3.1) i.e. this pressure, at least, is needed before melting can occur. Kapitza (1929) seems to have been the first to obtain an arsenic crystal from the melt. He melted arsenic, sealed in a silica capillary tube, with a bunsen burner and withdrew the tube slowly from the flame - "taking the necessary precautions to prevent poisoning by the arsenic vapours in case the tube exploded" - to grow a single crystal rod. Bridgman (1932) applied his crystal-growing method to arsenic and grew crystals 3mm. in diameter: like Kapitza, from the melt under pressure. More recently,

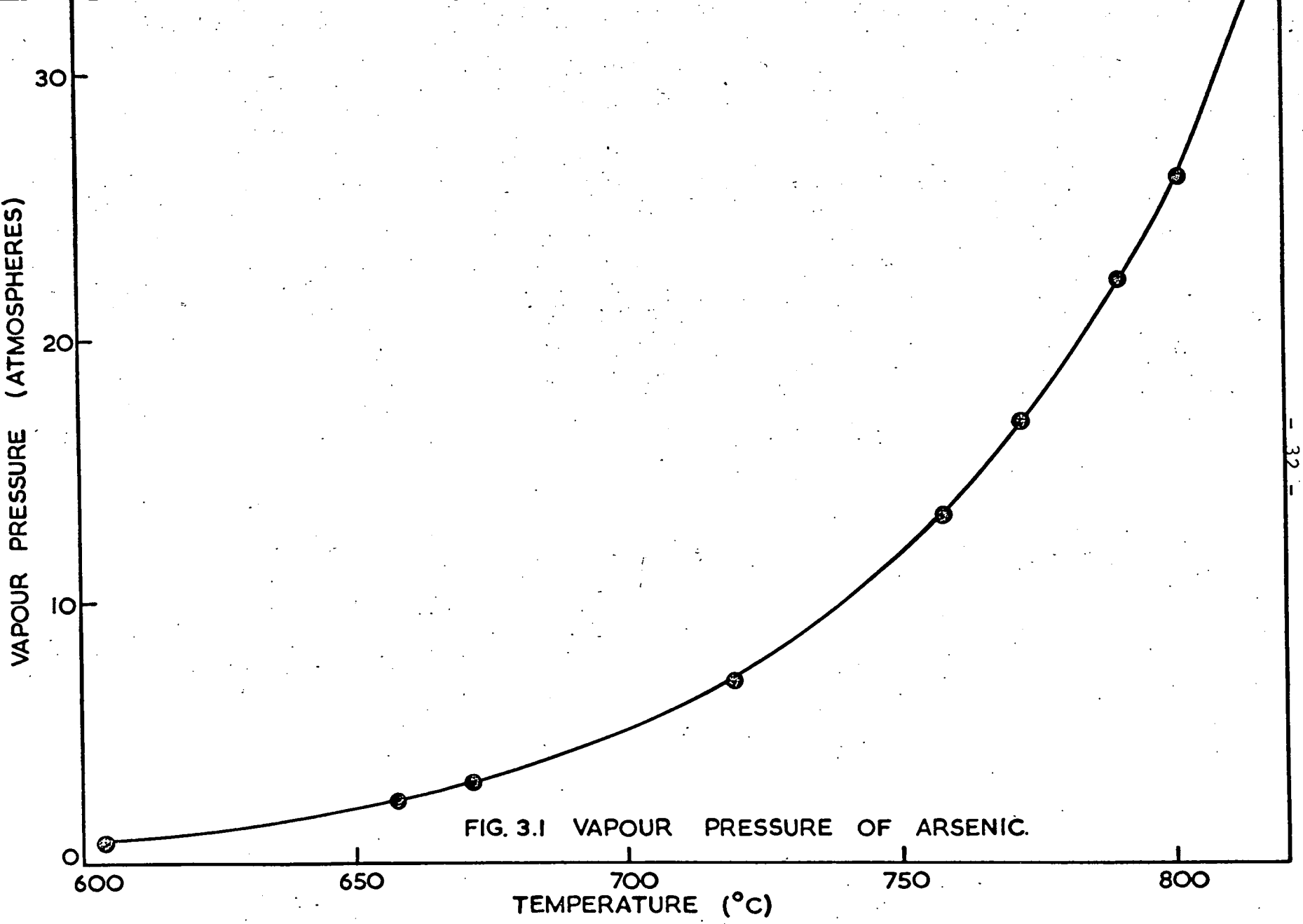

FIG. 3.1 VAPOUR PRESSURE OF ARSENIC.

(Weisberg et al. 1963, Taylor et al. 1965, Saunders and Lawson 1965) crystals up to 1 cm. in diameter have been grown in this way.

There are three serious disadvantages to growing arsenic crystals from the melt:-

1. Arsenic expands on freezing, and crystals grown in a rigid container are badly strained.

2. Only one crystallographic orientation usually results: the (111) plane parallel, or nearly so, to the crystal length (Bridgman 1932, Weisberg et al. 1963).

3. To withstand the pressure of 40 atmospheres or more involved, the wall thickness of the containing tube should be at least half the bore. A wall thickness of 5 mm. i.e. a crystal diameter of 1 cm. is a practical maximum.

A method of overcoming the problem of strain has employed a heavy walled silica "bomb" with a conical growth region (Ketterson and Eckstein 1965). Expansion on freezing is then possible; the crystal is able to "slide up" the conical wall. But the manufacture of such a container is highly specialised, and the cost prohibitive, particularly in view of its once-only use.

The second and third disadvantages are also

serious. In order to measure a full set of galvano-magnetic coefficients, at least one sample orientated with its length perpendicular to the (111) plane is required, (see p. 125). The restriction on the orientation that may be grown means that such a sample can be obtained only by cutting diametrically across a crystal boule. The maximum boule diameter, and therefore sample length, is 1 cm. and requirements of sensitivity and mechanical strength necessitate samples at least 2 cms. long. The only way to resolve this dilemma for melt-growth would probably be to use a liquid encapsulation technique, (Metz et al. 1962) and grow larger crystals inside a steel pressure chamber. As a much simpler alternative, growth from the vapour phase has been investigated. The problem of strain is immediately overcome and, if growth could be effected at temperatures 50°C or more below the triple point, bigger crystals could be obtained using thinner-walled,silica tubes at the considerably reduced vapour pressures (10 atm. at 740°C) involved (figure 3.1).

III.2 Vapour-Phase Growth.

a. Preliminary experiments.

Despite the ease with which arsenic sublimes,

until now, only small crystals have been grown from the vapour phase (McLennan et al. 1928, Berlincourt 1955). However, both workers reported that crystal size increases as the deposition temperature is increased. In one case (McLennan) the biggest crystal formed at an accidental cool spot inside the furnace.

An experiment was performed to examine systematically the effect of growth temperature on crystal size. A ten gram sample, sealed in vacuo in a pointed silica tube was lowered at 3 mm/hr. from a high temperature 'plateau' region in a furnace. Several runs were made; the plateau temperature was increased from 500°C to 750°C in steps of 50°C. Initially a polycrystalline mass was obtained, of about 1 mm^3 average grain size. Growth was very disordered, extending up the tube; lateral growth was incomplete. Grain size and lateral growth increased with temperature, the former to about 10 mm^3 at 650°C. At 700°C a sharp change to single crystal growth occurred. Lateral growth was now complete and crystal facets had formed at the tail.

b. The critical temperature.

The occurrence of a critical temperature for

ordered growth is well known, for instance in metal crystals (Keepin 1950) and in pyrolytic graphite (Blackman et al. 1961) and for epitaxial deposition. Single crystal growth upon a substrate will occur, if the freshly deposited atoms forming a monolayer are hot enough, and thus sufficiently mobile, to migrate to surface kink sites before the next monolayer condenses (Burton et al. 1951). The time available for migration is dependent on the growth rate. Thus to form a single crystal at a given growth rate the substrate must attain a sufficiently high temperature. An Arrhennius relationship (Burton et al. 1951) applies:-

$$R_g = C \exp\left(- Q/RT_c\right)$$

Here R_g is the growth rate and T_c the critical, substrate temperature. Q is the activation energy for surface diffusion and R is the gas constant.

This simple model has been verified experimentally for the epitaxial deposition of germanium (Krikorian and Sneed 1966). They found that "neither the deposition techniques, nor the deposition conditions used to control the growth rates have a significant influence on the results. A qualitative model based purely on the relation

between growth rate and surface mobility appears to be sufficient to describe the growth rate-epitaxial temperature relation".

A brief attempt was made to test the formula in the case of arsenic deposition by repeating the previous experiment with the growth rate changed to 0.6 mm/hr. No change in critical temperature greater than 10-20°C (the experimental accuracy) was found.

A reliable method for growing large single crystals has been developed following the finding of a critical temperature. It is now described.

c. The Growth furnace (figure 3.2)

The furnace consists of a well-insulated mullite tube 70 cm. long, 4 cm. bore, mounted vertically inside a rectangular sindanyo box, and wound with four adjacent heater windings of 22 S.W.G. "Kanthal" wire. Each winding covers 15 cms. of the tube, has a resistance of 100 ohms, and is independently fed from the mains via a "Regavolt" rotary transformer to facilitate wide adjustment of temperature profile. Low cost A.C. ammeters were not available; for economy, four small A.C. voltmeters (Japanese "Sew") were converted to monitor the current in each winding. Smooth lowering of the sample is

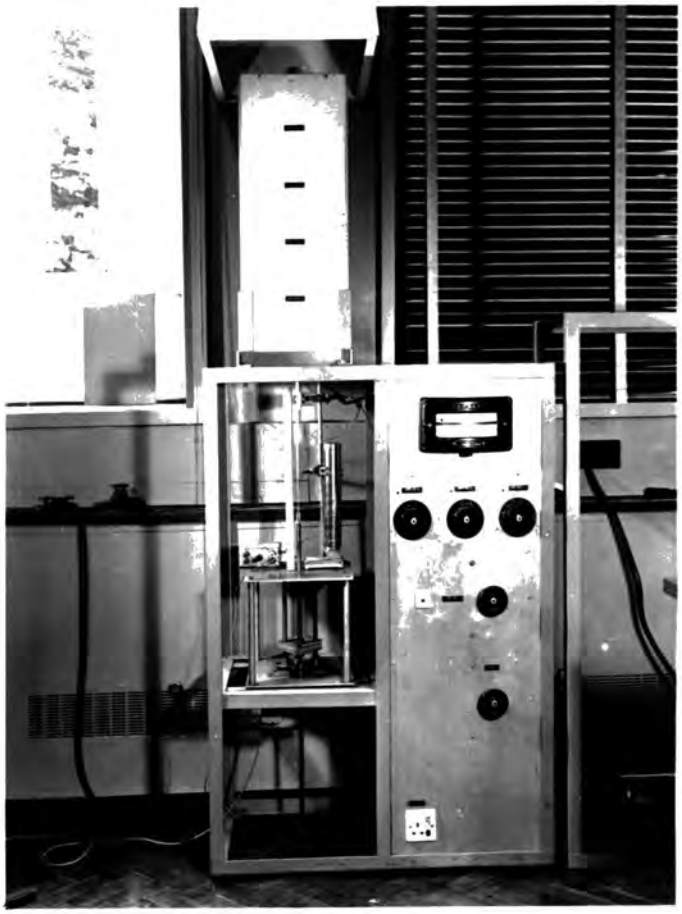

Figure 3.2

The furnace used for growing single crystals of arsenic.

effected by means of a support rod clamped to a platform driven down by three geared, motor rotated screw legs. Temperature is controlled at one adjustable position in the furnace with an 'on-off' galvanometer controller (Ether type 991) using a Pt - Pt/13%Rh thermocouple. The first crystals grown possessed a severe mosaic structure that proved to be due to thermal fluctuations during growth (see page 51). Hence the following refinements to the furnace:-

1. 'Gouy' modulation (Reid 1941) is incorporated into the temperature controller. In this system, low frequency (0.1 - 1.0 Hz) A.C., injected into the thermocouple circuit, from a transistorised multivibrator, pulses the galvanometer pointer by some 5°C about the mean temperature, switching the furnace on and off as the control point is traversed. The ratio of on to off times, longer or shorter depending on whether the mean temperature falls short of or exceeds the control point, determines the mean power reaching the furnace. Proportional control ensues; thermal inertia and galvanometer pivot friction are largely overcome. Temperature stability is improved from $\pm$ 1°C to $\pm$ 0.1°C at 800°C. For much useful detail on this method see

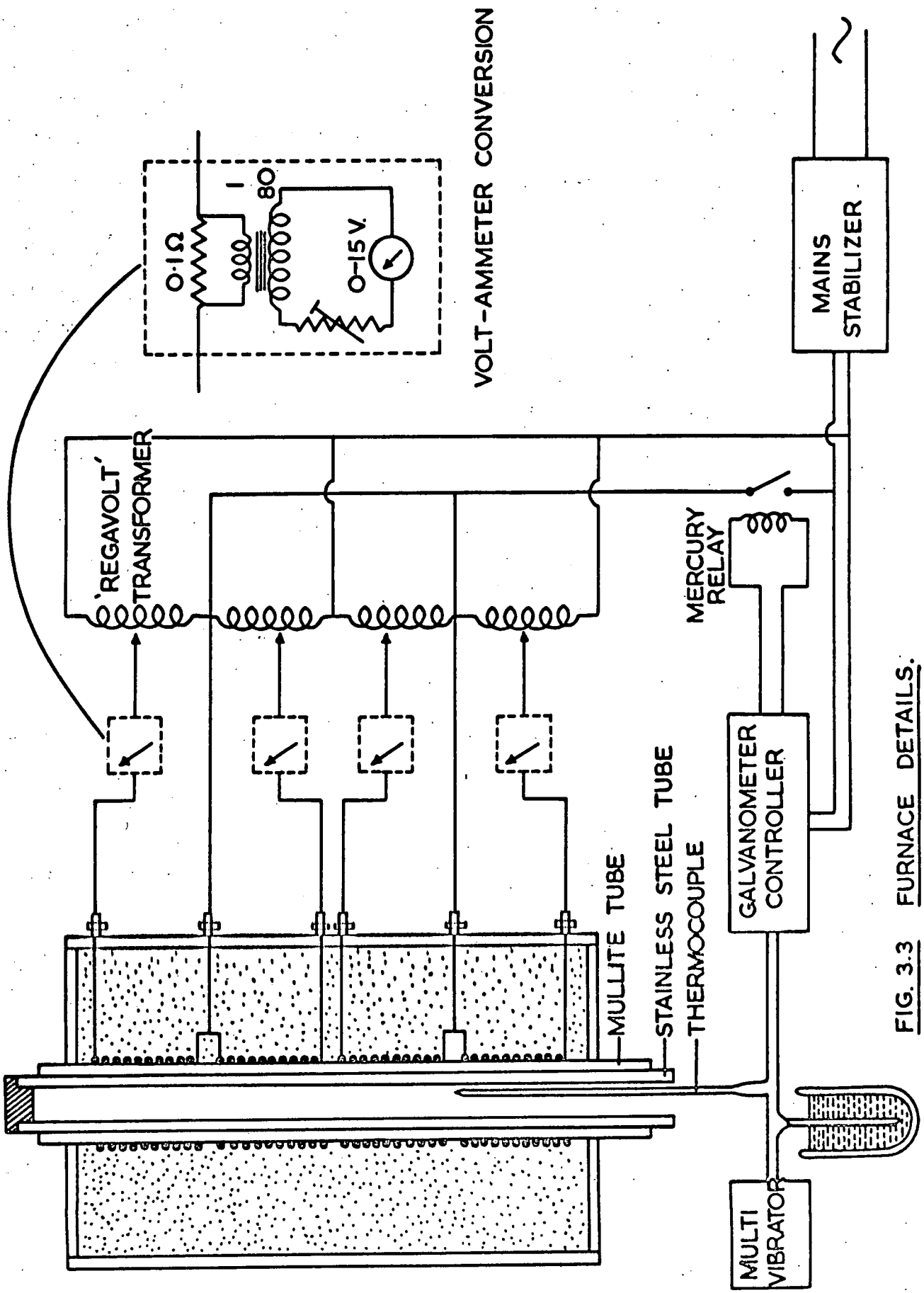

FIG. 3.3 FURNACE DETAILS.

Goodman (1966) and Jewell (1967).

2. The cold junction of the thermocouple is immersed in oil in a Dewar flask for stability.

3. A mains stabiliser (Servomex AC2 MkIII) is used.

4. A thick stainless steel liner is fitted to the mullite tube to smooth any temperature undulations between the heater turns.

Figure 3.3 illustrates the furnace details.

d. The silica growth tube (figure 3.4)

The tube has dimensions: length 30 cm., internal diameter 2.0 cms., and wall thickness 1.5 mm. A simple pointed end does not seed successfully because contact with the steel support rod destroys the temperature gradient at the tip and several longitudinal crystals develop. Therefore a 2 cm. length of 3 mm. diameter quartz rod is fused to the tip as a spacer, and the tube is constricted near the bottom for single seed selection (Brice 1965b). A B24 silica cone provides a demountable connection to a pyrex-glass vacuum system. Three stages of cleaning were used:-

1. A general cleaning for 3 hours in 1:1 hydrofluoric/nitric acid.

Figure 3.4

The silica growth tube.

2. 20 minutes in concentrated (48%) hydrofluoric acid, recommended by Weisberg (1963) to reduce silicon impurity in the crystal.

3. Baking for 24 hours at 900°C and 10^{-5} mm. of mercury.

Sealing the wide bore growth tube posed a problem as it could not be 'necked' before evacuation else the arsenic charge could not be loaded. And to avoid contamination and oxidation the arsenic charge could not be powdered. A procedure previously used in growing gallium arsenide (Brice 1965c) was adopted.

A blank containing air at atmospheric pressure is formed by closing both ends of a silica tube of length 8 cm. and diameter a close fit inside the growth tube. The blank is placed inside the tube at the desired sealing point and the tube evacuated. The seal is effected by heating a band of the tube so that it collapses onto the blank. At the same time, the blank expands as the air pressure inside it increases. It is desirable to heat strongly at one point once a preliminary seal has been made, until the blank and tube puncture. Then the pressure in the blank remains at atmospheric and the seal may be consolidated and annealed without any undesirable

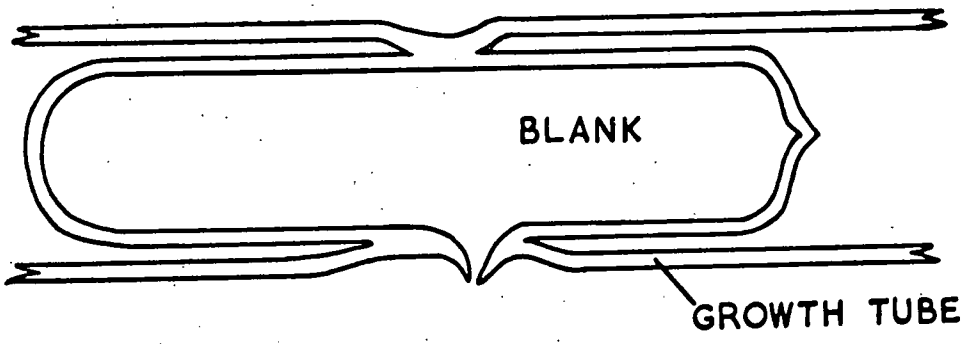

Figure 3·5. Sealing the growth tube.

thinning occurring. See figure 3.5.

e. Experimental details.

50 gms. of 99.9995% purity arsenic (Johnson and Matthey Grade I), followed by the blank are tipped into the tube. Heating to 300°C under vacuum for 3 hours distils off any volatile oxide present; the tube is sealed, and then the cone removed by cutting with a diamond wheel. The growth furnace temperature profile, shown in figure 3.6, has two major features, a 'hump' and a 'plateau'. The tube is sited with its tip just above the hump, so that the arsenic charge sublimes to the cooler, upper part of the container, where it adheres to the glass. The plateau is vital. It maintains the bulk of the tube at a fairly uniform temperature to disperse the charge and prevent the formation of a plug which subsequently fractures the tube on expanding. Crystals grow by progressive condensation, as the tube cools on the lower side of the hump. The growth rate was 0.6 mm/hr, as slow as practical to minimise the critical temperature ; probably a faster growth rate could be tolerated (see earlier discussion on the critical temperature). A 50 gm. crystal 2 cms. in diameter and 5 cms. long may be grown in about seven days.

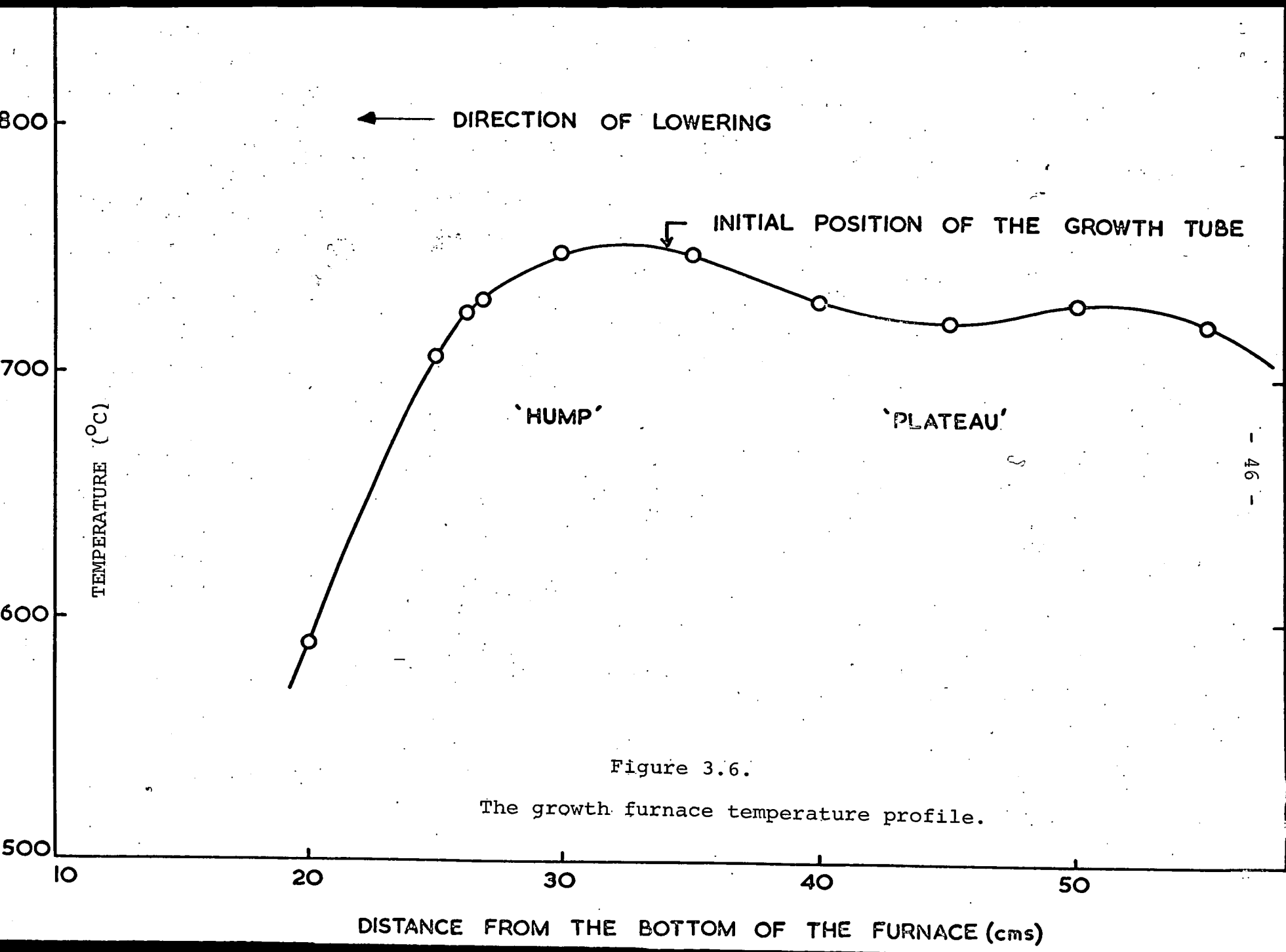

Figure 3.6.

The growth furnace temperature profile.

III.3 Crystalline Perfection.

Three types of crystal were examined by X-ray and etch-pit techniques:-

1. Melt-grown.
2. Early vapour grown.
3. Final vapour grown.

a. X-ray examination.

Figure 3.7 shows X-ray, back reflection Laue photographs, taken perpendicular to the (111) plane, of the three classes. The spreading of the spots in figure 3.7a illustrates severe strain due to bending of the (111) plane. Indeed kinks and bumps were easily visible to the eye on melt-grown crystals. In figure 3.7b there is little spreading, but now splitting of the spots, typical of a mosaic structure. In this case, instead of a curved crystal face a patchwork of relatively strain-free crystallites exists, with small orientation (up to 1-2^{o}) differences between them. Each crystallite illuminated diffracts its part of the X-ray beam to a slightly different place on the film and spot splitting results. For more information on mosaic structure, see McLean (1957). Figure 3.7c indicates relatively high quality strain-free material.

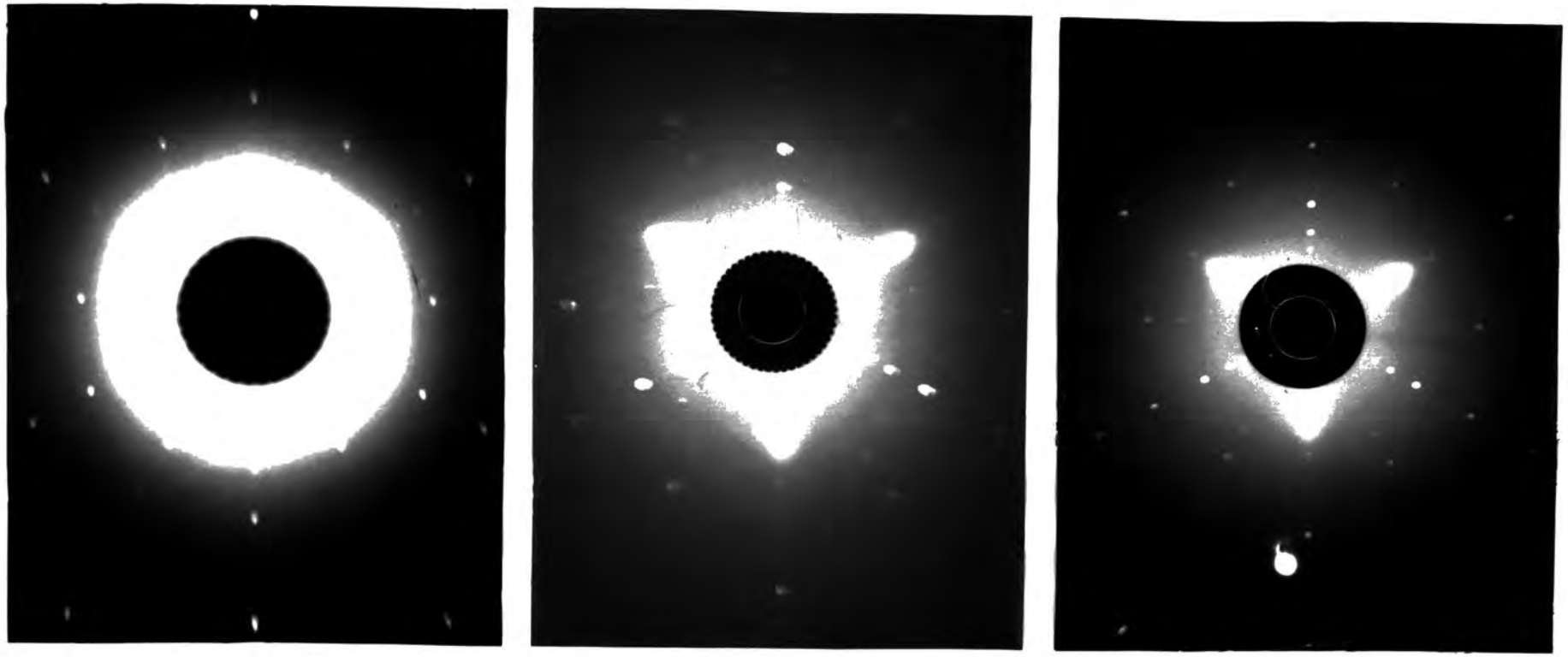

a. Spot spreading due to strained material

b. Spot splitting due to a mosaic structure

c. Good quality material

Figure 3.7.

Back reflection X-ray photographs of (a) melt grown (b) early vapour grown and (c) final vapour grown crystals.

b. Etch-pits in arsenic.

Freshly cleaved faces of the crystals have been etched and examined microscopically. Etches were composed of different proportions of hydrofluoric, nitric and glacial acetic acids (see Table 3.1). Pits of trigonal and hexagonal shape are found in all material, with overall densities averaging $10^5/cm^2$ in melt grown and $10^4/cm^2$ in final vapour-grown. The mosaic structure of the early vapour-grown crystals is dramatically revealed (figure 3.8). The following observations are general and not dependent on the growth procedure.

c. Slip lines.

Straight lines, mutually orientated at 120^o are observed, see figure 3.9, along the $[10\bar{1}]$ directions. Those which terminate, do so, (figure 3.10) in an etch pit. Different patterns of lines appear on separated faces of a cleaved crystal. These are slip lines; slip occurs on cleaving. The primary slip system in arsenic comprises the (111) as glide plane and the $[10\bar{1}]$ as slip directions (Barrett 1952) and this system cannot give rise to slip lines on the (111) plane. The lines result from slip in the (x-z)

Etch Composition			Etch Time	Pit Shape	Remarks
HF	HNO_3	CH_3COOH			
1	2	O	1 sec.	No pits	Oxidation globules on the surface
1	1	O	1 sec.	Irregular	Very violent reaction NO_2 fumes
2	1	O(Etch A)	1/2 sec.	Trigonal, Rounded	Used for producing trigonal pits
2	1	2	1/2 sec.	Round	Rapid reaction
2	1	6	5 sec.	Round	Shallow Pits
3	1	O(Etch B)	1 sec	Truncated trigonal and round	Between trigonal and hexagonal pits.
4	1	O(Etch C)	1 sec.	Hexagonal	Used for producing hexagonal pits
5	1	O	1 sec. 10 sec.	Irregular Irregular	Rough surface Surface broken up

Table 3.1.

Details of etching and resultant pit shapes

Figure 3.8

The mosaic structure of the early vapour grown material, revealed by etching.

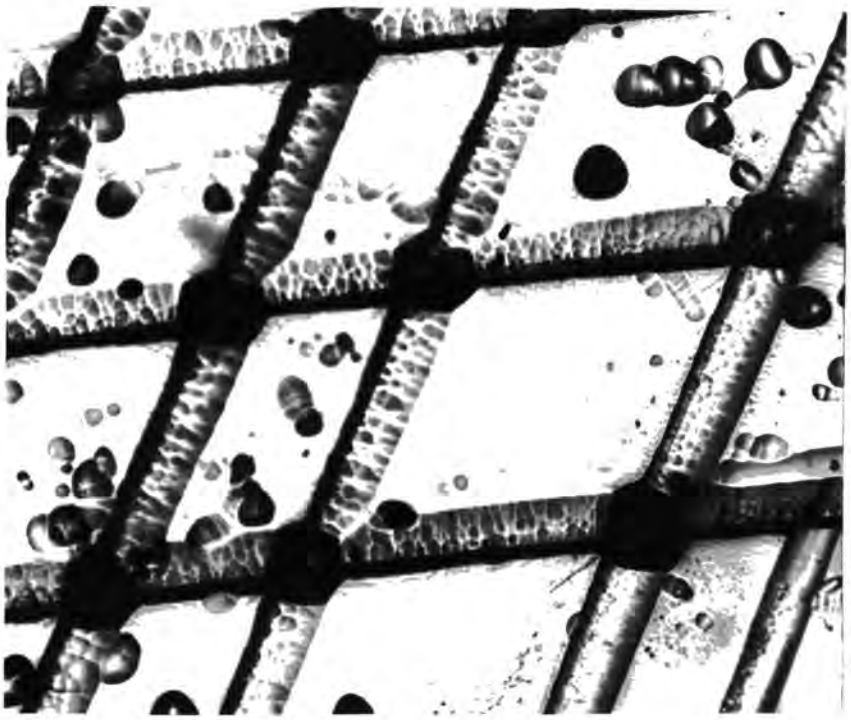

Figure 3.9. Duplex slip on the (111) cleavage face. The scarp and dip topography arises from etching at the surface steps (X500)

Figure 3.10. Slip lines on the (111) face, terminating in etch pits. The network of faint lines is thought to mark dislocations lying in the (111) plane (X50)

plane, a secondary glide plane. If the associated slip direction is the $\langle 111 \rangle$, then the etch pits at the ends of the slip lines would mark screw dislocations.

d. Etch pits - dislocations.

The etch pits are well defined; on further etching they enlarge whilst retaining their general shape and, except in a few cases, their number. Pits match on opposite cleaved faces and the etch pattern repeats with consecutive cleaving. Clearly the pits are sited at the points of emergence of dislocations on the (111) plane. Rows of closely spaced etch pits are observed in all crystals. By counting the line pit density at intersections and applying the method developed by Vogel et al. (1953) and extended to antimony by Wernick et al. (1958), these rows have been shown to indicate arrays of parallel edge dislocations defining low angle grain boundaries.

e. Pit shape.

Arsenic exhibits hexagonal as well as trigonal pits. The pit shape is characteristic of the etch used (Table 3.1); a trend is evident (figure 3.11) from the trigonal to hexagonal shape with increasing hydrofluoric acid concentration. To answer the question whether the different shaped pits arise at different

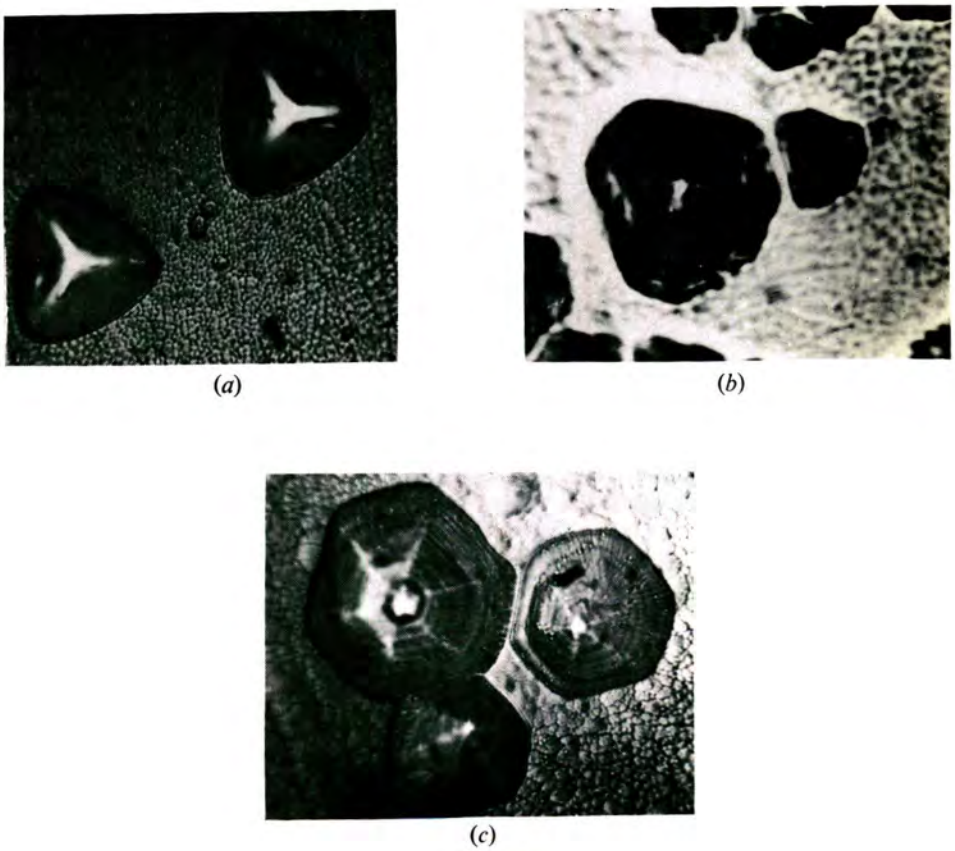

(a) (b) (c)

Figure 3.11

(a) Trigonal pits (etch A, see table 3.1) (b) A truncated pit (etch B). (c) Hexagonal pits (etch C) (X 500)

sites, one half of a cleaved crystal was etched to produce trigonal pits and the other to give hexagonal pits. With very few exceptions, the pit patterns were identical. Every dislocation can produce both types of pits; the etch is the determining factor.

Both kinds of pits are pyramidal and have edges parallel to the $\langle 10\bar{1} \rangle$ directions. But hexagonal pits have stepped sides, while trigonal pits are smooth. Many pits are symmetrical; the dislocations are parallel to the $\langle 111 \rangle$ axis. The existence of dislocations at a very acute angle to the cleavage plane is indicated by some highly antisymmetric pits (figure 3.12). Shallow grooves, like those shown in figure 3.10 suggest a network of dislocations actually in the cleavage plane. That both trigonal and hexagonal pits can be produced in arsenic, probably results from the lamellar aspect of its crystal structure (see page 15). If the etch will break thelong bond but not the short bond, then puckered hexagonal layers will be removed and hexagonal etch pits produced. But, if the layers are attacked singly, in the normal way, trigonal pits will result, showing just the threefold symmetry of the z-axis. For bismuth and antimony, closer to cubic in structure

Figure 3.12.

Etch pits produced from dislocations directed at an acute angle to the surface (etch A) (X 500).

(α = 57°14' and 57°7') than arsenic (α = 54°10'), the long and short bonds are almost equal, and only trigonal pits are found. Both types of pits are observed in bismuth telluride (α = 24°10') (Sagar and Faust 1967).

CHAPTER IV

THE THEORY OF THE GALVANOMAGNETIC EFFECTS IN ARSENIC

IV.1 Specification of Effects, in Tensor Notation.

a. The isothermal, electrical resistivity tensor.

Abeles and Meiboom (1954) introduced a tensor notation to provide a basic definition of all the galvanomagnetic effects in n-type germanium. Previously, the literature is fraught with confusing and ambiguous terms: the Hall effect, longitudinal Hall effect, planar Hall effect, quadratic Hall effect, transverse and longitudinal magnetoresistance (Beer 1963); all of which may be defined relative to various crystallographic and field directions. The basic principle of Abeles and Meiboom's method is to resolve all effects into a set of components referred to Cartesian axes. Then any desired effect may be specified by systematically summing appropriate components.

First, the axes are chosen. For mathematical simplicity they should be directed along axes of

crystallographic symmetry; in the case of the arsenic structure the binary-bisectrix-trigonal (1-2-3) set is an obvious choice. Suppose an electric current density ($\underline{J}$) is passed through an isothermal, single-crystal sample of arsenic in an arbitrary direction. Then the components referred to the binary, bisectrix and trigonal axes respectively are J_1, J_2 and J_3. The resulting electric field distribution may be measured by a vector $\underline{E}$ with components E_1, E_2 and E_3. Assuming that Ohm's law applies, $\underline{E}$ and $\underline{J}$ may be related:

$$E_1 = \rho_{11} J_1 + \rho_{12} J_2 + \rho_{13} J_3$$

$$E_2 = \rho_{21} J_1 + \rho_{22} J_2 + \rho_{23} J_3$$

$$E_3 = \rho_{31} J_1 + \rho_{32} J_2 + \rho_{33} J_3$$

or $E_i = \rho_{ij} J_j$

where the repetition of the subscript j implies summation (the Einstein convention). ρ_{ij} is a tensor of the second rank and has nine constant components or coefficients which may be written as a matrix :

$$\rho_{ij} \equiv \begin{pmatrix} \rho_{11} & \rho_{12} & \rho_{13} \\ \rho_{21} & \rho_{22} & \rho_{23} \\ \rho_{31} & \rho_{32} & \rho_{33} \end{pmatrix} \qquad (4.1)$$

A tensor of the first rank is a vector (e.g. $\underline{E}$ or $\underline{J}$). For the isotropic case, $\underline{E}$ and $\underline{J}$ are parallel:

$$E_1 = \rho J_1$$

$$E_2 = \rho J_2$$

$$E_3 = \rho J_3$$

and ρ is a tensor of the zeroth rank, i.e. a scalar. This is the case for the cubic lattice; only one coefficient is required to completely relate $\underline{E}$ and $\underline{J}$. Generally, certain identities exist between the coefficients for thermodynamic reasons and due to crystallographic symmetry. Thus for the A7 structure, seven of the nine coefficients that specify ρ_{ij} vanish, leaving ρ_{11} and ρ_{33}:

$$\rho_{ij} = \begin{pmatrix} \rho_{11} & 0 & 0 \\ 0 & \rho_{11} & 0 \\ 0 & 0 & \rho_{33} \end{pmatrix}$$

b. The isothermal, low-field, magnetoresistivity tensor.

To extend the tensor notation to include galvanomagnetic effects, the components of ρ_{ij} are made dependent on magnetic field to form the magnetoresistivity tensor $\rho_{ij}(\underline{H})$.

$$E_i = \rho_{ij}(\underline{H})\ J_j \qquad (4.2)$$

$$\rho_{ij}(H) \equiv \begin{pmatrix} \rho_{11}(\underline{H}) & \rho_{12}(\underline{H}) & \rho_{13}(\underline{H}) \\ \rho_{21}(\underline{H}) & \rho_{22}(\underline{H}) & \rho_{23}(\underline{H}) \\ \rho_{31}(\underline{H}) & \rho_{32}(\underline{H}) & \rho_{33}(\underline{H}) \end{pmatrix}$$

Since each component is now a function of field and no longer constant the term 'coefficient' is not strictly accurate. The nine parameters are'the components of the magnetoresistivity tensor'.

The next step is to express $\rho_{ij}(\underline{H})$ as a definite function of $\underline{H}$. It will be seen later (page 76) that one way of doing this is as a power series:

$$\rho_{ij}(\underline{H}) = \rho_{ij} + R_{ijk}H_k + A_{ijkl}\ H_kH_l + T_{ijklm}H_kH_lH_m + F_{ijklmn}H_kH_lH_mH_n + \ldots\ldots\ldots\ldots$$

ρ_{ij}, the second rank resistivity tensor is retained and R_{ijk}, A_{ijkl}, T_{ijklm}, F_{ijklmn} being 3rd, 4th, 5th, 6th rank tensors respectively are introduced to relate progressively higher powers of $\underline{H}$. This massive battery of tensors may be cut down by considering only the low-field case when $\mu H << 1$ (μ is the carrier

mobility). Then the series converges rapidly, and only terms to H^2 are significant:

$$\rho_{ij}(\underline{H}) = \rho_{ij} + R_{ijk}H_k + A_{ijkl}H_kH_l$$

Still a large number of coefficients exists:

Tensor	Matrix Size	No. of coefficients
ρ_{ij}	3 x 3	9
R_{ijk}	3 x 3 x 3	27
A_{ijkl}	3 x 3 x 3 x 3	81
	Total	117

As before symmetry relations may be used to reduce the number of independent coefficients. Thermodynamic arguments lead to the Onsager relation (Onsager 1931): $\rho_{ij}(\underline{H}) = \rho_{ji}(-\underline{H})$. The following identities follow (Juretschke 1955):

$$\begin{aligned} \rho_{ij} &\equiv \rho_{ji} \\ A_{ijkl} &\equiv A_{jikl} \quad \text{(all permutations of kl)} \\ R_{ijk} &\equiv -R_{jik} \end{aligned} \tag{4.3}$$

As an example of use, these identities are now applied to the expansion of $\rho_{11}(\underline{H})$, the first of the nine components of $\rho_{ij}(\underline{H})$.

$$\rho_{11}(\underline{H}) = \rho_{11} + R_{111}H_1 + R_{112}H_2 + R_{113}H_3 + A_{1111}H_1^2 + A_{1122}H_2^2$$

$$+ A_{1133}H_3^2 + A_{1112}H_1H_2 + A_{1113}H_1H_3 + A_{1121}H_2H_1$$

$$+ A_{1123}H_2H_3 + A_{1131}H_3H_1 + A_{1132}H_3H_2 .$$

This contains thirteen coefficients (one ninth of one hundred and seventeen). Applying (4.3):-

$$R_{111} = -R_{111} \equiv 0$$

Similarly $R_{112} \equiv R_{113} \equiv 0$

$$A_{1112} = A_{1121}$$

$$A_{1113} = A_{1131}$$

$$A_{1123} = A_{1132}$$

and the number of independent components is reduced to seven. In addition to the restrictions of Onsager's relation, the components are subject to the crystallographic point group symmetry. Juretschke (1955) has developed this systematically using group theory. Of significance for $\rho_{11}(\underline{H})$ is that A_{1112} and A_{1113} vanish, and $A_{1123} \equiv A_{2223}$, leaving just five coefficients:

$$\rho_{11},\ A_{1111},\ A_{1122},\ A_{1133},\ A_{2223}.$$

A similar treatment of all nine components of $\rho_{ij}(\underline{H})$ reveals that only twelve coefficients are independent. These twelve coefficients may be

described as the twelve coefficients that define the isothermal magnetoresistivity tensor to second order in magnetic field:

		Shorthand notation
Resistivity	ρ_{11}	ρ_{11}
	ρ_{33}	ρ_{33}
Hall	R_{123}	R_{123}
	R_{231}	R_{231}
Magneto-resistivity	$A_{11,11}$	A_{11}
	$A_{33,33}$	A_{33}
	$A_{22,23}$	A_{24}
	$A_{23,22}$	A_{42}
	$A_{11,22}$	A_{12}
	$A_{11,33}$	A_{13}
	$A_{33,11}$	A_{31}
	$A_{23,23}$	A_{44}

The expansion of the nine components of $\rho_{ij}(\underline{H})$ to second order in magnetic field is (Juretschke 1955):

$$\rho_{11}(\underline{H}) = \rho_{11} + A_{11}H_1^2 + A_{12}H_2^2 + A_{13}H_3^2 - 2A_{24}H_2H_3$$

$$\rho_{22}(\underline{H}) = \rho_{11} + A_{12}H_1^2 + A_{11}H_2^2 + A_{13}H_3^2 + 2A_{24}H_2H_3$$

$$\rho_{33}(\underline{H}) = \rho_{33} + A_{31}H_1^2 + A_{31}H_2^2 + A_{33}H_3^2$$

$$\rho_{23}(\underline{H}) = R_{231}H_1 - A_{42}H_1^2 + A_{42}H_2^2 + 2A_{44}H_2H_3 \qquad (4.4)$$

$$\rho_{31}(\underline{H}) = R_{231}H_2 + 2A_{44}H_3H_1 - 2A_{42}H_1H_2$$

$$\rho_{12}(\underline{H}) = R_{123}H_3 - 2A_{24}H_3H_1 + (A_{11} - A_{12})H_1H_2$$

There is no need to write down $\rho_{13}(\underline{H})$, $\rho_{21}(\underline{H})$ or $\rho_{32}(\underline{H})$; they follow automatically since $\rho_{ij}(\underline{H}) = \rho_{ji}(-\underline{H})$.

We have now obtained a basic set of twelve coefficients that will completely specify the low-field galvanomagnetic effects in arsenic (or any material of crystallographic point group $\bar{3}m$). Knowing these coefficients, $\rho_{ij}(\underline{H})$ is defined by (4.4) and then $\underline{E}$ and $\underline{J}$ related by (4.2) The scheme is quite general; $\underline{J}$ and $\underline{H}$ may be at any angle to the crystal axes and resolved into components. Also, any particular Hall or magnetoresistance effect does not have to be tagged by a lengthy description of orientation; the values of the twelve coefficients are absolute at any given temperature.

The process may be used in reverse to measure the twelve coefficients. By choosing special cases of

E-J-H orientations, each coefficient may be isolated and measured in turn. As an example, consider the configuration shown in figure 4.1. $\underline{J}$ is in the binary (1) direction and $\underline{H}$ is in the trigonal (3) direction. The probes measure only E_1. Therefore:-

$$J_1 = J;\ J_2 = J_3 = 0$$

$$H_3 = H;\ H_1 = H_2 = 0$$

$$E_1 = E.$$

Thus, from (4.2) ; $E = \rho_{11}(\underline{H})J$

$\rho_{11}(\underline{H})$ comes from (4.4); $\rho_{11}(\underline{H}) = \rho_{11} + A_{13}H^2$.
Hence $E = (\rho_{11}+A_{13}H^2)J$ or $E/J=A_{13}H^2+\rho_{11}$
and a graphical plot of E/J against H^2 has a gradient A_{13} and an intercept ρ_{11}.

A systematic scheme for determining all twelve coefficients is described in chapter VI.

c. The low-field magnetoconductivity tensor.

The theoretical derivation of the galvanomagnetic effects in terms of band parameters (see next section) is more conveniently carried out by using the magneto-conductivity tensor, the inverse of the magneto-resistivity tensor. It is defined:

$$J_i = \sigma_{ij}(\underline{H})E_j.$$

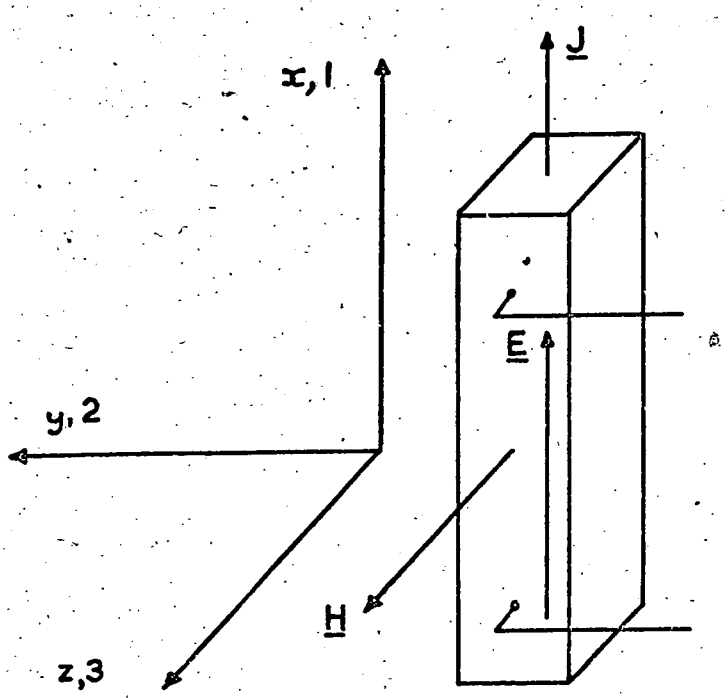

Figure 4.1

An illustration of sample orientation and field alignments used to measure ρ_{11} and A_{13}.

and expanded:

$$\sigma_{ij}(\underline{H}) = \sigma_{ij} - P_{ijk}H_k - B_{ijkl}H_kH_l \quad \cdots\cdots$$

For convenience, the minus signs are employed to give B_{ijkl} positive values since conductivity decreases with increasing magnetic field. Now we have twelve coefficients in inverse relationship to the magnetoresistivity coefficients:-

Magnetoresistivity	Magnetoconductivity	
ρ_{11}	σ_{11}	conductivity
ρ_{33}	σ_{33}	
R_{123}	P_{123}	inverse Hall
R_{231}	P_{231}	
A_{11}	B_{11}	magneto-conductivity
A_{33}	B_{33}	
A_{24}	B_{24}	
A_{42}	B_{42}	
A_{12}	B_{12}	
A_{13}	B_{13}	
A_{31}	B_{31}	
A_{44}	B_{44}	

The link is the equation:

$$\sigma_{ij}(\underline{H})\rho_{ij}(\underline{H}) = \delta_{ij} \quad \text{(Kronecker } \delta\text{)}$$

solved by Juretschke (1955) :-

$$\sigma_{11} = \frac{1}{\rho_{11}} \qquad \sigma_{33} = \frac{1}{\rho_{33}}$$

$$P_{123} = \frac{R_{123}}{\rho_{11}^2} \qquad P_{231} = \frac{R_{231}}{\rho_{11}\rho_{33}}$$

$$B_{11} = \frac{A_{11}}{\rho_{11}^2} \qquad B_{33} = \frac{A_{33}}{\rho_{33}^2}$$

$$B_{24} = \frac{A_{24}}{\rho_{11}^2} \qquad B_{42} = \frac{A_{42}}{\rho_{11}\rho_{33}} \tag{4.5}$$

$$B_{12} = \frac{A_{12}}{\rho_{11}^2} + \frac{R_{231}^2}{\rho_{11}^2\rho_{33}} \qquad B_{13} = \frac{A_{13}}{\rho_{11}^2} + \frac{R_{123}^2}{\rho_{11}^3}$$

$$B_{31} = \frac{A_{31}}{\rho_{33}^2} + \frac{R_{231}^2}{\rho_{11}\rho_{33}^2} \qquad B_{44} = \frac{A_{44}}{\rho_{11}\rho_{33}} - \frac{1}{2}\frac{R_{123}R_{231}}{\rho_{11}^2\rho_{33}}$$

So far, we have obtained twelve coefficients that define the magnetoconductivity tensor. In the next section, these coefficients are derived from fundamental physical terms.

IV.2 A Derivation of the Magnetoconductivity Tensor from Band Theory.

a. The Boltzmann equation.

The transport of electrical carriers under general

field conditions is governed by the Boltzmann equation which states:-

$$\left[\frac{\partial f_{\underline{k}}(\underline{r},t)}{\partial t}\right] + \left[\frac{\partial f_{\underline{k}}(\underline{r},t)}{\partial t}\right] + \left[\frac{\partial f_{\underline{k}}(\underline{r},t)}{\partial t}\right] = 0 \qquad (4.6)$$

diffusion fields scattering

for steady state conditions. $f_{\underline{k}}$ is the density of carriers in a state $\underline{k}$ of k-space in the neighbourhood of $\underline{r}$ in real space at a time t.

It may be shown (see Ziman 1964):

$$\left[\frac{\partial f_{\underline{k}}(\underline{r},t)}{\partial t}\right] = -\underline{v}_{\underline{k}} \cdot \left\{\frac{\partial f_{\underline{k}}(\underline{r},t)}{\partial \underline{r}}\right\} \qquad (4.7)$$

diffusion

where $\underline{v}_{\underline{k}}$ is the velocity of a carrier in the state $\underline{k}$. In a similar manner, it follows that for a crystal subjected to electric ($\underline{E}$) and magnetic ($\underline{H}$) fields :

$$\left[\frac{\partial f_{\underline{k}}(\underline{r},t)}{\partial t}\right] = -\frac{e}{\hbar}\left\{\underline{E} + \frac{1}{c}\,\underline{v}_{\underline{k}} \times \underline{H}\right\} \cdot \left\{\frac{\partial f_{\underline{k}}(\underline{r},t)}{\partial \underline{k}}\right\} \qquad (4.8)$$

fields

e is the electronic charge and c the velocity of light.

The only simple assessment of the scattering term in the Boltzmann equation is a phenomenological assumption:-

$$-\left[\frac{\partial f_{\underline{k}}}{\partial t}\right]_{\text{scattering}} = \frac{1}{\tau}\left(f_{\underline{k}} - f_{\underline{k}}^{\,o}\right) \qquad (4.9)$$

Here $f_{\underline{k}}^{\,o}$ is the equilibrium, Fermi-Dirac distribution function, i.e. the distribution function when all fields are absent :

$$f_{\underline{k}}^{\,o} = \frac{1}{1 + \exp\left(\frac{\varepsilon - \varepsilon_f}{kT}\right)} \; ; \; \varepsilon \text{ denotes carrier energy.}$$

τ is the relaxation time; it measures the rate of decay of $f_{\underline{k}}$ to $f_{\underline{k}}^{\,o}$ when the fields are removed at time $t = 0$:

$$f_{\underline{k}}(t) - f_{\underline{k}}^{\,o} = \left(f_{\underline{k}}(0) - f_{\underline{k}}^{\,o}\right) \exp\left(-\frac{t}{\tau}\right)$$

obtained by integrating (4.9).

Substituting (4.7), (4.8), (4.9) into the Boltzmann equation (4.6)

$$-v_{\underline{k}} \cdot \frac{\partial f_{\underline{k}}}{\partial \underline{r}} - \frac{e}{\hbar}\left\{\underline{E} + \frac{1}{c}\, v_{\underline{k}} \times \underline{H}\right\} \cdot \frac{\partial f_{\underline{k}}}{\partial \underline{k}} = \frac{f_{\underline{k}} - f_{\underline{k}}^{\,o}}{\tau} \qquad (4.10)$$

b. Electrical conductivity in the absence of a magnetic field.

As a simple application of the Boltzmann equation, consider the case of an isothermal crystal when only $\underline{E}$ is applied.

$$\frac{\partial f_{\underline{k}}}{\partial \underline{r}} = 0 \text{ and } \underline{H} = 0.$$

Since the deviation of $f_{\underline{k}}$ from $f_{\underline{k}}^{o}$ is small, the approximation $\frac{\partial f_{\underline{k}}}{\partial \underline{k}} = \frac{\partial f_{\underline{k}}^{o}}{\partial \underline{k}}$ is made on the L.H.S. of (4.10).

Now

$$\frac{\partial f_{\underline{k}}^{o}}{\partial \underline{k}} = \frac{\partial f_{\underline{k}}^{o}}{\partial \varepsilon} \cdot \frac{\partial \varepsilon}{\partial \underline{k}} = \hbar \underline{v}_{\underline{k}} \cdot \frac{\partial f_{\underline{k}}^{o}}{\partial \varepsilon}$$

so that (4.10) becomes :

$$-\left\{\frac{\partial f_{\underline{k}}^{o}}{\partial \varepsilon}\right\} \tau \underline{v}_{\underline{k}} \cdot e\underline{E} = f_{\underline{k}} - f_{\underline{k}}^{o} \qquad (4.11)$$

To calculate the electrical conductivity, an expression for the current density, $\underline{J}$, is required. Each carrier creates a current $e\underline{v}_{\underline{k}}$ and the number of carriers per unit volume of the crystal, in k-states within a volume $d\underline{k}$ is

$$\frac{2}{(2\pi)^3} f_{\underline{k}} \, d\underline{k}$$

$$\therefore \quad \underline{J} = \frac{1}{4\pi^3} \int e\underline{v}_{\underline{k}} f_{\underline{k}} \, d\underline{k}$$

Substituting for $f_{\underline{k}}$ from (4.11),

$$J = \frac{1}{4\pi^3} \int e^2 \tau \underline{v}_{\underline{k}} (\underline{v}_{\underline{k}} \cdot \underline{E}) \left(- \frac{\partial f_{\underline{k}}^{\,o}}{\partial \varepsilon} \right) d\underline{k}$$

since $\int e \underline{v}_{\underline{k}} f_{\underline{k}}^{\,o} \, d\underline{k} = 0$.

Next a transform is made from a volume integration to an integration over constant energy surfaces. If dS is an element of the surface, then $\frac{\partial \varepsilon}{\partial \underline{k}}$ is a vector perpendicular to dS. The height of a cylinder of base dS, volume $d\underline{k}$ between surfaces ε and $\varepsilon + d\varepsilon$ is

$$dk_{\perp_r} = \frac{d\varepsilon}{\left| \frac{d\varepsilon}{d\underline{k}} \right|} = \frac{d\varepsilon}{\hbar v_{\underline{k}}}$$

$$\therefore \quad d\underline{k} = \frac{dS d\varepsilon}{\hbar v_{\underline{k}}} \qquad (4.12)$$

$$\text{and } J = \frac{1}{4\pi^3} \iint e^2 \tau \underline{v}_{\underline{k}} \left(\underline{v}_{\underline{k}} \cdot \underline{E} \right) \left(- \frac{\partial f_{\underline{k}}^{\,o}}{\partial \varepsilon} \right) \frac{dS d\varepsilon}{\hbar v_{\underline{k}}}$$

In the degenerate case, $\frac{\partial f_{\underline{k}}^{\,o}}{\partial \varepsilon}$ behaves as a delta function at the Fermi level and an integration over the Fermi surface is required :

$$J = \frac{1}{4\pi^3} \frac{e^2 \tau}{\hbar} \int \frac{\underline{v}_{\underline{k}} (\underline{v}_{\underline{k}} \cdot \underline{E})}{v_{\underline{k}}} \, dS_F$$

Comparing this with Ohm's law, $J_i = \sigma_{ij} E_j$,

$$\sigma_{ij} = \frac{e^2 \tau}{4\pi^3 \hbar} \int \frac{v_i v_j}{v_{\underline{k}}} dS_F \qquad (4.13)$$

To proceed further, a model of the Fermi surface is required. For an isotropic metal and free electrons, the Fermi surface is spherical, $\varepsilon = \frac{1}{2} \frac{\hbar^2 k_F^2}{m}$ and σ is a scalar. For $\underline{E}$ and $\underline{J}$ both in the x-direction,

$$\left\{ \underline{v}_{\underline{k}} (\underline{v}_{\underline{k}} \cdot \underline{E}) \right\}_x = v_x^2 E$$

which is 1/3 of $v^2 E$.

$$\therefore \quad \sigma = \frac{1}{4\pi^3} \frac{e^2 \tau}{\hbar} \frac{1}{3} v \int dS_F$$

Now $v = \frac{1}{\hbar} \frac{\partial \varepsilon}{\partial k} = \frac{\hbar k_F}{m}$ $\quad \therefore \quad \varepsilon = \frac{1}{2} \frac{\hbar^2 k_F^2}{m}$

and $\quad dS_F = 4\pi k_F^2$.

$$\therefore \quad \sigma = \frac{1}{4\pi^3} \frac{e^2 \tau}{\hbar} \frac{1}{3} \frac{\hbar k_F}{m} \cdot 4\pi k_F^2$$

$$= \frac{1}{4\pi^3} \frac{e^2 \tau}{m} \frac{4}{3} \pi k_F^3$$

$$\text{or } \sigma = \frac{e^2\tau}{m} \frac{V_F}{4\pi^3}$$

where V_F is the volume in k-space enclosed by the Fermi surface.

Since there are $\frac{1}{4\pi^3}$ carriers per unit volume of k-space, $N = \frac{V_F}{4\pi^3}$; N is the carrier density.

$$\therefore \quad \sigma = \frac{Ne^2\tau}{m} \qquad (4.14)$$

c. Anisotropic, isothermal, galvanomagnetic effects in arsenic

In this section, the Boltzmann equation is applied to the galvanomagnetic effects in arsenic and the twelve magnetoconductivity coefficients are derived in terms of energy band and carrier parameters. The analysis applies to any material possessing the arsenic crystal structure.

The distribution function, $f_{\underline{k}}$, is redefined by introducing a function Φ (Wilson 1953):

$$f_{\underline{k}} = f_{\underline{k}}^{o} - \Phi \frac{\partial f_{\underline{k}}^{o}}{\partial \varepsilon}$$

Then the Boltzmann equation (4.10) for an isothermal metal becomes:

$$\frac{1}{\tau}\underline{\Phi} + \frac{e}{\hbar}\underline{E}\cdot\operatorname{grad}\varepsilon + \frac{e}{\hbar^2 c}\underline{H}.\underline{\Omega}\underline{\Phi} = 0 \qquad (4.15)$$

where $\underline{\Omega}$ is the operator $\underline{\Omega} = \operatorname{grad}_{\underline{k}}\varepsilon X \operatorname{grad}_{\underline{k}}$.

The electric current is:

$$\underline{J} = \frac{e}{4\pi^3\hbar}\int \operatorname{grad}_{\underline{k}}\varepsilon\,\underline{\Phi}\,\frac{\partial f_{\underline{k}}^{o}}{\partial\varepsilon}\,d\underline{k} \qquad (4.16)$$

The solution of (4.15) in ascending powers of $\underline{H}$ obtained by interation (Jones and Zener 1934) is :

$$\underline{\Phi} = -\frac{e}{h}\left[\tau\underline{E}.\operatorname{grad}_{\underline{k}}\varepsilon - \frac{e}{\hbar^2 c}\,\tau\underline{H}.\underline{\Omega}(\tau\underline{E}.\operatorname{grad}_{\underline{k}}\varepsilon)\right.$$

$$\left. + \frac{e^2}{\hbar^4 c^2}\,\tau\underline{H}.\underline{\Omega}\left\{\tau\underline{H}.\underline{\Omega}(\tau\underline{E}.\operatorname{grad}_{\underline{k}}\varepsilon)\right\} + ...\right]$$

A knowledge of $\underline{\Phi}$ defines $\underline{J}$ by (4.16). In tensor notation, (Abeles and Meiboom 1954).

$$\Omega_i = \varepsilon_{ikl}\,\frac{\partial\varepsilon}{\partial k_k}\cdot\frac{\partial}{\partial k_l}$$

where the tensor ε_{ikl} is defined

$$\varepsilon_{123} = \varepsilon_{231} = \varepsilon_{312} = +1$$

$$\varepsilon_{231} = \varepsilon_{132} = \varepsilon_{321} = -1$$

and all other ε_{ijk} are zero.

The coefficients defining the magnetoconductivity tensor - $\sigma_{ij}(\underline{H}) = \sigma_{ij} - P_{ijk}H_k - B_{ijkl}\,H_kH_l$ - are then expressed as follows:-

$$\sigma_{ij} = -\frac{e^2}{4\pi^3\hbar^2}\int \tau \frac{\partial f_{\underline{k}}^{o}}{\partial \varepsilon}\frac{\partial \varepsilon}{\partial k_i}\frac{\partial \varepsilon}{\partial k_j}\,d\underline{k} \qquad (4.17)$$

$$P_{ijk} = -\frac{e^2}{4\pi^3\hbar^4 c}\int \tau \frac{\partial f_{\underline{k}}^{o}}{\partial \varepsilon}\frac{\partial \varepsilon}{\partial k_i}\frac{\partial \varepsilon}{\partial k_l}\frac{\partial}{\partial k_m}\left(\tau\frac{\partial \varepsilon}{\partial k_j}\right)\varepsilon_{klm}\,d\underline{k} \qquad (4.18)$$

$$B_{ijkl} = -\frac{e^4}{4\pi^3\hbar^6 c^2}\int \tau \frac{\partial f_{\underline{k}}^{o}}{\partial \varepsilon}\frac{\partial \varepsilon}{\partial k_i}\frac{\partial \varepsilon}{\partial k_p}\frac{\partial}{\partial k_q}\tau\frac{\partial \varepsilon}{\partial k_m}\frac{\partial}{\partial k_n}\left(\tau\frac{\partial \varepsilon}{\partial k_j}\right)$$

$$\times \frac{1}{2}\left[\varepsilon_{qpl}\varepsilon_{nmk} + \varepsilon_{qpk}\varepsilon_{nml}\right]\,d\underline{k} \qquad (4.19)$$

Note that substituting $v_i = \frac{1}{\hbar}\frac{\partial \varepsilon}{\partial k_i}$ and $v_j = \frac{1}{\hbar}\frac{\partial \varepsilon}{\partial k_j}$ in (4.17) gives :

$$\sigma_{ij} = \frac{e^2}{4\pi^3}\int \tau\, v_i\, v_j \left(-\frac{\partial f_{\underline{k}}^{o}}{\partial \varepsilon}\right)\,d\underline{k}$$

which transforms, using $d\underline{k} = \frac{d\varepsilon dS}{\left|\frac{\partial \varepsilon}{\partial \underline{k}}\right|}$ to

$$\sigma_{ij} = \frac{e^2}{4\pi^3\hbar}\int \tau \frac{v_i v_i}{v_{\underline{k}}} \, dS_F$$

in agreement with (4.13).

As for the simpler case of electrical conductivity in the absence of magnetic field, to proceed, a specification of the dependence of ε and τ on $\underline{k}$ is required. In general they will be complex functions of $\underline{k}$, but much can be achieved by considering simple models.

In chapter I it was shown that the simple model of spherical energy surfaces fails to explain anisotropy of the galvanomagnetic effects. Retaining the quadratic ε-$\underline{k}$ relationship, Jones (1936) invoked a model of one ellipsoidal energy surface centred on $\underline{k} = 0$ for each of two carriers and obtained a qualitative explanation of the anisotropic effects in bismuth. A theory of the galvanomagnetic effects based on a model of several energy extrema at equivalent points in $\underline{k}$-space and ellipsoidal energy surfaces centred on these points has been developed by Abeles and Meiboom (1954) and Herring (1955). They applied this 'many-valley' model to cubic semiconductors, for which the conductivity and Hall effects are isotropic. However, for non-cubic materials, this model does predict that these properties

may be anisotropic and quantitative analyses of the galvanomagnetic effects in bismuth (Abeles and Meiboom 1956), bismuth telluride (Drabble, Groves and Wolfe 195) and in particular antimony (Freedman and Juretschke 1961, Epstein and Juretschke 1963, Oktu and Saunders 1967) have followed. For arsenic, the recent mapping of the Fermi surface, discussed in chapter II, demonstrates that a multivalley band model is indeed correct. Such a model is now used to evaluate the integrals 4.17,4.18,4.19.

The following assumptions are made:-

1. The minimum energy occurs at a number of equivalent points $\underline{k}_o^{\,i}$, related by the crystal symmetry.

2. Constant energy surfaces in $\underline{k}$-space are sets of similar ellipsoids centred on these points. If suitable axes, known as the principal axes of the i th valley are chosen, then the energy ε in the vicinity of $\underline{k}_o^{\,i}$ may be written

$$\varepsilon = \varepsilon_o + \frac{\hbar^2}{2}\left[\frac{(k_1^{\,i} - k_{1o}^{\,i})^2}{m_1} + \frac{(k_2^{\,i} - k_{2o}^{\,i})^2}{m_2} + \frac{(k_3^{\,i} - k_{3o}^{\,i})^2}{m_3}\right]$$

ε_o is the band energy minimum and m_1, m_2, m_3 are the effective masses along the principal axes of the ellipsoids.

3a. Each type of carrier contributes independently to the galvanomagnetic effects.

3b. Each valley also contributes independently; the scattering of a carrier is restricted to processes peculiar to its own valley.

4. The relaxation time is independent of $\underline{k}$:

$$\tau = b\varepsilon^{-\lambda} \qquad (4.20)$$

where λ and b depend on the scattering mechanism. The validity of the relaxation time approximation in general is discussed by Herring (1955). The further assumption that it is isotropic in $\underline{k}$-space is not too resistrictive: it is a reasonable approximation provided that the components of the tensor $\tau(\underline{k})$ are within 2:1 (Herring and Vogt 1956).

With these assumptions, Drabble and Wolfe (1956) have systematically evaluated the integrals (4.17, 4.18,4.19) for the $R\bar{3}m$ structure:

$$\sigma^{i}_{pq} = \frac{A}{m_p}\,\delta_{pq}$$

$$P^{i}_{pq} = \frac{-B}{m_p m_q}\,\varepsilon_{pqr} \qquad (4.21)$$

$$B^{i}_{pqrs} = \frac{C}{m_p m_q m_t}\,(\varepsilon_{tps}\varepsilon_{qtr}+\varepsilon_{tpr}\varepsilon_{qts}).$$

The superscript (i) denotes the tensor components relative to the principal axes of the i th valley. A, B and C depend on the nature of $f_{\underline{k}}^{o}$, b and λ; for the degenerate case :

$$A = \frac{e^2}{3\pi^2} \; b \; \left(\frac{2m^*}{\hbar^2}\right)^{1.5} \; \varepsilon_F^{(1.5-\lambda)}$$

$$B = \frac{e^3}{3\pi^2} \; \frac{b^2}{c} \left(\frac{2m^*}{\hbar^2}\right)^{1.5} \; \varepsilon_F^{(1.5-2\lambda)} \qquad (4.22)$$

$$C = \frac{e^4}{6\pi^2} \; \frac{b^3}{c^2} \left(\frac{2m^*}{\hbar^2}\right)^{1.5} \; \varepsilon_F^{(1.5-3\lambda)}$$

where m^* denotes $(m_1 m_2 m_3)^{1/3}$ and ε_F the Fermi energy.

The following relations exist :

$$B^2 = 2AC$$

$$\sigma_{pq}^{i} = 0 \text{ unless } p = q$$

$$P_{pqr}^{i} = 0 \text{ unless p,q,r are all different.}$$

$$B_{pqrs}^{i} = 0 \text{ unless p,q,r,s, are equal in pairs.}$$

Simplifications may be made as follows:

If N is the total carrier density, then the usual degenerate expression holds:

$$N = \frac{1}{3\pi^2}\left(\frac{2m^*}{\hbar^2}\right)^{1.5} \varepsilon_F^{1.5} \qquad (4.23a)$$

Only carriers close to the Fermi surface contribute to the galvanomagnetic effects; the relaxation time expression (4.20) becomes:

$$\tau = b\varepsilon_F^{-\lambda} \qquad (4.23b)$$

Substituting (4.23a,b) into (4.22) gives

$$\begin{aligned} A &= Ne^2\tau \\ B &= \frac{N}{c} e^3\tau^2 \\ C &= \frac{N}{2c^2} e^4\tau^3 \end{aligned} \qquad (4.24)$$

so that (4.21) may be written :

$$\begin{aligned} \sigma_{pq}^{i} &= Ne^2\tau\left(\frac{1}{m_p}\right)\delta_{pq} \\ P_{pq}^{i} &= -\frac{N}{c} e^3\tau^2\left(\frac{1}{m_p m_q}\right)\varepsilon_{pqr} \\ B_{pqrs}^{i} &= \frac{N}{2c^2} e^4\tau^3\left(\frac{1}{m_p m_q m_t}\right)(\varepsilon_{tps}\varepsilon_{qtr} + \varepsilon_{tpr}\varepsilon_{qts}) \end{aligned} \qquad (4.25)$$

The final stage is to transform the contributions from the separate valleys given by equations (4.25) to a common co-ordinate system and sum. This is done in accordance with the symmetry of the particular multivalley

model, in this case three or six ellipsoids centred on the mirror planes of the $R\bar{3}m$ crystal structure. Two carriers are incorporated by simple addition and three electron (μ_i) and three hole(ν_i) mobilities introduced :

$$\mu_i = \frac{e\tau_e}{m_{ei}} \qquad \nu_i = \frac{e\tau_h}{m_{hi}}$$

Then the twelve magnetoconductivity coefficients are described in terms of nine parameters: total electron density N, equal to the hole density, three electron mobilities μ_1, μ_2, μ_3 along the axes of each electron ellipsoid, corresponding hole mobilities ν_1, ν_2, ν_3 and ellipsoid tilt angles ψ_e, ψ_h with cosines C_e, C_h and sines S_e, S_h. μ_1 and ν_1 are directed along the binary axes; μ_2, μ_3 and ν_2, ν_3 are along the ellipsoid axes in the mirror plane. The tilt angles are defined as the angle of rotation in the mirror plane of m_3 away from the trigonal axis towards X (see page 19). Carrier densities and all mobilities are defined to be positive. The equations are (Epstein and Juretschke 1963):

$$\sigma_{11} = Ne\{(\mu_1+C_e^2\mu_2+S_e^2\mu_3)+(\nu_1+C_h^2\nu_2+S_h^2\nu_3)\}/2$$

$$\sigma_{33} = Ne\{(S_e^2\mu_2+C_e^2\mu_3)+(S_h^2\nu_2+C_h^2\nu_3)\}$$

$$-P_{231} = Ne\{\nu_2\nu_3+\nu_1(S_h^2\nu_2+Ch^2\nu_3)\}$$
$$-\{\mu_2\mu_3+\mu_1(S_e^2\mu_2+C_e^2\mu_3)\}/2c$$

$$-P_{123} = Ne\{\nu_1(C_h^2\nu_2+S_h^2\nu_3)\}-\{\mu_1(C_e^2\mu_2+S_e^2\mu_3)\}/c$$

The rest of the equations are written more conveniently by including only the electron terms, those of the holes being identical in form and simply added on:

$$B_{13} = Ne(\mu_1+C_e^2\mu_2+S_e^2\mu_3)\{\mu_1(C_e^2\mu_2+S_e^2\mu_3)\}/2c^2$$

$$B_{31} = Ne(S_e^2\mu_2+C_e^2\mu_3)\{\mu_2\mu_3+\mu_1(S_e^2\mu_2+C_e^2\mu_3)\}/2c^2$$

$$-B_{44} = Ne(S_e^2\mu_2+C_e^2\mu_3)\{\mu_1(C_e^2\mu_2+S_e^2\mu_3)\}/2c^2$$

$$B_{11} = Ne\{S_e^2\mu_2(\mu_1-\mu_3)^2+C_e^2\mu_3(\mu_1-\mu_2)^2$$
$$+3C_e^2S_e^2\mu_1(\mu_2-\mu_3)^2\}/8c^2$$

$$B_{12} = Ne\{3S_e^2\mu_2(\mu_1^2+\mu_3^2)+3C_e^2\mu_3(\mu_1^2+\mu_2^2)$$
$$+C_e^2S_e^2\mu_1(\mu_2-\mu_3)^2+2\mu_1\mu_2\mu_3\}/8c^2$$

$$B_{33} \equiv (-B_{12}+3B_{11}-2B_{44})/2=NeC_e^2S_e^2\mu_1(\mu_2-\mu_3)^2/c^2$$

$$B_{24} = NeC_eS_e\mu_1(\mu_2-\mu_3)(-\mu_1+C_e^2\mu_2+S_e^2\mu_3)/4c^2$$

$$B_{42} = NeC_eS_e(\mu_2-\mu_3)\{\mu_2\mu_3-\mu_1(S_e^2\mu_2+C_e^2\mu_3)\}/4c^2. \qquad (4.26)$$

The set of interchange operations $C \rightleftarrows S$, $\mu_2 \rightleftarrows \mu_3$,

$\nu_2 \rightleftarrows \nu_3$ corresponds to the transformation between the two sets of binary axes and corresponding (x-y-z) systems mentioned earlier (page 19). The transformation is reflected in the equations very simply : B_{24} and B_{42} change sign and all other coefficients are unchanged.

Since (4.26) consists of twelve equations in nine unknowns, three identities must exist. Two of them are known (Freedman and Juretschke 1961):

$$2B_{33} \equiv 3B_{11} - B_{12} - 2B_{44}$$

and $$4P_{231}(-2B_{44}\sigma_{11}/\sigma_{33} - B_{13})$$

$$\equiv P_{123}(4B_{31}\sigma_{11}/\sigma_{33} - 3B_{12} + B_{11} + 2B_{44}).$$

Later (page 144) these identities are assessed.

The remaining chapters of this thesis deal with the experimental measurement of the twelve magneto-conductivity coefficients and the application of the equations (4.26) to the galvanomagnetic effects in arsenic.

CHAPTER V

EXPERIMENTAL APPARATUS AND PROCEDURE

V.1. Problems Involved in Measuring the Galvanomagnetic Potentials.

By far the most common method of resistance measurement is to apply Ohm's law to measurements of current and voltage. This method requires sample contacts which may affect the voltage being measured, contaminate the sample or simply be very difficult to make, and in certain cases, contactless measurement methods may be advantageous. Usually they employ a 'Q'-meter technique (Miyamoto and Nishazawa 1967). In this work, conventional methods were used since small contacts could be made quite easily. Care was taken to avoid certain errors, principally Hall Field shorting.

The basic principle is straightforward: a primary current is passed through a rectangular bar sample in a magnetic field and suitably placed voltage probes pick up the appropriate galvanomagnetic voltage. Either alternating or direct current may be used; the galvanomagnetic coefficients are the same (Wood 1932).

Advantages of using d.c. stem from the d.c. potentiometer. It operates under open-circuit conditions and so does not load the voltage source; it may be directly calibrated to the standard cell, a fundamental voltage standard. Many years of development have resulted in instruments of high accuracy and stability. The ability to measure a small voltage change with a large standing voltage present is of paramount importance. The main disadvantage to the d.c. method is the slow, manual operation required: systematic averages of readings for forward and reversed directions of current and magnetic field are usually necessary to eliminate unwanted thermoelectric/magnetic effects. Even so, the Ettingshausen effect is not removed (see Putley 1960a).

A.C. methods (e.g. Donoghue and Eatherley 1951) inherently include current reversal, and if a double a.c. system (see Putley 1960b) is used, where the magnetic field is modulated, field reversal is included too. Amplification of very small voltages, to provide power to drive voltmeters or X-Y recorders, is straightforward. Hence using a.c., fast, automatic measurement is possible. The main drawback is the cost and complexity of the equipment required to select the signal and reject interference such as 50 Hz pick-up for the mains. Careful screening, both electrostatic and electromagnetic,

may be necessary. For the double a.c. method a metal cryostat may not be used because of the production of eddy currents.

An attempt to combine the advantages of both a.c. and d.c. methods by using synchronous chopping, has been made by Dauphinee (1955).

For the present work, the standard d.c. potentiometric method was adopted, partly because of its use for measurements on antimony (Oktu and Saunders 1967). However, detailed refinements were required to make accurate measurements of the small voltages involved. Preliminary measurements showed that the galvanomagnetic effects in arsenic are an order of magnitude smaller than in antimony; room temperature magnetoresistance is about 0.05% KG^{-2}. Therefore to measure the coefficients to an accuracy of 1% requires a system with a resolution of 5 parts in 10^6 and thus a drift stability of approximately 1 in 10^6. At room temperature, the resistivity of arsenic is such that a primary current of 5 amps through the sample produced some 3mV between the probes; the necessary resolution is equivalent to 15 nV and the noise level to 3 nV.

V.2. The Measuring System.

a. General description.

A block diagram of the measuring system is shown in figure 5.1. The potentiometer is a precision instrument (Pye type 7600) of the decade principle (see Stout 1960); switches are employed throughout. The smallest switched voltage step is 0.1 μV. The potentiometer has five input channels (A-E). For extra thermal insulation it is inside a wooden box lined with 1" thick expanded-polystyrene. Accumulators in series with a current regulator, described later (page 93), supply the current to the potentiometer. A similar regulator supplies the primary sample current via a junction box consisting of on/off and reversing switches, and a rheostat to set the current value which is indicated by an ammeter. The exact current value is obtained by measuring on the potentiometer the potential drop across a standard resistor (0.01Ω). The preamplifier-galvanometer detector (Pye type 11330) usually used with the potentiometer proved unsatisfactory for measuring at the nanovolt level, due to 0.1 to 0.2 μV short-term zero drift and a modified electronic millimicrovoltmeter (Keithley type 149) is used instead.

Stray thermal e.m.f.s in the measuring circuit are minimised by using copper wire throughout; connections

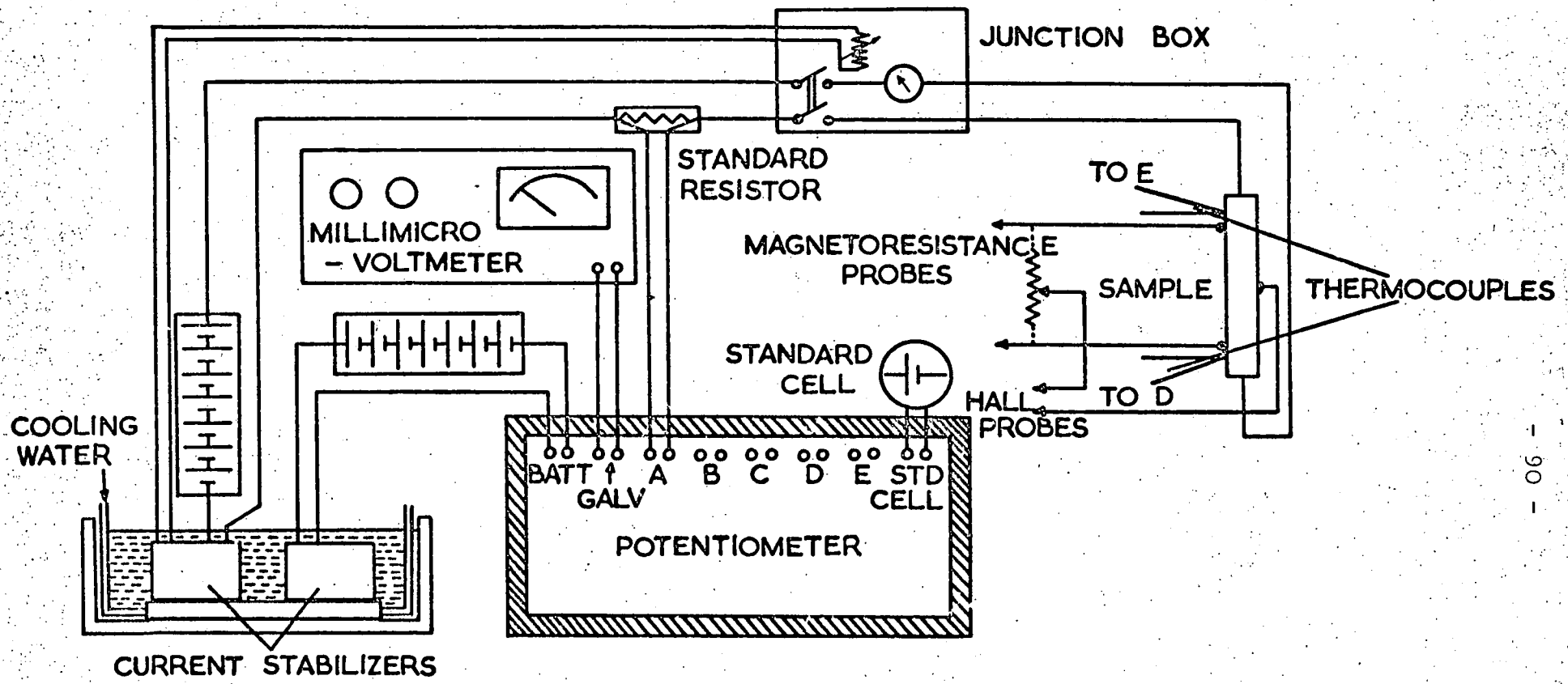

FIG 5.1. THE MEASURING SYSTEM

were carefully cleaned and clamped where possible; 'low thermal' solder (70% Cd 30% Sn) was used whenever soldering was absolutely necessary. Certain tap-key connections inside the potentiometer were shorted with copper wire. The rheostat (resistance 1Ω) used to balance out the 'IR' drop for Hall measurements is made of copper wire and submerged in a small oil bath.

b. Modifications to the millimicrovoltmeter.

Apart from freedom from zero drift, other advantages were gained by employing the electronic millimicrovoltmeter:-

1. Robustness
2. Fast response
3. High input resistance : very much greater power sensitivity.
4. 'Live' output for driving recorders.

But mains pick-up interference, the one drawback to an electronic detector was severe, largely due to the limited rejection built into the particular instrument used here. The latest Keithley instruments (models 140, 147, 148) have a rejection ratio one hundred times greater than the 149.

The instrument operates by chopping the input d.c., amplifying the resulting a.c. and reverting to d.c. by

synchronous demodulation before a final stage of d.c. amplification. The pick-up problem derives from the fact that the full-wave chopper is mains energised and the amplifier is peaked at 100 Hz. 50 Hz mains pick-up at the input to the chopper produces 50 and 150 Hz sidebands. These will be amply rejected by the synchronous demodulation. But some 100 Hz component resulting from sideband harmonics and/or cross modulation will inevitably appear. Moreover, such a signal will be locked to the desired signal of chopped d.c.: the controlling factor in both cases is the 50 Hz mains. Consequently, this interference will be distinguishable from the signal, apart from a possible phase difference, and will be demodulated in the normal way. It would not matter if the amount of pick-up were constant; readings could be made by difference. But this was not so due to the operation of machines or lights elsewhere in the laboratory. In fact the switching operature of the growth furnace - described in chapter III - situated upstairs, could be monitored with ease !

Two solutions are possible : the pick-up may be reduced to a negligible level or the instrument (149) modified to chop at a frequency different from 50 Hz to ensure that no sideband products occur at the signal frequency. A chopping frequency of 94 Hz is used in

the model 148. The first policy was pursued vigorously :-

1. The position and orientation of the apparatus and all circuit wiring was varied to minimise pick-up.

2. A hum loop in the potentiometer was removed by rerouting a wire.

3. The mains transformer in the 149 proved to be a pick-up source. It was disconnected and duplicated by a transformer remote from the instrument.

These measures were insufficient and so the second remedy was invoked. The 149 was modified to operate from 60 Hz, the highest frequency at which the chopper would still vibrate. A signal generator(Advance type J2C) is coupled to the chopper by a matching transformer. A second output on the generator provides the demodulator signal via a 10:1 step up transformer to attain the required voltage; a full wave bridge circuit provides frequency doubling. A capacitor was changed inside the 149 to peak the amplifier to the new frequency. The exact operating frequency had to be tuned carefully to avoid slow oscillations in the 149 output due to beating between harmonics or product frequencies of 50 Hz mains and 60 Hz chopping frequencies.

V.3. Sample Current Control : the Current Regulator.

Any fluctuation in the primary current flowing

through the sample will reflect as a voltage change at the measuring probes. These fluctuations must be held to 1 in 10^6 to avoid measurement errors, as explained in section V.1. Usually, a stability of 1 in 10^3 or 1 in 10^4 is sufficient and is achieved by separate monitoring and manual control. This method proved quite impractical in this case and a transistorised current stabiliser (Palmer 1966) is employed; figure 5.2 shows the circuit diagram. The stabiliser places an apparent, high resistance (about 50 KΩ) in series with the sample. Then any temperature, or otherwise, induced resistance change in the sample or connecting leads comprises only a very small fraction of the total circuit resistance and the resulting current change is very small.

Circuit operation is as follows :-

R_s samples the circuit current and provides a voltage that is compared to the voltage across the Zener diode MRZ_2. The difference voltage is amplified by VT_2 and used to control the voltage across VT_4 and VT_5, which form a series element in the current circuit. A negative-feedback loop exists: a shift in the voltage across R_s causes a change in the voltage across VT_4 and VT_5 which restores the voltage across, and therefore

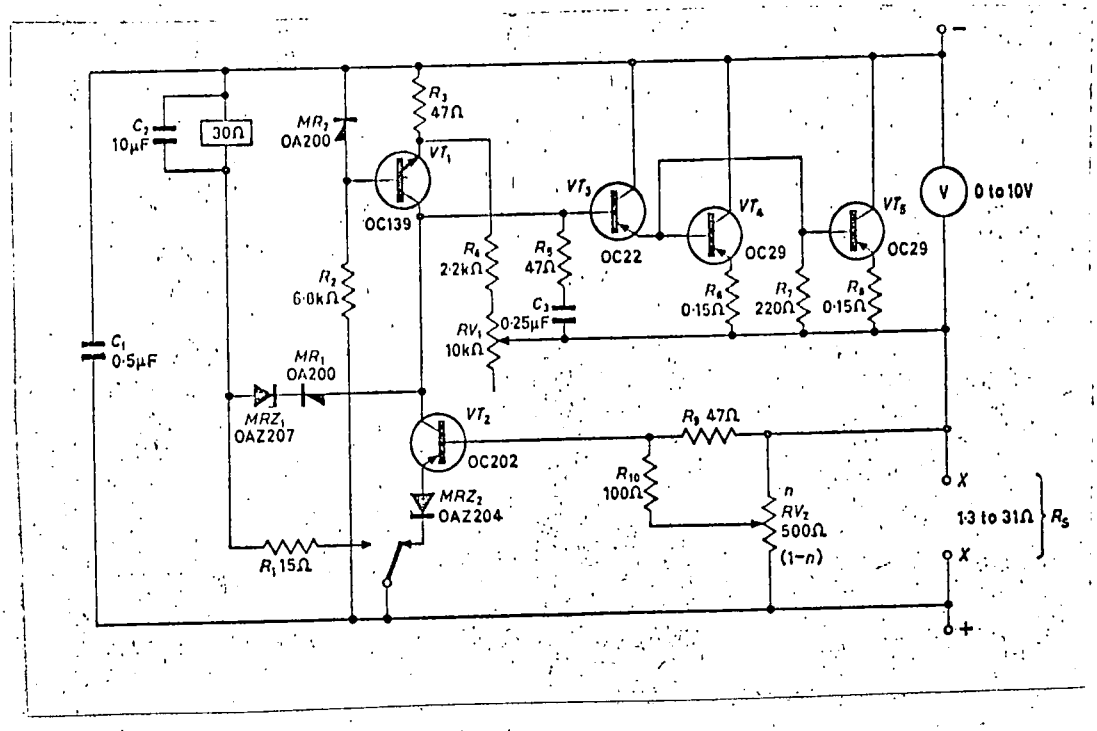

Figure 5.2.

Circuit diagram of the current regulator.

current through, R_s.

To remove drifts caused by temperature changes in R_s and MRZ_2 the complete stabiliser is immersed in a bath of industrial paraffin, cooled by tap water from a constant head running through a finned heat exchanger. After an initial 'warm-up' of 1 - 2 hours, the primary current (5 amps) could be held steady to better than 1 in 10^6 over a period of ten minutes and was quite unaffected by severe (about $10^{\circ}C$) temperature changes in the sample or connecting leads.

V.4. The Temperature Control System.

a. Description.

Temperature variations of the sample can give rise to spurious voltages at the measuring probes in two ways:

1. A differential temperature change between the probes, acting through the Seebeck effect ($\sim$10 $\mu V/^{\circ}K$ at room temperature).

2. A bulk temperature and therefore resistance change: the temperature-resistivity coefficient is 0.45% $^{\circ}K^{-1}$. On both counts it transpires that a temperature regulation to within $0.001^{\circ}K$ is prerequisite to achieve the overall stability of 1 in 10^6. The usual technique is to insert the sample into a cryostat and

manually balance the heat input (electrical heating) and output (cryostat interspace pressure) to stabilize sample temperature. This is a time consuming operation to achieve a stability of 0.05°C and it is impractical to the fine limit required here. Therefore, a system of automatic control of electrical heating was devised.

Many descriptions appear in the literature of temperature control systems, ranging from a single photo-transistor device (Woodhams et al. 1966) to elaborate a.c. systems for use at helium temperatures. Negative feedback is the underlying principle: the signal from a temperature sensor is amplified and fed back to a heater to offset any temperature change. D.c. systems often employ thermocouples (Zabetakis et al. 1957); a.c. a resistance thermoneter and bridge (White 1953). A survey may be found in White (1959).

The sensitivity required in this case implies a high degree of amplification: an a.c. system was constructed. It is based on a design by Wilson and Stone (1957). Phase-sensitive detection is employed to increase the sensitivity (Faulkner et al. 1965). Figure 5.3 shows a block diagram of the electronic apparatus; operation is straightforward. The copper-resistance thermometer in the cryostat senses any temperature change and produces an out of balance signal from the a.c. Wheatstone bridge.

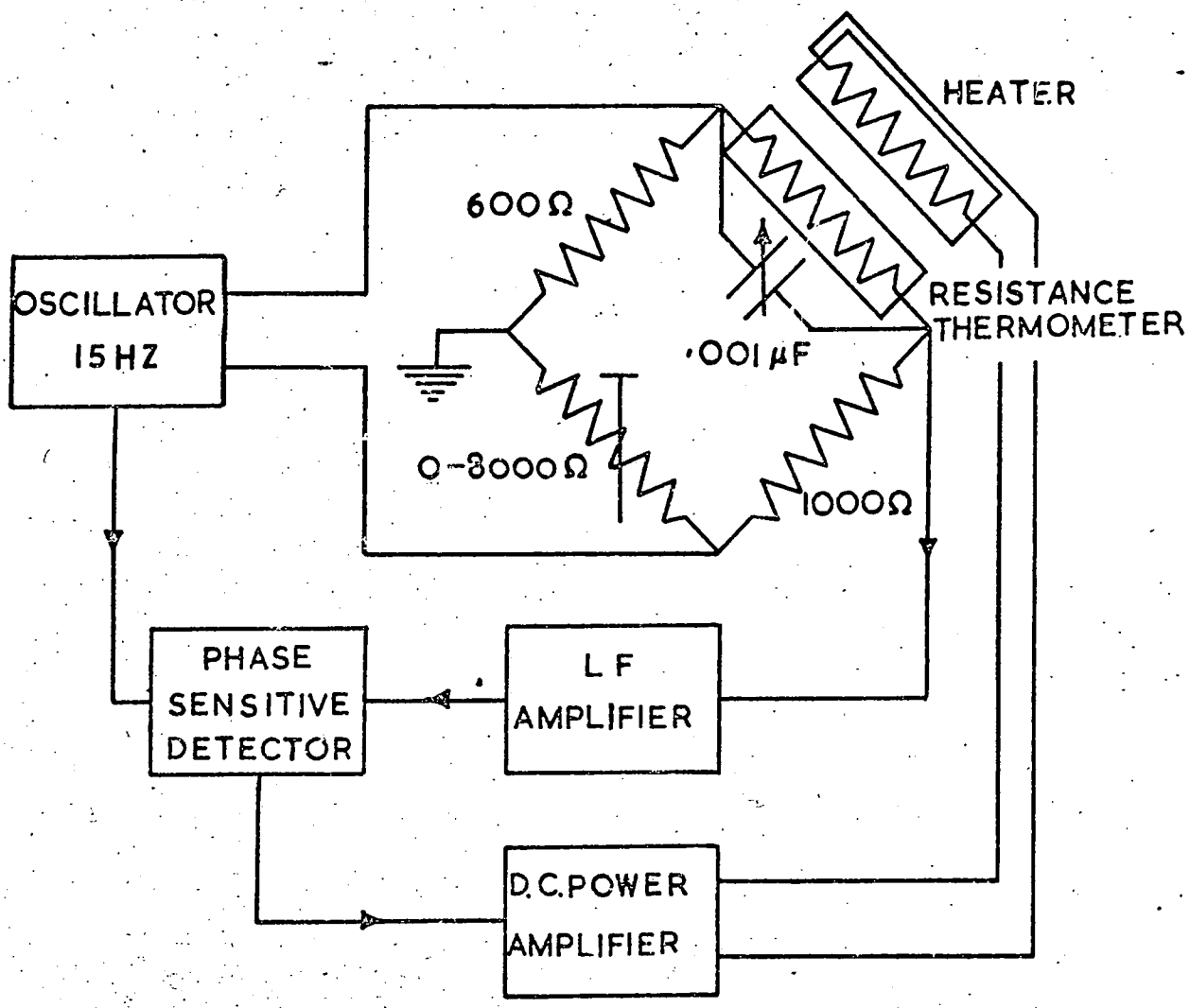

Figure 5.3.

A block diagram of the system of automatic temperature control.

This is amplified, passed through a phase-sensitive detector and power amplified (d.c.) to feed back to the heater in the cryostat. Details of the individual stages are now presented.

b. The cryostat.

The cryostat is illustrated in figure 5.4. Basically it is a stainless steel Dewar flask inside a glass tail Dewar flask (Lark-Horovitz and Johnson 1959). All the wires to the sample run inside a 0.5" diameter german-silver tube that supports the copper sample-holder. To facilitate isothermal conditions, the sample is surrounded by a liquid. The sample temperature may be roughly set by adjusting the interspace pressure of the metal Dewar flask to control the heat leak to the coolant in the glass Dewar flask. For measurements at 305^{o}K the metal Dewar flask contains industrial paraffin and the glass Dewar flask ice/water. For lower temperatures the ice/water is replaced by liquid nitrogen and the paraffin by isopentane, liquid down to 113^{o}K. The non-flammable, five-component eutectic used by Oktu and Saunders (1967) was not used owing to its appreciable electrical conductivity. Stirring the liquid around the sample was tried with a completely immersed stirrer, comprising a 2V electric motor, geared down to rotate a paddle. But it was not successful: heat input to the cryostat from

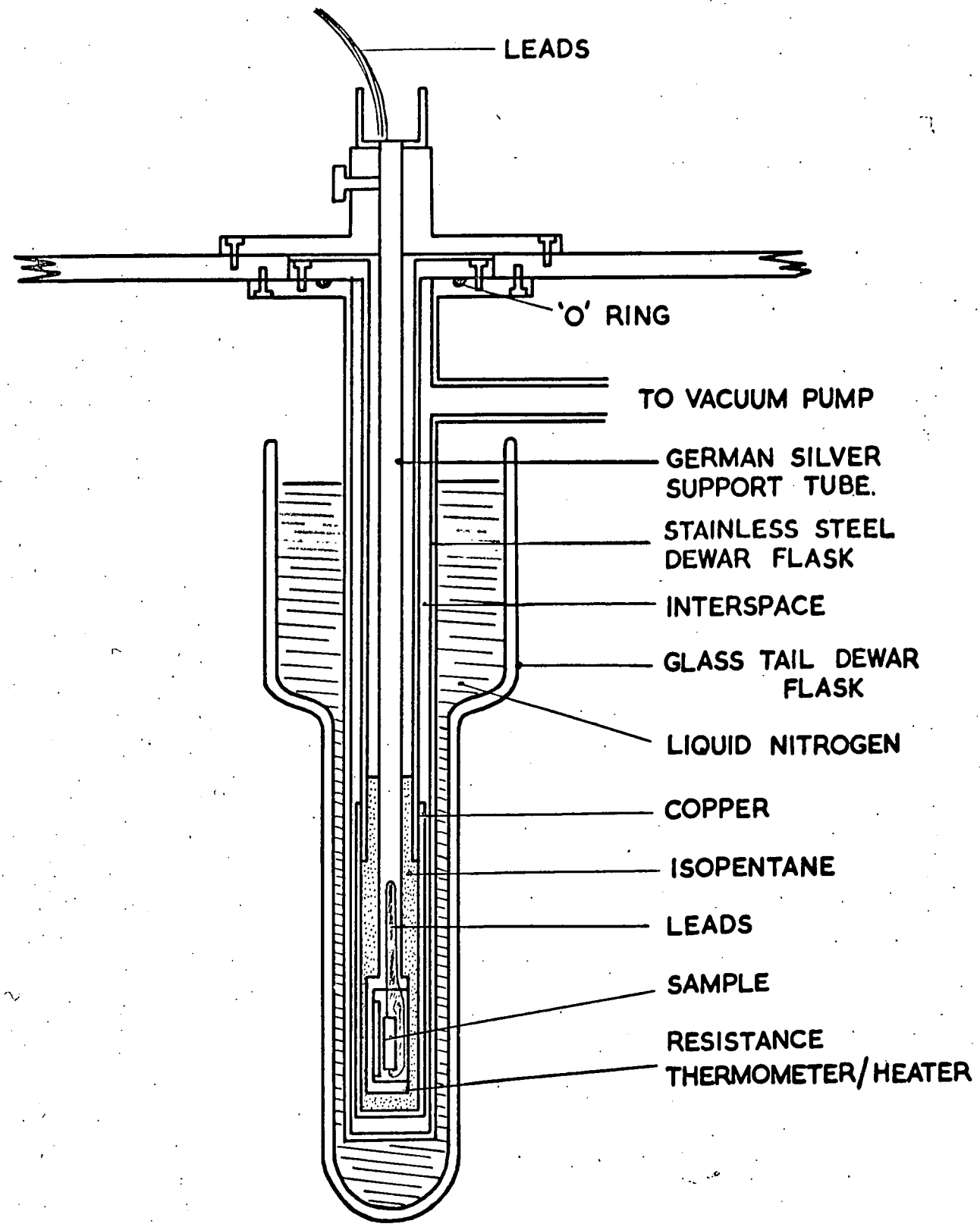

FIG. 5.4 THE CRYOSTAT.

the electric motor, and vibration were prohititive. Fortunately, convection currents sufficed.

c. Resistance thermometer and electrical heater.

The sensing arm of the Wheatstone bridge is wound noninductively, on an open 'birdcage' former 4" long and 1" in diameter to maximise contact with the cryogenic liquid, to a resistance of 600Ω from 48S.W.G. enamelled copper wire. A thermistor was not used, despite greater sensitivity, as its small size would enable only a small part of the experimental space to be sensed. Also the linearity of the change in resistivity of copper with temperature is useful.

Close contact is necessary between the resistance thermometer and heater to avoid hunting due to a long time constant for the thermometer to sense the heater. Therefore the 100Ω heater is wound helically over the resistance thermometer.

d. Wheatstone bridge.

If X denotes the resistance of the resistance thermometer which is compared to arm C of the Wheatstone bridge with ratio arms A and B then: $X = C.A/B$. For stability, the value of C and of the ratio A/B must not change. C is wound from 36 S.W.G. manganin wire to

600Ω on a small plastic bobbin and immersed in oil in a Dewar flask. A and B form a five-decade resistance box (Pye 7630): A is one 1000Ω coil and B is the rest of the box which is switched to set any desired temperature. Since A and B are in the same box, and have identical temperature-resistance coefficients, any temperature change affects them equally, so that A/B remains constant. Twin core screened cable is used to connect the bridge arms; the resistance contribution of the leads is minimised. A variable capacitor of 0.001μF across X facilitates a phase balance.

Only one volt of a.c. from a signal generator (Advance type J2C) is applied to the bridge to minimise power dissipation in the bridge arms. The frequency of 15 Hz is as low as practical to avoid reactive effects. A step-up (60:1) transformer matches the bridge output (about 500Ω) to the amplifier input (2MΩ). 35 dB voltage gain results.

e. Amplification (a.c.), phase detection.

A commercial solid-state amplifier is used (Brookdeal, model EL355). Maximum gain is 100 dB; 75 dB of attenuation, switched in steps of 5 dB is available. The phase sensitive detector (Brookdeal MS320) - subsequently written as PSD - incorporates a reference

phase amplifier and phase shifter. Faulkner & Stannett (1964) and Nancollas and Hardy (1967) have described amplifiers and phase sensitive detectors that could also be used.

f. The class-D d.c. amplifier.

The power needed for the heater is about 1 watt. Since only 1 mW is available from the PSD, further d.c. power amplification of 1000 X is required; a modification to the PSD was considered inadvisable. The output of the PSD is 1 volt at 1 mA; the heater requires 10 V at 100 mA, so a voltage gain of 10 and current gain of 100 is required. The common emitter circuit is a convenient current amplifier, being relatively stable due to inherent full negative feedback. But a stage of voltage gain would also be required and d.c. voltage amplifiers require careful design and compensation to overcome drift problems. To avoid this, a class-D amplifier was designed. Block and circuit diagrams are shown in figure 5.5. The transistors are used as switches; high efficiency and stable amplification results.

The heart of the amplifier is the Schmitt trigger (TR7 and 8) (see Hampshire 1967). This is a flip-flop circuit: the two stable states are TR7 on TR8 off, or TR7 off and TR8 on, and the circuit is triggered from one state to the other as the input voltage to the base of

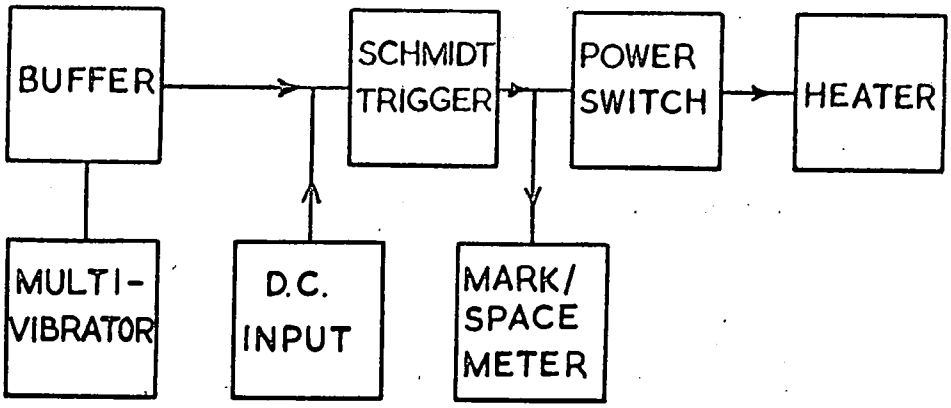

a. BLOCK DIAGRAM

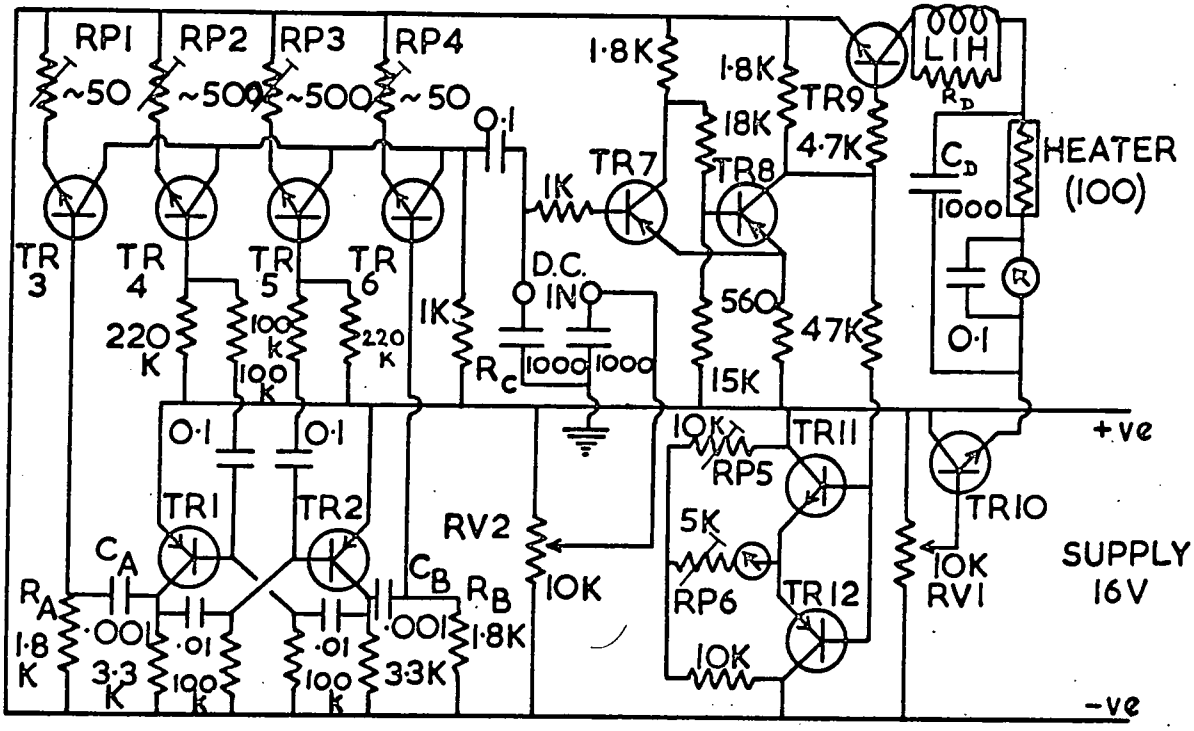

C in μF; R in Ω.

b. CIRCUIT DIAGRAM

FIGURE 5·5 The Class-D Amplifier

TR7 crosses a critical or threshold voltage. If a modulating voltage (e.g. sine wave) is applied to the input, square waves result from the TR8 collector which moves from the negative rail potential to emitter potential when TR8 switches on, and vice versa (figure 5.6a). A d.c. bias is now added to the modulating waveform. As the bias changes, the width of the squarewave pulses and therefore their power content varies (figure 5.6b and c). This power is fed to the heater; the variable d.c. bias comes from the PSD.

A sine wave is not the ideal modulation for the Schmitt trigger. A ramp waveform will give voltage and current lineaity. Inherent backlash in the Schmitt trigger threshold voltage means that the maximum pulse width is restricted (figure 5.6d) and thus the range of control is limited. This may be overcome by adding a spike, at least as large as the backlash, to each peak of the ramp. Then the limiting pulse width is close to full width (figure 5.6e). A sawtooth waveform is simpler to generate and serves just as well; only one spike is required (figure 5.6f).

The waveform of figure 5.6f is generated by a multivibrator (TR1,2) operating at a compromise frequency of 1000 Hz: well away from bridge (15 Hz) and mains

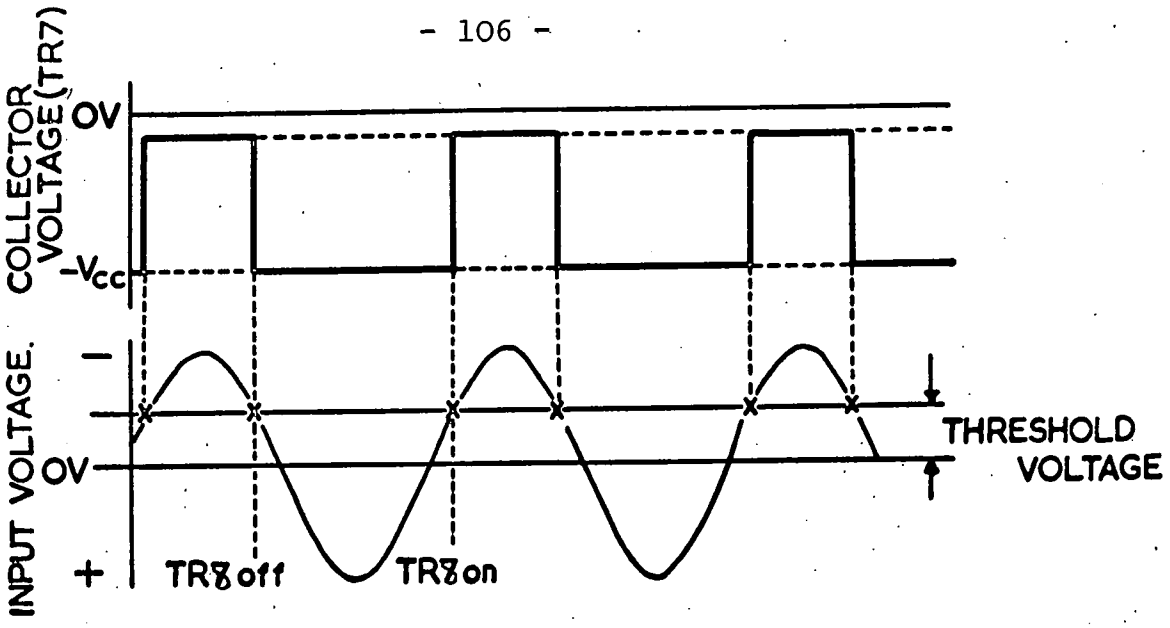

Figure 5.6 a.

The production of square waves from the Schmidt trigger.

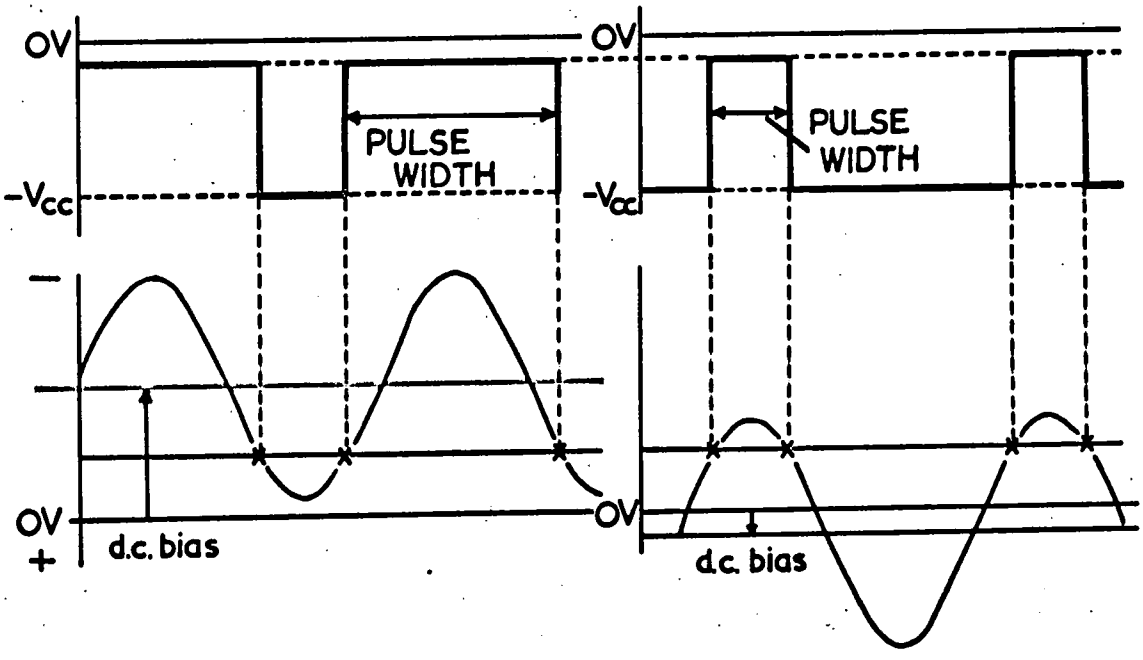

Figure 5.6 b

Figure 5.6 c

The width of the square pulses varies as the input d.c. bias is changed.

FIG 5.6 a-c. SCHMITT TRIGGER OPERATION

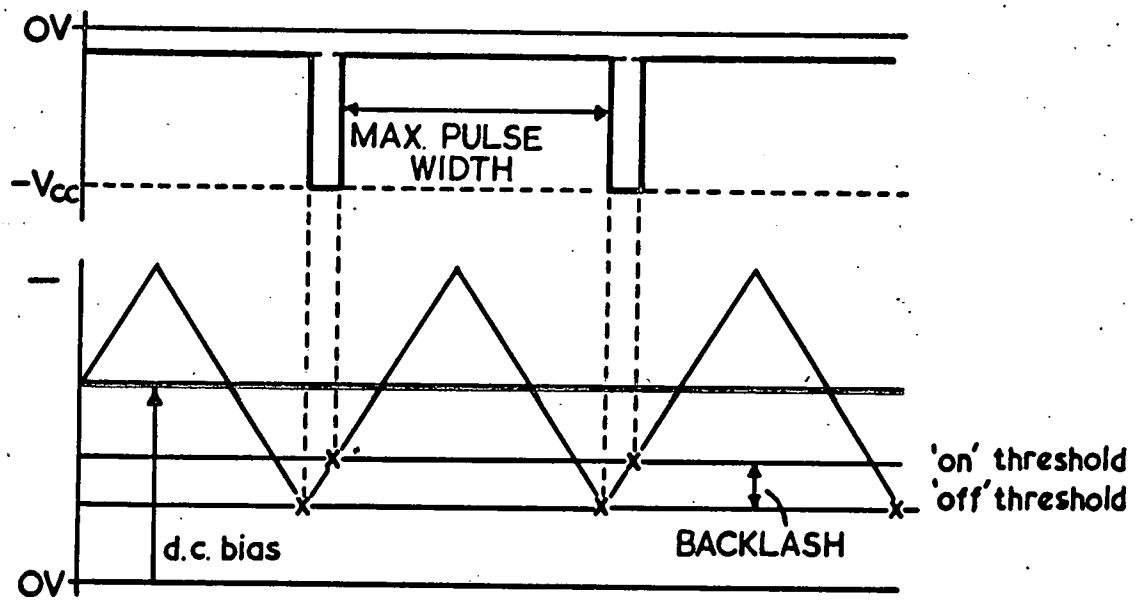

Figure 5.6. d.

'Backlash' in the trigger limits the maximum pulse width.

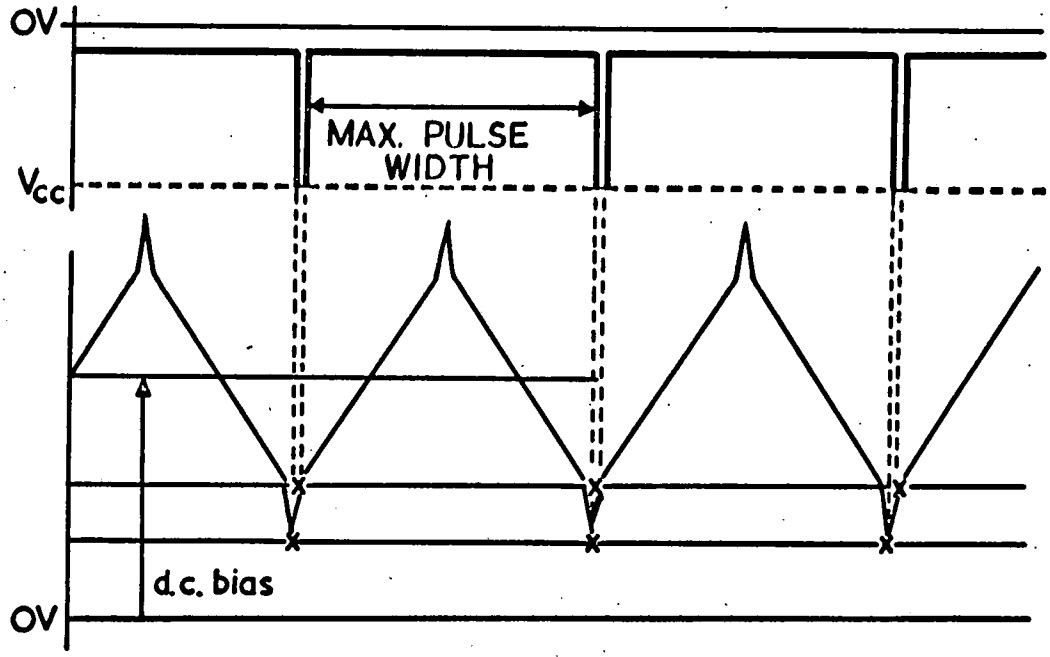

Figure 5.6 e.

Adding a 'spike' to the waveform increases the maximum pulse width.

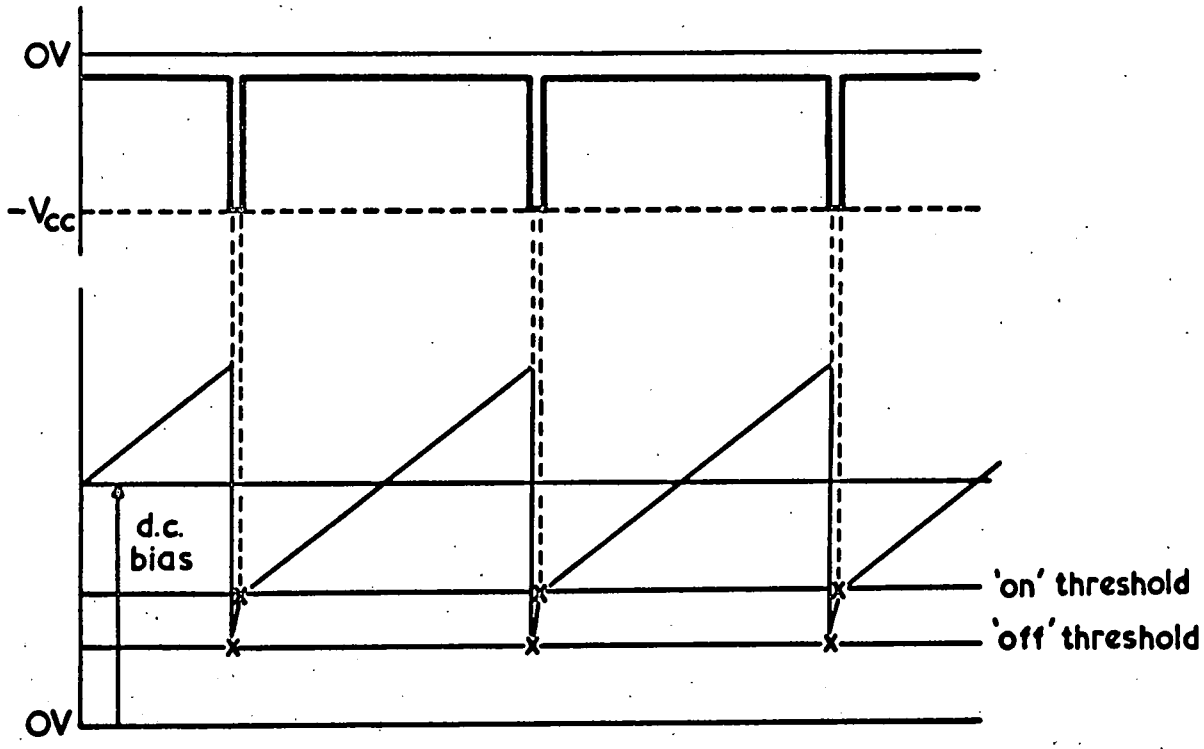

A sawtooth waveform serves just as well as a ramp.

FIG. 5.6 (cont.) f

(50Hz) frequencies, to minimise pick-up but low enough to maintain switching. The sawtooth waveform comes from the bases of TR1, 2 via TR4,5 which buffer the multivibrator and current amplify to provide a low (1 KΩ) output impedance. The spikes are obtained by differentiating the squarewaves at the collectors of TR1,2 with $C_A R_A$, $C_B R_B$ and buffering with TR3,6. The components of the waveform are summed in the common collector resistor R_C; individual amplitudes may be balanced by setting RP1,2,3,4.

It is essential to feed the heater with d.c. If a.c. is used, considerable vibration of the sample-holder is caused by the Lorentz force produced when the magnetic field is applied to the sample. TR9 is a power switch to supply the heater; d.c. results from the integrating circuit L, R_D C_D. To maintain the full switching action of TR9 R_D must be adjusted: its value is approximately equal to the heater resistance. L must have sufficient inductance to prevent pulse 'droop' or 'overshoot'. TR10 operates as an emitter follower to establish the voltage to TR9 and thus the squarewave amplitude: the power corresponding to a given pulse width is set by RV1.

The operation of the amplifier is monitored by TR11, 12 a complementary pair of transistors which monitor the pulse width by measuring the mark-space ratio.

TR11 turns on when the square wave goes positive and TR12 when it goes negative. For an equal mark-space ratio, equal currents flow in the emitters of TR11, 12 but of opposite phase: the centre-zero meter integrates to zero once the circuit has been balanced by adjusting RP5. RP6 sets the meter sensitivity. To set up initially, an equal mark-space ratio is established by monitoring with an oscilloscope. Then RP5 is adjusted for a zero meter reading. The amplifier is reset to maximum pulse width, in either sense, and RP6 set for maximum meter reading.

RV2 is set so that zero voltage input from the PSD corresponds to an equal mark-space ratio.

g. Operating the temperature control system.

1. Set the switched arm of the Wheatstone bridge to the appropriate value for the temperature required.

2. Set the cryostat interspace pressure. Both of the above settings must be learnt by experience !

3. Set the a.c. amplifier to minimum gain.

4. Switch on the electronic equipment. Adjust the voltage (1V) to the Wheatstone bridge, and the reference phase gain.

5. When the temperature is within the control band of the electronic system, observe the non-integrated signal output of the PSD on an oscilloscope and set the phase-shifter

so that the reference signal is in phase.

6. Connect the output of the PSD to the class-D amplifier. Adjust the amplitude control (RV1) to give sufficient power to balance the system at an equal mark-space ratio (zero meter reading).

7. Increase the amplifier gain as desired, but avoid hunting: indicated by the mark-space meter oscillating to and fro.

8. Repeat (6) after one hour.

Once established, the temperature remains quite stable until the heat input to the cryostat is altered, e.g. by switching off the sample current.

It is very difficult to assess the control of the temperature control system in terms of fractions of a degree (see Hutchinson et al. 1954). All that can be said is that when all the equipment, including the millimicro-voltmeter and current stabilizers, had been turned on for a few hours, the voltage drop along the sample remained at 3 mV $\pm$ 3nV($\sim$1 in 10^6) over a period of 10 minutes (figure 5.7): the experimental problems had been solved.

V.5. Experimental Technique.

a. Sample preparation.

Rectangular bar samples (2 x 0.2 x 0.2 cm) were spark cut from crystals orientated by reference to the (111) cleavage plane and slip lines thereon that mark

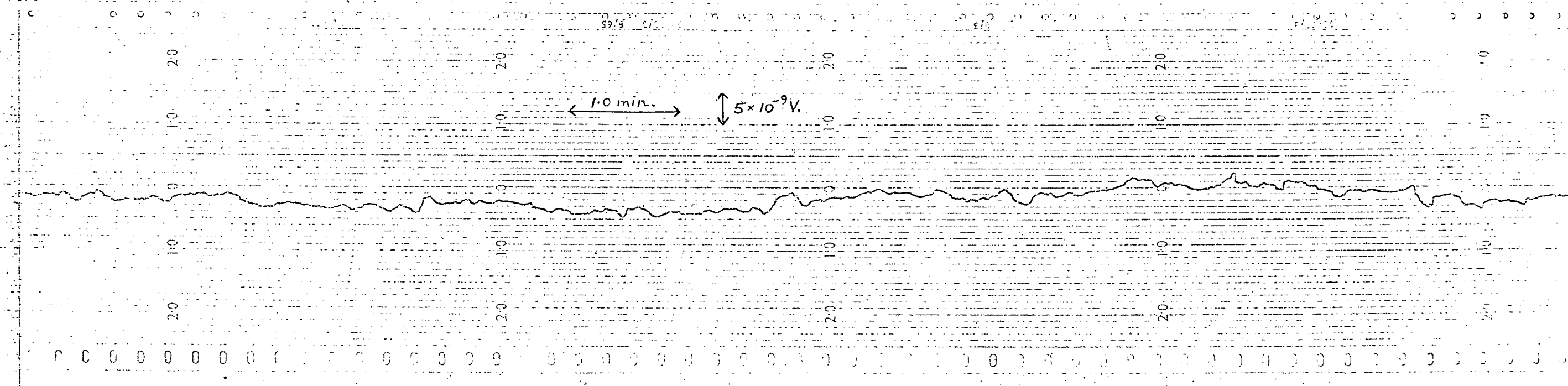

Figure 5.7.

The potential drop along an arsenic sample after a steady temperature had been established. Drift is within 5×10^{-9} V over a period of more than 10 minutes.

the binary axes. Considerable care was necessary when cutting to prevent fracture or cracking due to the strong (111) cleavage; it was found essential to avoid cutting in the trigonal direction. Size was measured with a travelling microscope.

Three different methods of making contacts were tried:-

1. Small arms were machined on the sample (Debye and Conwell 1954). This is probably the best method, offering the least disturbance of the isopotentials and no sample contamination. But the difficulty of cutting the most fragile probes was prohibitive.

2. Spark-welding was also tricky. Contacts could be made but the usual result was a pit at the point of sparking. Presumably vapourization occurs unless some pressure is present to enable melting, since arsenic sublimes so readily.

3. Soldering was the method adopted. Voltage probes were of 0.002" diameter copper wire soldered to the sample with a low melting point ($95^{o}C$) alloy (32% Pb - 16% Sn - 52%Bi) and positioned well away from the sample ends to minimise Hall field shorting (Volger 1950); contact diameter was about 0.01".

To detect any longitudinal temperature gradient,

copper-constantan thermocouples were soldered to each end of the sample which was mounted rigidly, on an alignment mechanism in the sample holder at one end only (figure 5.8) to prevent damage due to contraction on cooling.

b. The magnet: field alignment.

Since most of the magnetoresistivity coefficients are proportional to H^2, an accurate knowledge of magnetic field strength is important to avoid errors. The magnet was calibrated initially by nuclear magnetic resonance and subsequently a systematic procedure was used to avoid hysteresis errors (figure 5.9): field values were always set by increasing the magnet current, finishing at saturation. The magnet current was not reversed; the magnet was rotated to reverse the magnetic field and to establish the various orientations. The magnetic field and sample were centralised on the axis of rotation. Sample alignment in the magnetic field was achieved mechanically by reference to the plane pole-tip faces. Magnetoresistance polar diagrams were not used for this: they could only be measured in the assembled apparatus and rely on exact probe positioning on the sample.

c. Field reversals.

Magnetic field reversal was employed to remove error voltages due to inexact probe positioning and to separate Hall and magnetoresistance coefficients (see page 130)

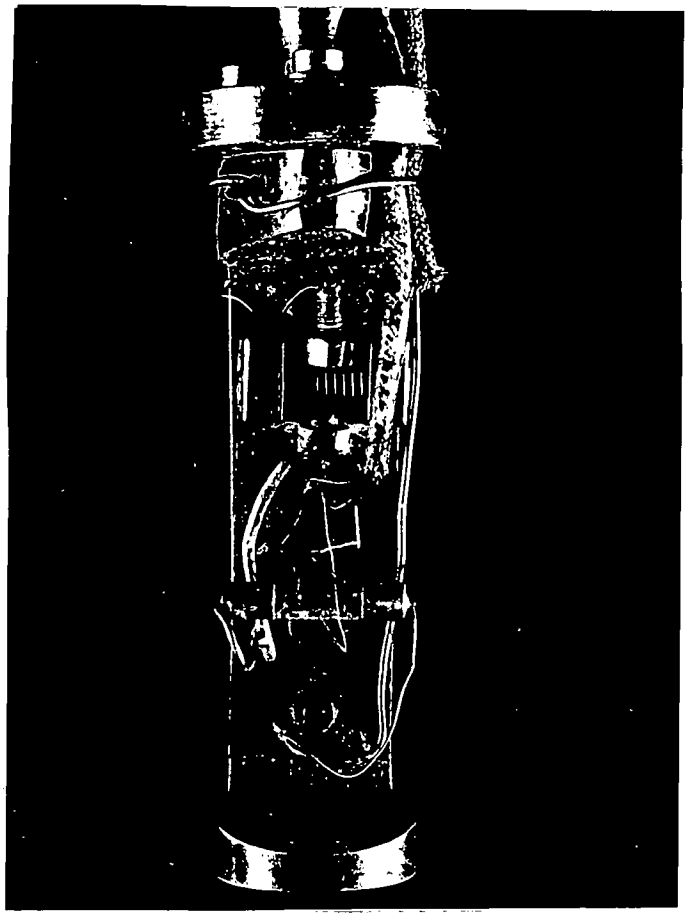

Figure 5.8.

An arsenic sample mounted in the sample holder. Only one end (the left) is firmly secured.

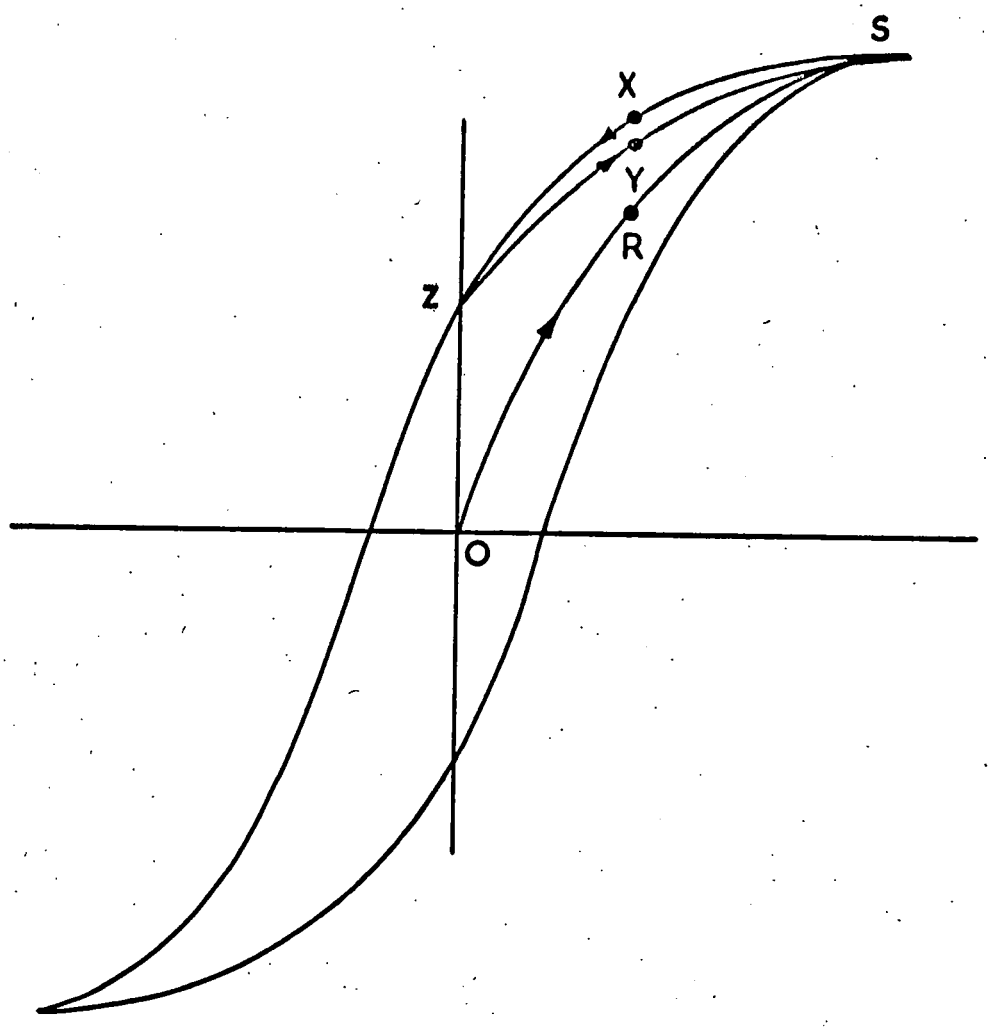

Figure 5·9.

Avoiding hysteresis errors when setting the magnetic field: The magnet current is increased to field saturation (S) from zero (i.e. line ORS). Decreasing the field to zero and back to saturation then follows the path SXYS. A further cycle will follow the same path. Thus hysteresis errors are avoided if the field values are attained after the magnet has been saturated. In this work, the path ZYS was used.

The standard procedure of reversing the primary current was not used because of interference from the Peltier effect arising from the use of a large primary current (5 amps) for this relatively highly conductive semimetal. The required galvanomagnetic voltages are proportional to current; it is necessary to eliminate error voltages independent of current. These arise from Seebeck voltages due to standing temperature gradients in the sample and contact potentials in the sample or measuring circuit; usually they are removed by reversing the current and averaging. However, in this work a temperature gradient could appear along the sample due to Peltier heat being absorbed at one current contact and emitted at the other. Since the Peltier effect is proportional to current, reversing the current reverses this temperature gradient; the error voltage is an intimate part of the ohmic voltage and cannot be averaged away. To overcome this a trick was adopted; the sample being mounted at one end only, heat transference from this end was better than from the other. Coupled with Joule heating in the sample, this was used to produce a temperature gradient that opposed the Peltier gradient. Isothermal conditions could be attained by adjusting the current to obtain a balance between these two effects. Fortunately the optimum current value ($\sim$5amps)

was also acceptable from considerations of sensitivity and practicability.

d. Measurement procedure.

It was hoped that automatic plotting of galvanomagnetic potentials against magnetic field on an X-Y recorder would be possible. But it was not; even at a slow sweep rate of five minutes per kilogauss, the steadily increasing magnetic field induced a direct voltage of 0.1μV via the loop area enclosed by the probe leads. Introducing an antiphase loop was tried, but it was a complex matter to do this for all field orientations. The problem may be illustrated by the fact that a 3" diameter loop moved slowly in the earth's magnetic field will generate several nanovolts. Point by point plotting at static magnetic fields was necessary; the stability of the equipment enabled a field range of 0.7 to 4.7 kilogauss to be covered in twelve steps without the need to restandardise the potentiometer or reset the primary current. The measurement procedure is as follows :-

1. Switch on all apparatus and establish the sample temperature as described on page 110.

2. Set the magnetic field orientation. Run the magnet current up to maximum and back to zero two or three times to eliminate any hysteresis error (page 116).

3. Check the a.c. pick-up to the millimicrovoltmeter with an oscilloscope.

4. Standardise the potentiometer. Set the sample current accurately and check for any longitudinal temperature gradient in the sample.

5. Switch the potentiometer to measure the required sample voltage; check for drift.

6. Measure the voltage at the desired field values as the magnetic field is increased.

7. Recheck the voltage with the magnetic field back to zero.

Typical results are shown in table 5.1. In certain cases the voltage measured at H = 0 after the field sweep differed from its value before the sweep, although a check over a similar time interval revealed negligible drift if no magnetic field was applied. Presumably the magnetic field causes a thermal disturbance in the sample through other galvanomagnetic effects (e.g. Ettingshausen): a voltage is produced by the Seebeck effect. This is a second-order effect and is not significant, but an allowance was made by incrementing (or decreasing) each reading on the assumption that the drift was uniform with time and that each reading took the same time.

Magnetic Field (Gauss)	V_J (μV) + .005 μV $\phi = 45^\circ$	$\phi = 135^\circ$	$\phi = 225^\circ$	$\phi = 315^\circ$
0	3266.312	3266.288	3266.356	3266.339
1000	6.626	6.026	6.228	6.740
1400	6.827	5.941	6.226	6.943
1800	7.038	5.846	6.253	7.157
2200	7.279	5.790	6.306	7.380
2600	7.550	5.745	6.377	7.638
3000	7.842	5.724	6.473	7.896
3400	8.147	5.736	6.592	8.166
3800	8.470	5.764	6.748	8.446
4200	8.831	5.818	6.918	8.744
4600	9.230	5.888	7.114	9.068
0	3266.324	3266.285	3266.400	3266.394

Table 5.1.

A typical set of measurements. The apparently negative magnetoresistance for $\phi = 135^\circ$ and $\phi = 225^\circ$ is due to interference from a Hall voltage. Averaging for ϕ, $\phi + 180$ eliminates this. See page 130.

CHAPTER VI

EXPERIMENTAL CONFIGURATIONS AND RESULTS.

VI.1. Crystal Configurations for Determining the Twelve Magnetoresistivity Coefficients.

In this section, the example of configuration discussed in chapter IV (page 66) is developed according to the method of Epstein and Juretschke (1963) to provide a systematic scheme for measuring all twelve magnetoresistivity coefficients.

Figure 6.1 shows two convenient crystal orientations: the trigonal axis is normal ($\underline{J} \perp Z$) and parallel ($J \parallel Z$) to the longitudinal sample axis respectively. In both cases, $\underline{H}$ is rotated away from the z-axis by an angle ϕ, in a plane (the H-plane) that makes an angle η with the bisectrix axis. For $\underline{J} \perp Z$, the crystal is cut so that the binary axis is at an angle θ, approximately 15°, to the sample length; for $\underline{J} \parallel Z$ the x, y axes are parallel to the width and thickness of the sample. Expressions are now developed for the various galvanomagnetic fields.

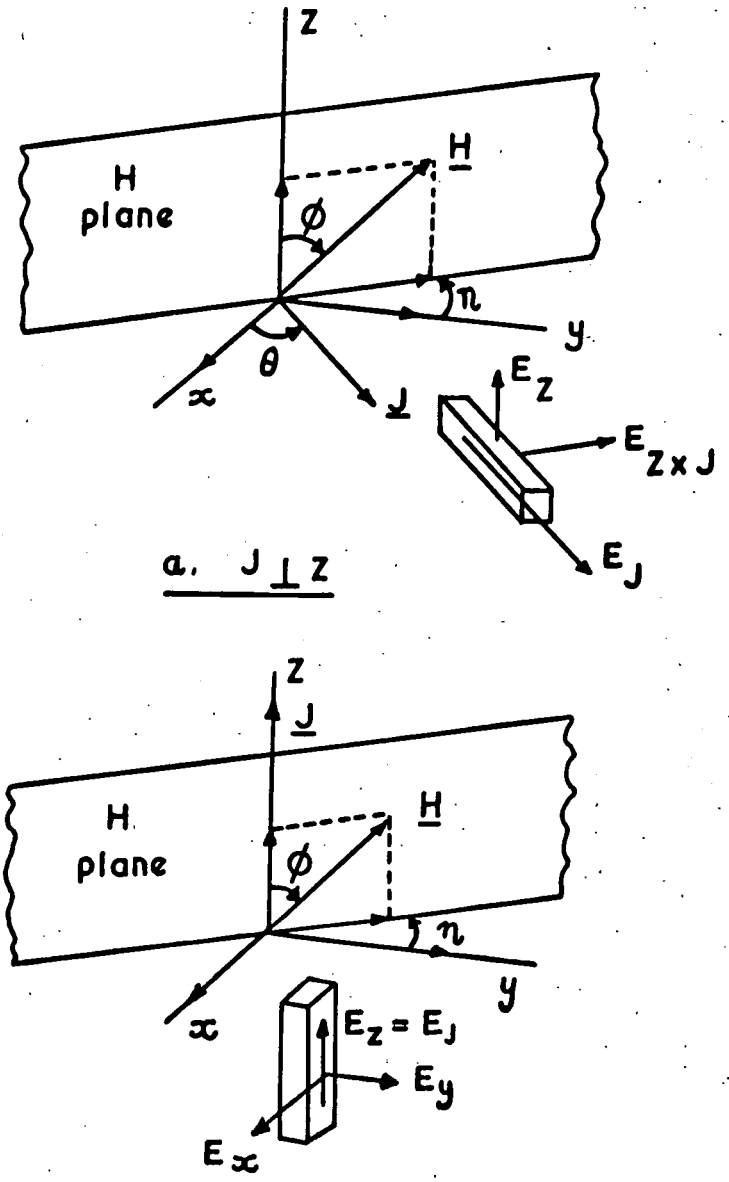

Figure 6·1. Two General Crystal Orientations

$\underline{J} \perp Z$ (figure 6.1a)

As before, the first step is to resolve $\underline{J}$ and $\underline{H}$ into components referred to the x, y, z (1, 2, 3) axes.

$$J_1 = J \cos\theta;\ J_2 = J \sin\theta;\ J_3 = 0$$

$$H_1 = H \sin\phi \sin\eta;\ H_2 = H \sin\phi \cos\eta;\ H_3 = H \cos\phi. \qquad (6.1)$$

There are three galvanomagnetic fields that may be measured: the longitudinal field E_J and two Hall fields, E_Z and E_{ZXJ}. E_J is summed from components:

$$E_J = E_1 \cos\theta + E_2 \sin\theta \qquad (6.2)$$

$\underline{E}$ and $\underline{J}$ are related by equations (4.2);

$$E_1 = \rho_{11}(\underline{H})J_1 + \rho_{12}(\underline{H})J_2 + \rho_{13}(\underline{H})J_3$$

$$E_2 = \rho_{21}(\underline{H})J_1 + \rho_{22}(\underline{H})J_2 + \rho_{23}(\underline{H})J_3.$$

$$E_3 = \rho_{31}(\underline{H})J_1 + \rho_{23}(\underline{H})J_2 + \rho_{33}(\underline{H})J_3$$

Substituting these equations into (6.2) with (6.1):

$$E_J = J\,(\rho_{11}(\underline{H})\cos^2\theta + \rho_{12}(\underline{H})\cos\theta\sin\theta$$

$$+\rho_{21}(\underline{H})\cos\theta\sin\theta + \rho_{22}(\underline{H})\sin^2\theta). \qquad (6.3).$$

The components of $\rho_{ij}(\underline{H})$ are now fed in, according to the equations (4.4) which connect the nine components to the twelve coefficients. Then:

$$E_J = J \{ \cos^2\theta(\rho_{11} + A_{11}H_1^2 + A_{12}H_2^2 + A_{13}H_3^2 - 2A_{24}H_2H_3$$

$$+\cos\theta\sin\theta(2(A_{11}-A_{12})H_1H_2 - 4A_{24}H_1H_3)$$

$$+\sin^2\theta(\rho_{11}+A_{12}H_1^2+A_{11}H_2^2+A_{13}H_3^2+2A_{24}H_2H_3)\}.$$

Substituting for H_1, H_2, H_3 according to (6.1) and simplifying, for the case that $\underline{J}$ is normal to the H-plane, i.e. $\theta = \eta$:-

$$E_J = \rho_{11}J + JH^2(A_{12}\sin^2\phi + A_{13}\cos^2\phi - A_{24}\cos3\theta\sin2\phi); \quad (6.4a)$$

The corresponding expressions for E_Z and $E_{Z\times J}$ are:-

$$E_Z = JHR_{231}\sin\phi + JH^2A_{42}\sin3\theta\sin^2\phi; \quad (6.4b)$$

$$E_{Z\times J} = -JHR_{123}\cos\phi + JH^2A_{24}\sin3\theta\sin2\phi; \quad (6.4c)$$

θ is chosen as 15° to give comparable contributions to E_J and $E_{Z\times J}$ from A_{24}. Seven coefficients are involved: ρ_{11}, R_{231}, R_{123}, A_{12}, A_{13}, A_{24}, A_{42}. Two more - A_{44}, A_{11} - appear if η is made equal to $\theta + 90^\circ$ so that $\underline{J}$ is in the H-plane:

$$E_J = \rho_{11}J + JH^2(A_{11}\sin^2\phi + A_{13}\cos^2\phi + A_{24}\sin3\theta\sin2\phi) \quad (6.5a)$$

$$E_Z = JH^2(-A_{42}\sin3\theta\sin^2\phi - A_{44}\sin2\phi); \quad (6.5b)$$

$$E_{Z\times J} = -JHR_{123}\cos\phi + JH^2A_{24}\cos3\theta\sin2\phi; \quad (6.5c)$$

J‖Z (figure 6.1B)

The remaining three coefficients, ρ_{33}, A_{31} and A_{33} are involved in the second configuration, J‖Z. Again, three fields may be measured:-

$$E_J = \rho_{33}J+JH^2(A_{31}\sin^2\phi+A_{33}\cos^2\phi); \quad (6.6a)$$

$$E_X = -JHR_{231}\cos\eta\sin\phi+JH^2(A_{42}\sin 2\eta\sin^2\phi - A_{44}\sin\eta\sin 2\phi); \quad (6.6b)$$

$$E_Y = -JHR_{231}\sin\eta\sin\phi+JH^2(A_{42}\cos 2\eta\sin^2\phi + A_{44}\cos\eta\sin 2\phi); \quad (6.6c)$$

Conveniently, η may be set at 0° or 90°. Changing the choice of binary axis corresponds to the transformation $\theta \rightarrow \theta + 180^\circ$ in equations 6.4, 6.5, 6.6. Consistently, A_{24} and A_{42} change sign. No distinction is necessary, at this stage, as to which binary axis is involved.

It is possible to measure all twelve coefficients on just two samples. If all the equations are utilised, a large amount of cross-checking occurs. For practical convenience, three samples were used in this work: some coefficients were measured in two ways on the same sample and most were remeasured on different samples. All coefficients have been measured at six temperatures between $77^\circ K$ and $305^\circ K$.

Sample 1.

Three probes were attached to a sample cut in the $J \perp Z$ configuration, to pick up E_J and E_{ZXJ}. From equation (6.4a) the following coefficients were measured:-

ρ_{11} : $E_J = \rho_{11} J$ for $H = 0$

A_{13} : $E_J = \rho_{11} J + JH^2 A_{13}$ for $\phi = 0^o$, 180^o.

A_{12} : $E_J = \rho_{11} J + JH^2 A_{12}$ for $\phi = 90^o$, 270^o.

A_{24} and $(A_{12} + A_{13})$:

$$E_J = \rho_{11} J + JH^2 \{ (A_{13}+A_{12})/2 - A_{24} \cos 3\theta \}$$

for $\phi = 45^o$, 225^o.

$$E_J = \rho_{11} J + JH^2 \{ (A_{13}+A_{12})/2 + A_{24} \cos 3\theta \}$$

for $\phi = 135^o$, 315^o.

A_{24} results from the difference average of these two equations. The sum average provides $(A_{12}+A_{13})$. Equation (6.4c) provided R_{123}.

R_{123} : $E_{ZXJ} = \pm JHR_{123}$ for $\phi = 0^o$, 180^o.

A graphical plot, at room temperature, of equation (6.4c) is presented in figure 6.2. Practically, only $(JHR_{123} \cos\phi)$ appears; $(JH^2 A_{24} \sin 3\theta \sin 2\phi)$ contributes a maximum (when $\phi \to 90^o$) of 2% of V_{ZXJ}

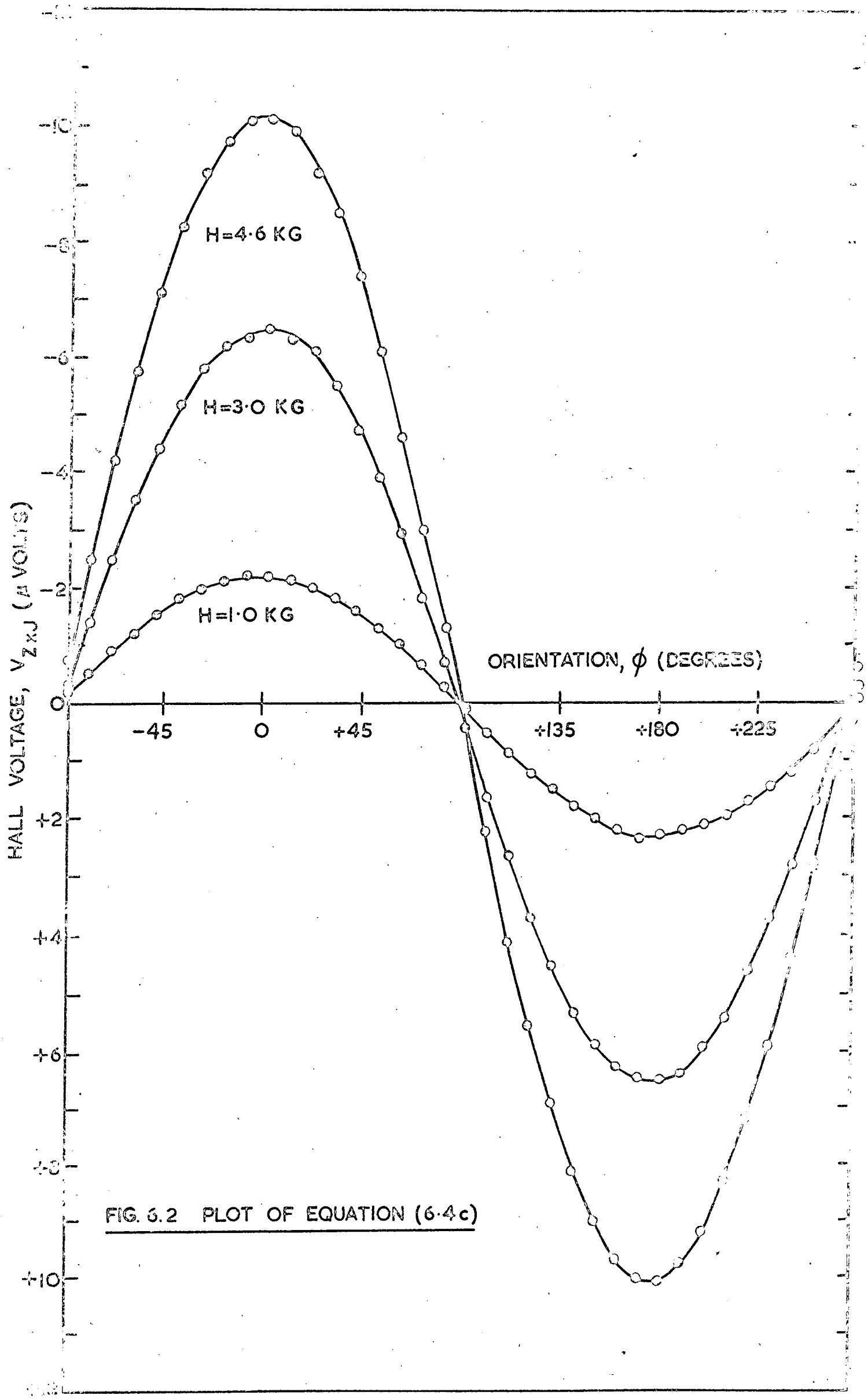

FIG. 6.2 PLOT OF EQUATION (6·4c)

for H = 4.6KG and only 0.4% for H = 1.0 KG.

Sample 2.

A second sample, cut in the J Z configuration had probes to measure E_J, E_Z. This time, equations (6.5) apply.

ρ_{11} : $E_J = \rho_{11} J$ for H = 0

A_{13} : $E_J = \rho_{11}J+JH^2A_{13}$ for $\phi = 0^o$, 180^o

A_{11} : $E_J = \rho_{11}J+JH^2A_{11}$ for $\phi = 90^o$, 270^o

A_{24} and $(A_{11}+A_{13})$:

$$E_J = \rho_{11}J+JH^2\{(A_{11}+A_{13})/2+A_{24}\sin 3\theta\}$$

for $\phi = 45^o$, 225^o

$$E_J = \rho_{11}J+JH^2\{(A_{11}+A_{13})/2-A_{24}\sin 3\theta\}$$

for $\phi = 135^o$, 315^o

As before, the difference average yields A_{24} and the sum average $(A_{11}+A_{13})$.

A_{42} and A_{44} are both small coefficients. Equations (6.5b) which contains these coefficients is most useful; all the other equations involving A_{42} are dominated by much larger coefficients R_{123} and R_{231}.

A_{42} : $E_Z = JH^2(-A_{42}\sin 3\theta)$ for $\phi = 90^\circ, 270^\circ$

A_{44} and A_{42}:

$$E_Z = JH^2\left(-\frac{A_{42}\sin 3\theta}{2} - A_{44}\right) \text{ for } \phi = 45^\circ, 225^\circ$$

$$E_Z = JH^2\left(-\frac{A_{42}\sin 3\theta}{2} + A_{44}\right) \text{ for } \phi = 135^\circ, 315^\circ$$

The difference average yields A_{44} and the sum average A_{42}.

R_{231} was obtained using (6.4b).

R_{231} : $E_Z = JHR_{231} + JH^2 A_{42}\sin 3\theta$ for $\phi = 90^\circ$.

$E_Z = -JHR_{231} + JH^2 A_{42}\sin 3\theta$ for $\phi = 270^\circ$

R_{231} results from the difference average.

Sample 3.

The remaining coefficients were measured from the configuration $\underline{J} \| Z$, through equations (6.6).

A_{33} : $E_J = \rho_{33} J + JH^2 A_{33}$ for $\phi = 0^\circ, 180^\circ$

A_{31} : $E_J = \rho_{33} J + JH^2 A_{31}$ for $\phi = 90^\circ, 270^\circ$.

R_{231} : $E_X = \pm JHR_{231}$ for $\eta = 0^\circ$, $\phi = 90^\circ, 270^\circ$.

VI.2. Details of Calculations.

All coefficients result from averages of the angles ϕ, $\phi + 180^{\circ}$ which is equivalent, assuming a well constructed magnet, to +H and -H. This is important: error voltages due to inexact probe positioning are removed. The probes measuring E_J, for example, will pick up a small fraction of E_Z (or E_{ZXJ}) unless they are exactly sited on the centre line of the sample. Averaging for +H and -H separates the odd (Hall) and even (magnetoresistance) effects. See figure 6.3.

Figure 6.4 shows graphical plots that determine typical coefficients $-R_{123}$, R_{231}, A_{12}, A_{13} - at the temperature $250^{\circ}K$. The graphs demonstrate two important points : (a) the straight line plot shows that the low field condition $\mu H << 1$ is not violated up to 5 kilogauss, and (b) drift is within the desired limit of 15 nV. Accurate values of all the magnetoresistivity coefficients were obtained from a least-mean-squares fit to the measurements by a computer. The PL1 computer programme is shown in figure 6.5: straight-line gradient

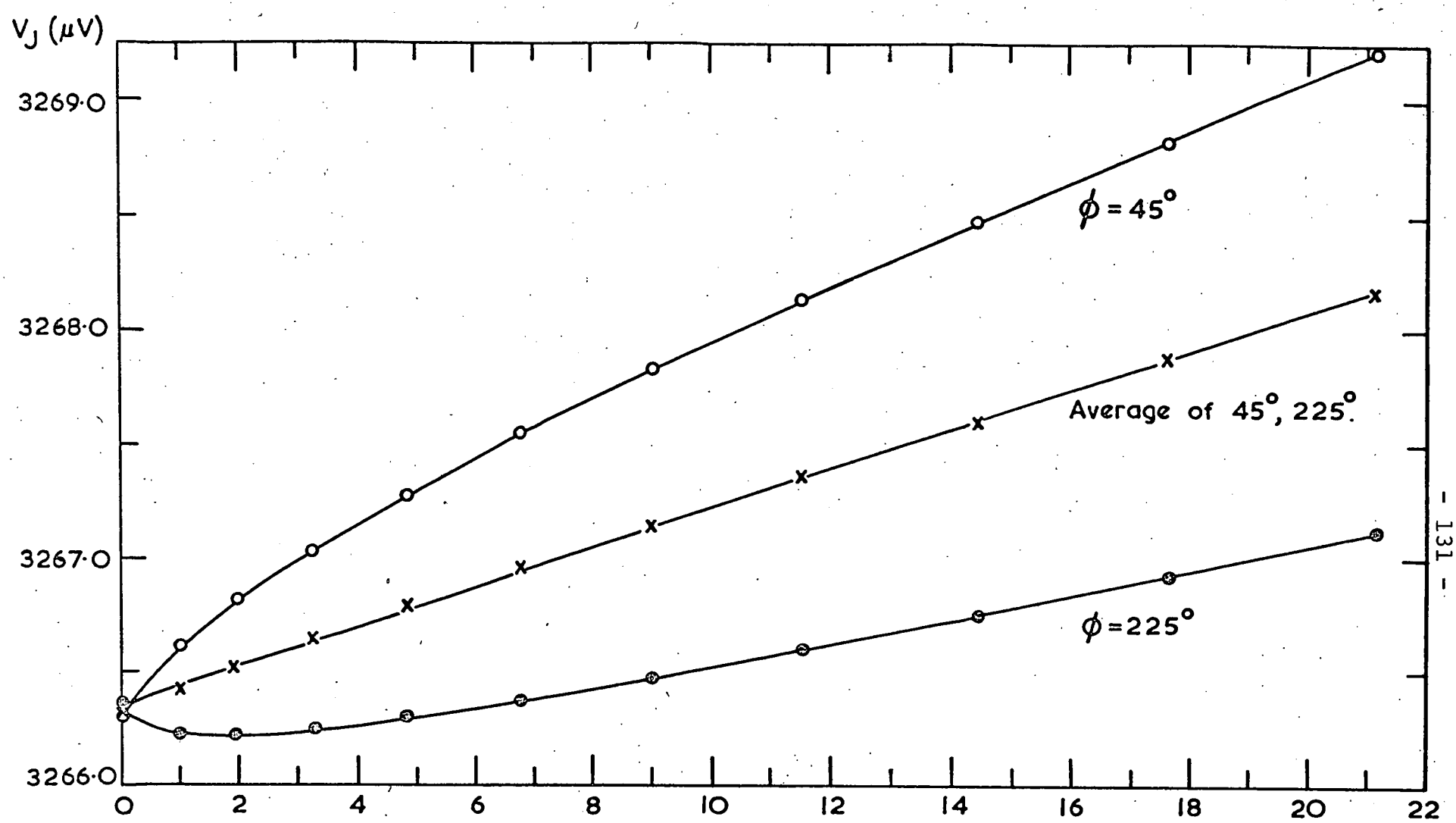

Figure 6·3 Data from table 5·1. Error Hall Voltage cancels to give $V_J \propto H^2$.

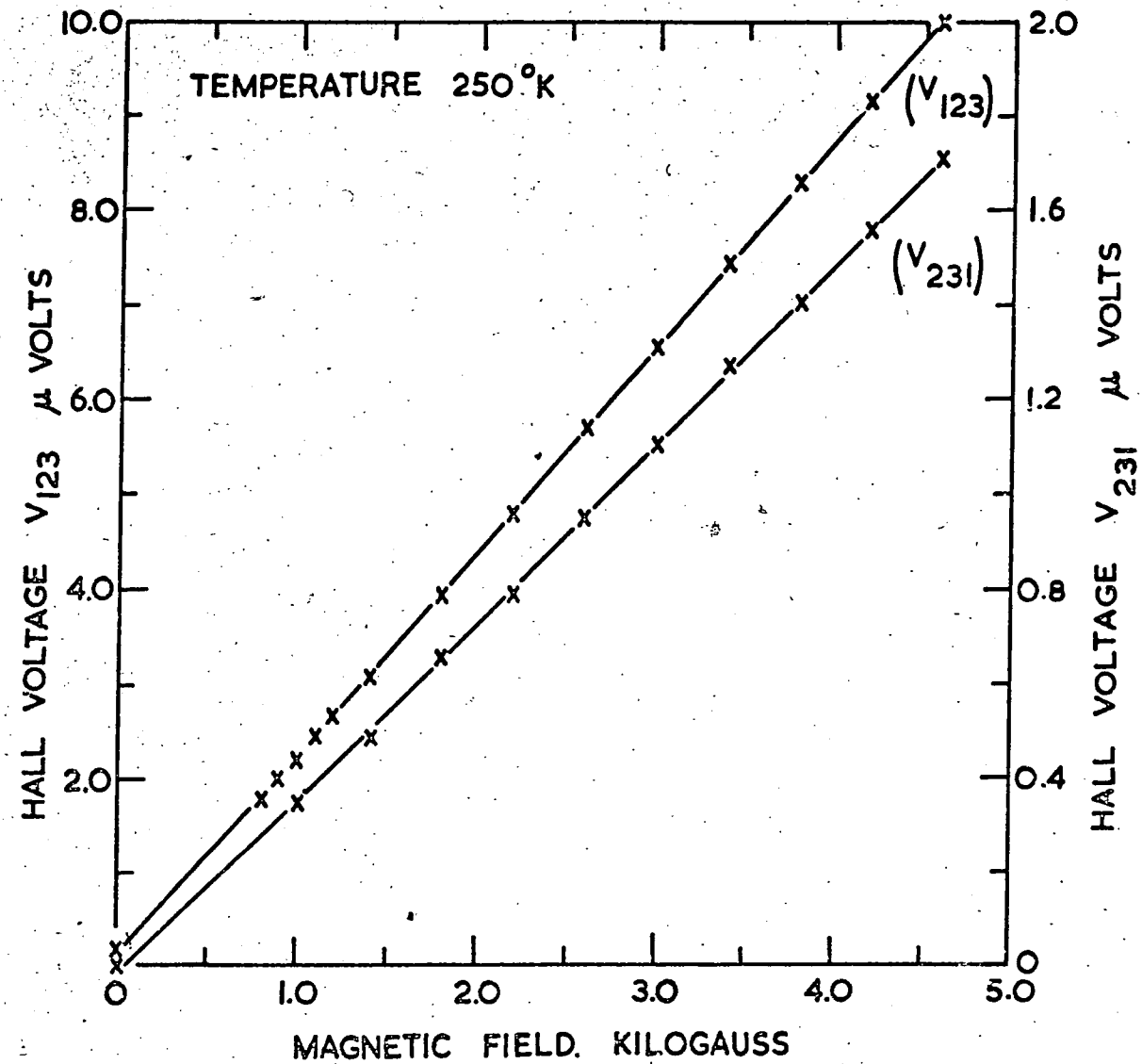

THE MAGNETIC FIELD DEPENDENCE OF V_{123} AND V_{231}. V_{123} AND V_{231} ARE DIRECTLY PROPORTIONAL TO R_{123} AND R_{231}.

Figure 6.4 a.

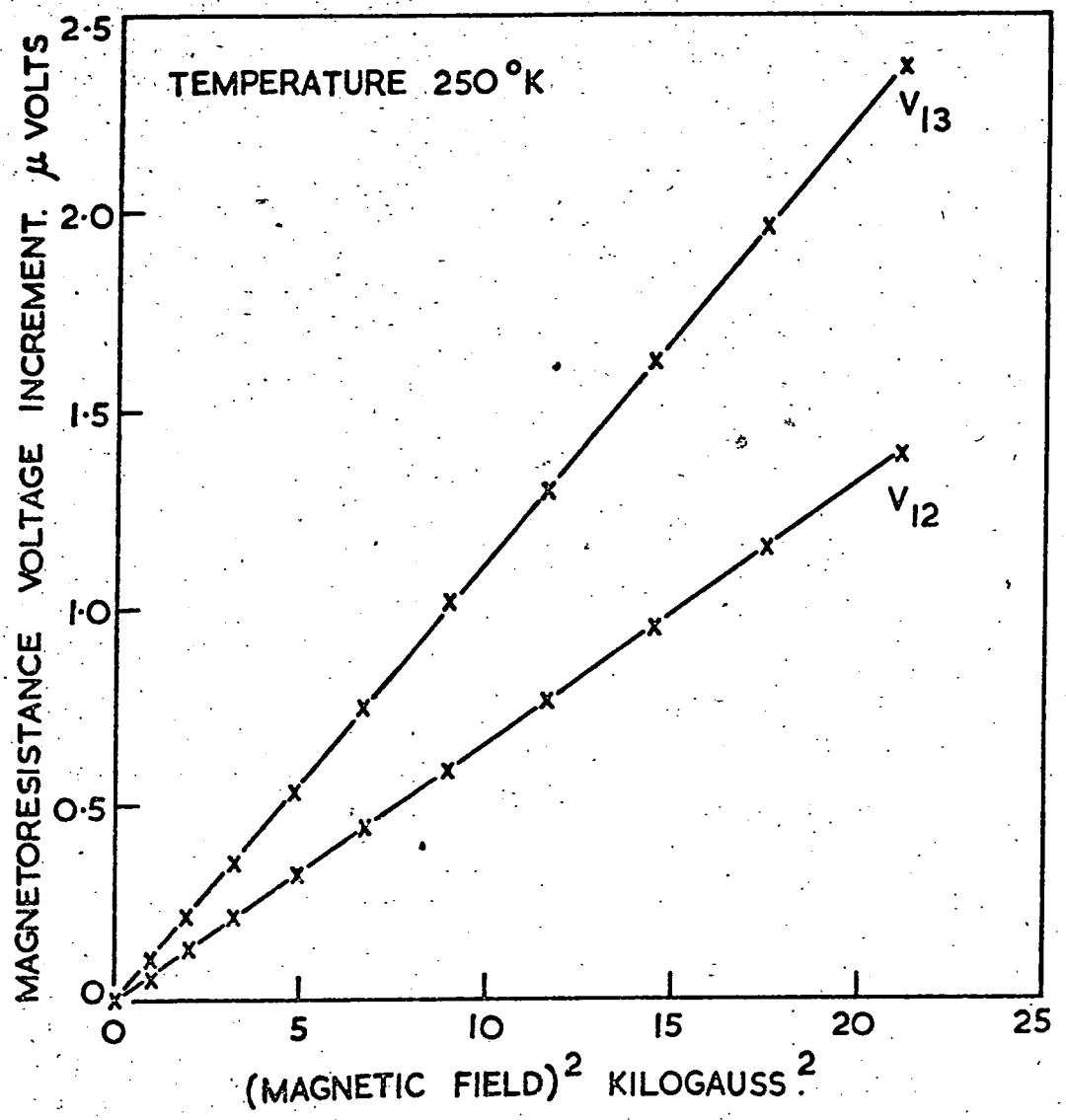

THE MAGNETIC FIELD DEPENDENCE OF V_{13} AND V_{12}. V_{13} AND V_{12} ARE DIRECTLY PROPORTIONAL TO A_{13} AND A_{12}.

Figure 6.4 b.

```
 1   MNSQS:PROC OPTIONS(MAIN);
 2   DCL((GRAD,INCPT,N)FLOAT,(I)FIXED BIN);
 3   GET LIST(N,P,Q);
 4   BEGIN;
 5   DCL((X_X,X,Y,Z)(N),A(N,2),COR(2))FLOAT;
 6   GET LIST(X_X,X);  I=0;
 7   AGAIN:GET LIST(A,COR);
 8   DO K=1,2;
 9   DO L=1 TO N;
10   A(L,K)=A(L,K)-(L-1)*COR(K)/(N-1);
11   END; END;
12   Y=(A(*,1)+A(*,2))*0.5;
13   PUT SKIP(2) LIST(Y);
14   MEANY=SUM(Y)/N;
15   GRAD=SUM(X_X*(Y-MEANY))/P;
16   INCPT=MEANY-GRAD*Q;
17   Z=Y-(INCPT+GRAD*X);
18   STDER=SQRT(SUM(Z*Z)/((N-2)*P));
19   I=I+1;
20   PUT SKIP(2) LIST(GRAD,INCPT,Z,STDER); GO TO AGAIN; END; END;
```

Figure 6.5

Computer programme for calculating

the twelve coefficients

and intercept are calculated by the standard formulae (see Topping 1962); statement numbers 7 - 11 correct the initial readings for the thermo-magnetic drift mentioned on page 119.
Table 6.1 shows typical results; the scatter of points is pleasingly small.

VI.3. Experimental Results.

Table 6.2 gives all the measurements of the coefficients. Generally, the cross-check agreement is good. The values at six temperatures averaged over the three samples are presented in table 6.3; they result from approximately 2,500 readings.

The signs of the coefficients are established unequivocally in all but two cases by relating the current and field directions. The seven coefficients ρ_{11}, ρ_{33}, A_{11}, A_{12}, A_{13}, A_{31} and A_{33} are all positive and R_{123}, R_{231} and A_{44} are negative, as equations (4.26) predict; A_{24} and A_{42} are both positive or both negative. To establish completely the signs of A_{24} and A_{42}, X-ray photographs must be taken to find the directions of pseudo-symmetry in the sample and

Data for A_{12} at 250°K.

Gradient : 0.066 $\mu V/KG^{-2}$

Scatter of points ($10^{-9}V$):

-1.1; -5.8; +5.0; -0.4; +1.2; -0.4;
-5.0; +9.3; +1.5; +1.6; -5.4.

Standard error : 0.21 x $10^{-9}V$.

Data for A_{13} at 250°K.

Gradient : 0.112 $\mu V/KG^{-2}$.

Scatter of points ($10^{-9}V$):

-2.5; -3.1; +0.3; -2.1; -3.4; +2.4;
+6.3; +7.4; +9.6; -11.0; -3.5.

Standard error : 0.28 x $10^{-9}V$.

Table 6.1.

Numerical form of figure 6.4 for A_{12} and A_{13}, produced by the computer programme shown in figure 6.5.

Temp.	Resistivity		Hall		Magnetoresistivity									
^{o}K	ρ_{11}	ρ_{33}	$-R_{231}$	$-R_{123}$	A_{13}	A_{31}	$-A_{44}$	A_{11}	A_{12}	A_{33}	$-A_{24}$	$-A_{42}$	$A_{12}+A_{13}$	$A_{11}+A_{13}$
305	26.7 26.9	34.1	2.05 2.11	11.5	9.74 9.70	8.2	1.9	2.5	5.5	5.8	1.63 2.02	0.95 1.1	15.3	12.1
250	20.8 21.2	26.2	2.27 2.44	12.5	13.7 14.0	11.3	2.6	3.5	8.1	7.8	2.4 2.0	1.32 1.38	22.0	17.5
215	16.7 16.9	20.5	2.49 2.62	13.1	18.2 18.5	13.7	3.2	4.8	11.0	9.2	2.87 2.59	1.59 1.66	29.2	23.3
175	12.9 13.0	15.2	2.56 2.75	13.7	24.9 25.2	18.8	4.5	6.73 6.68	15.0	12.7	4.11 4.07	2.14 2.22	40.9	30.9
125	7.9 8.0	9.2	2.51 2.75	14.4	41.5 41.8	31	7.7	11.8	27	20.0	6.38 5.86	3.91 3.92	69.5	54.0
77	3.61 3.66	3.95	1.76 2.01	14.7	80.7 81.8	66	17.4	25.9	63	40	11.5 11.6	7.9 8.3	145	112

Units: Resistivity, 10^{-6} ohm cm; Hall, 10^{-8} ohm cm.Kgauss^{-1};
magnetoresistivity, 10^{-10} ohm cm. Kgauss^{-2}.

Table 6.2

The measured values of the twelve magnetoresistivity coefficients.

Temp.	Resistivity		Hall		Magnetoresistivity							
^{o}K	ρ_{11}	ρ_{33}	$-R_{231}$	$-R_{123}$	A_{13}	A_{31}	$-A_{44}$	A_{11}	A_{12}	A_{33}	$-A_{24}$	$-A_{42}$
305	26.8	34.1	2.08	11.5	9.7	8.2	1.9	2.5	5.5	5.8	1.8	1.0
250	21.0	26.2	2.35	12.5	13.8	11.3	2.6	3.5	8.1	7.8	2.2	1.3
215	16.8	20.5	2.55	13.1	18.4	13.7	3.2	4.8	11.0	9.2	2.8	1.6
175	12.9	15.2	2.66	13.7	25.0	18.8	4.5	6.7	15.0	12.7	4.1	2.2
125	8.0	9.2	2.63	14.4	42	31	7.4	11.8	27	20.0	6.0	3.9
77	3.63	3.95	1.88	14.7	81	66	17	26	63	40	11.5	8.1
Approx. Error %	3	3	5	5	5	5	15	5	5	5	15	15

Units : Resistivity, 10^{-6} ohm cm.; Hall, 10^{-8} ohm cm. Kgauss^{-1};
Magnetoresistivity, 10^{-10} ohm cm. Kgauss^{-2}.

Table 6.3.

The Averaged measured values of the twelve magneto-resistivity coefficients.

so determine the choice of binary axes (page 13). For the co-ordinate system defined in section II.1è, A_{24} and A_{42} are negative. In figure 6.6 the magnetoresistivity coefficients are plotted against temperature logarithmically. In general, straight lines are displayed, indicating consistent experimental work. Line gradients, or temperature exponents are similar for all A_{ij}; see table 6.4. ρ_{33}, ρ_{11} and $-R_{231}$ all depart from the straight line relationship at 77°K. This was not observed for antimony by Oktu and Saunders (1967), but recently (Tanaka et al. 1968) measurements have been made of the twelve magnetoresistivity coefficients of antimony down to 55°K when a similar behaviour of ρ_{33}, ρ_{11} and $-R_{231}$ is observed. Further discussion of this point follows later (page 195).

The only other coefficient values available for comparison with this work are those of ρ_{11} and ρ_{33} at 293°K (Taylor et al. 1965). Agreement is close for ρ_{11}; the values of ρ_{33} differ by about 10% (table 6.5).

Table 6.6 lists the magnetoconductivity coefficients, calculated from table 6.3 by means

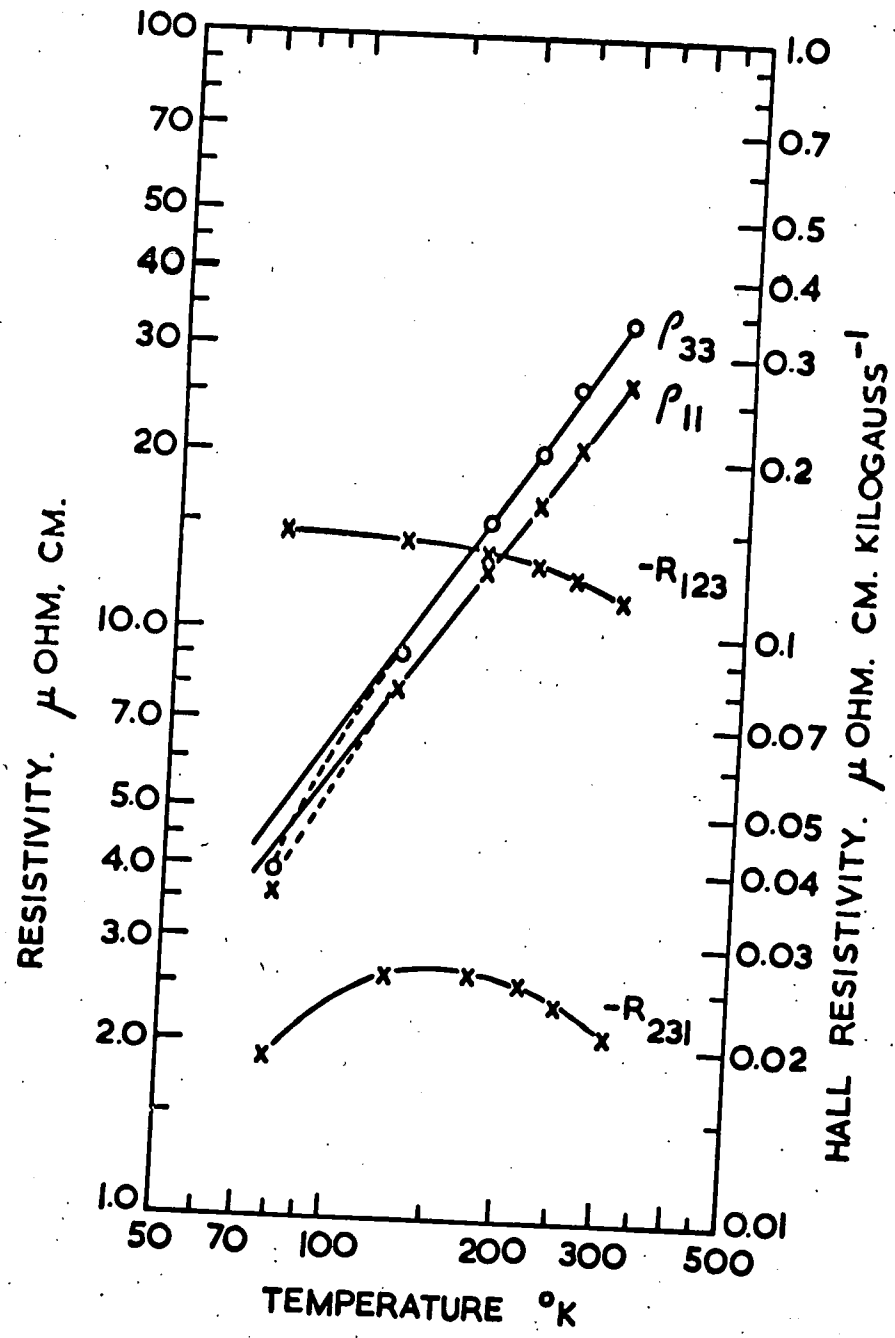

Figure 6.6. a.

The temperature dependence of the magnetoresistivity coefficients.

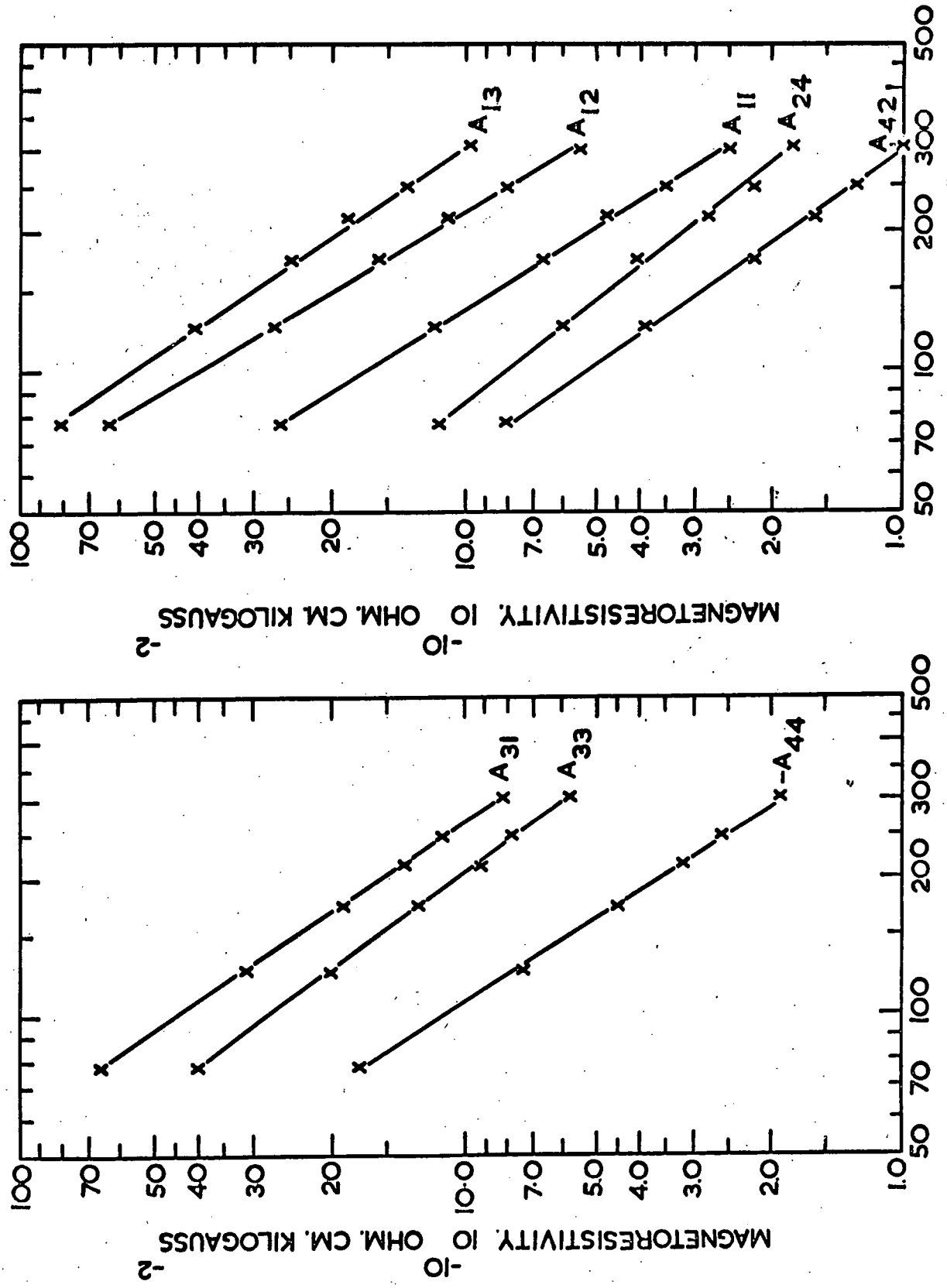
THE TEMPERATURE DEPENDENCE OF THE MAGNETORESISTIVITY TENSOR COEFFICIENTS.
MAGNETORESISTIVITY 10⁻² OHM. CM. KILOGAUSS
100
70
50
40
30
20
10.0
7.0
5.0
4.0
3.0
2.0
1.0
A13
A12
A11
A24
A42
A31
A33
A44
50 70 100 200 300 500
TEMPERATURE °K

Figure 6.6b.

Coefficient	Temperature Exponent	Approximate Error
ρ_{11}	+1.3	± 0.05
ρ_{33}	+1.4	
A_{13}	-1.6	± 0.2
A_{31}	-1.5	
$-A_{44}$	-1.6	
A_{11}	-1.7	
A_{12}	-1.8	
A_{33}	-1.4	
$-A_{24}$	-1.4	
$-A_{42}$	-1.5	

Table 6.4.

The temperature exponents of the magnetoresistivity coefficients

	$\mu\Omega$. cm.	
	ρ_{11}	ρ_{33}
This work	25.2 (3%)	32.1 (3%)
Taylor et al. (1965)	25.5 ($\pm$0.5)	35.6 ($\pm$ 1.9)

Table 6.5.

A comparison of measurements of ρ_{11} and ρ_{33} at 293^{o}K.

of the transform formulae (4. 5). Errors are slightly greater since each magnetoconductivity coefficient, with the exception of σ_{11} and σ_{33}, is compounded from two or more magnetoresistivity coefficients. Graphs (figure 6.7) against log T of log σ_{ij} give slopes of -1.4, of log P_{ijk} give -3.0 and of log B_{ij} give -4.3 (table 6.7). This is a reflection of a carrier mobility-temperature dependence close to $T^{-1.5}$, since basically, equations (4.26) state:-

$$\sigma_{ij} = f(\mu,\nu)$$

$$P_{ijk} = f(\mu^2,\nu^2)$$

$$B_{ij} = f(\mu^3,\nu^3)$$

This point is amplified later (page195). The deviation at $77^{o}K$ of all B_{ij} from a straight-line relationship reflects the already mentioned behaviour of ρ_{ij}.

VI.4. An Assessment of the Two Identities Imposed by the Ellipsoidal Band Model.

In chapter IV, two identities between the magnetoconductivity coefficients are given:

Temp	Conductivity		Inverse Hall		Magnetoconductivity							
^{o}K	σ_{11}	σ_{33}	$-P_{231}$	$-P_{123}$	B_{13}	B_{31}	$-B_{44}$	B_{11}	B_{12}	B_{33}	$-B_{24}$	$-B_{42}$
305	3.73	2.93	2.3	16.0	2.0	0.72	0.24	0.35	0.78	0.50	0.25	0.10
250	4.76	3.82	4.3	28.	4.8	1.68	0.60	0.79	1.88	1.14	0.50	0.23
215	5.92	4.88	7.4	46	10.0	3.3	1.20	1.69	4.0	2.18	0.96	0.47
175	7.75	6.58	13.6	82	24	8.4	2.8	4.00	9.7	5.5	2.5	1.04
125	12.3	10.9	35	220	102	38	13.1	17.9	43	23.9	9.0	5.2
77	27.5	25.3	131	1120	1070	430	150	197	470	256	87	56
Approx Error %	3	3	10	10	10	10	20	10	10	10	20	20

Units : Conductivity, 10^{4} ohm^{-1} $cm.^{-1}$; Inverse Hall, 10 $ohm^{-1}cm.^{-1}Kgauss^{-1}$;
Magnetoconductivity, $ohm^{-1}cm.^{-1}Kgauss^{-2}$.

Table 6.6

The measured values of the twelve magneto-conductivity coefficients.

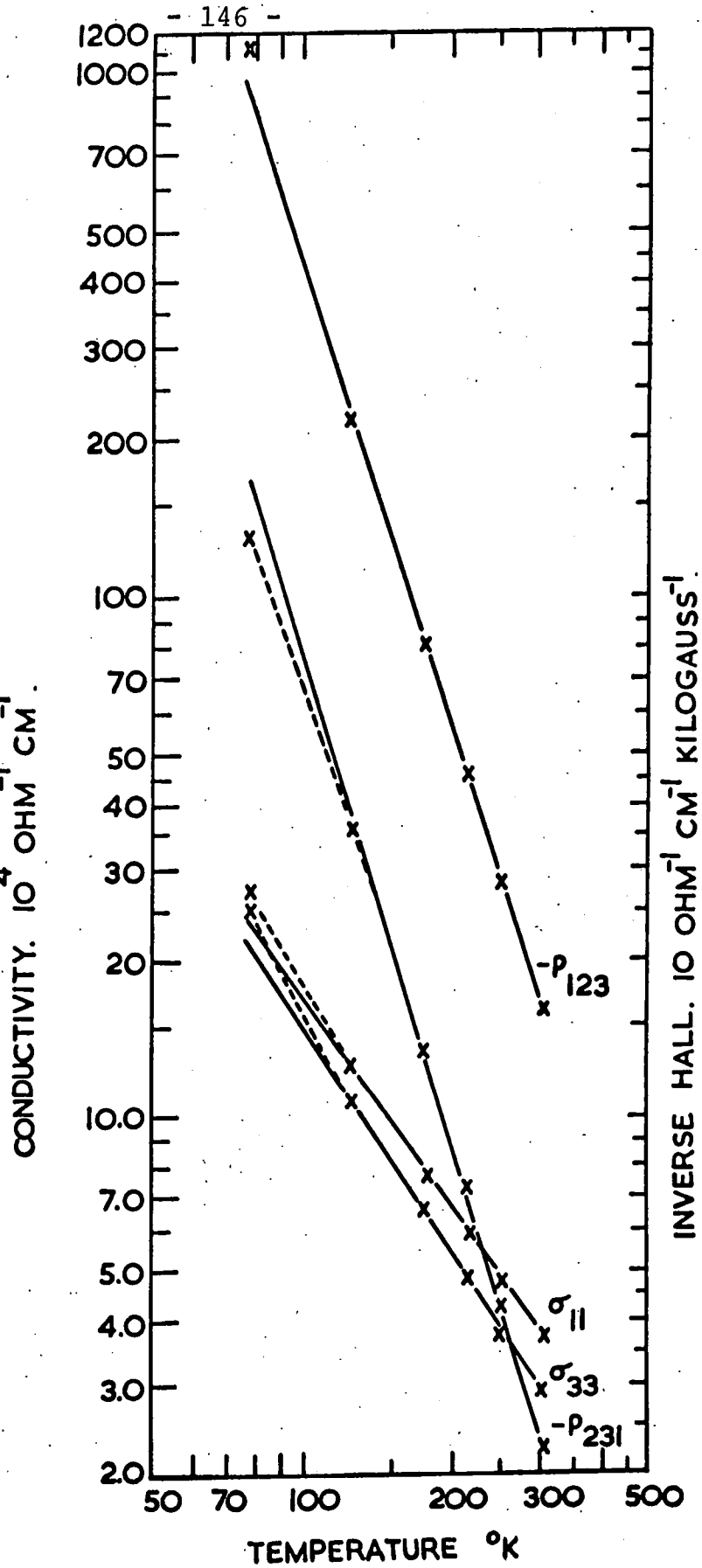

Figure 6.7a.

The temperature dependence of the magneto-conductivity coefficients

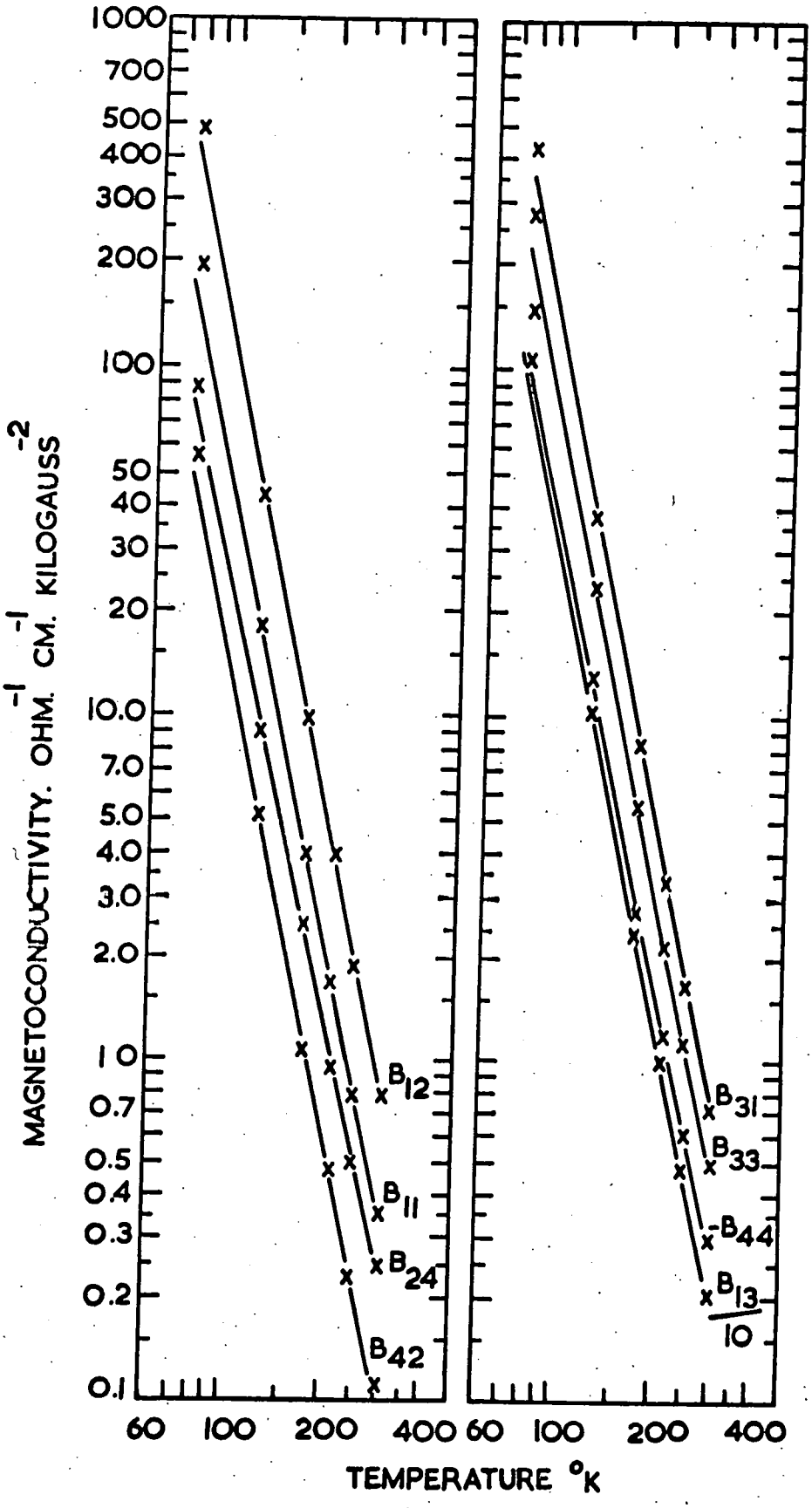
MAGNETOCONDUCTIVITY. OHM.$^{-1}$ CM.$^{-1}$ KILOGAUSS^{-2}
1000
700
500
400
300
200
100
50
40
30
20
10.0
7.0
5.0
4.0
3.0
2.0
1.0
0.7
0.5
0.4
0.3
0.2
0.1
B_{12}
B_{11}
B_{24}
B_{42}
B_{31}
B_{33}
B_{44}
B_{13}/10
60
100
200
400
TEMPERATURE °K

Figure 6.7b.

Coefficient	Temperature Exponent	Approximate Error
σ_{11}	-1.35	± 0.05
σ_{33}	-1.45	
$-P_{231}$	-3.1	± 0.1
$-P_{123}$	-2.9	
B_{13}	-4.3	± 0.2
B_{31}	-4.5	
$-B_{44}$	-4.3	
B_{11}	-4.4	
B_{12}	-4.4	
B_{33}	-4.3	
$-B_{24}$	-4.2	
$-B_{42}$	-4.4	

Table 6.7.

The temperature exponent of

the magnetoconductivity coefficients.

$$2B_{33} \equiv 3B_{11} - B_{12} - 2B_{44}.$$

and

$$4P_{231}(-2B_{44}\,\sigma_{11}/\sigma_{33} - B_{13})$$

$$\equiv P_{123}(4B_{31}\,\sigma_{11}/\sigma_{33} - 3B_{12} + B_{11} + 2B_{44}).$$

The left and right hand sides of these identities have been calculated and are presented in tables 6.8 and 6.9. Corresponding figures for antimony (Oktu 1967) are also given. Just as for antimony, the first identity 'looks' reasonable, but the second identity has almost equal and opposite left and right hand sides. Oktu (1967) has mentioned that the number of terms involved in, and the complexity of, these identities means that they can be satisfied by varying some of the coefficients within the experimental error. The same reasoning will apply here to arsenic.

The fact that the same discrepancy has been revealed by three independent measurements on antimony (Freedman and Juretschke 1961, Epstein and Juretschke 1963, Oktu and Saunders 1967) and now for arsenic, suggests that a systematic experimental error is extremely unlikely; the discrepancy must reflect the assumptions made in

ARSENIC

Temp (^{o}K)	$2B_{33}$	=	$3B_{11}-B_{12}-B_{44}$
305	1.00		0.58
250	2.29		1.68
215	4.37		3.54
175	11.0		6.9
125	47.9		37.1
77	511		399

ANTIMONY

273	0.44		0.53
225	1.08		1.09
183	2.76		3.63
139	9.4		15.4
77	119.8		152.8

Table 6.8

An assessment of the identity

$2B_{33}=3B_{11}-B_{12}-2B_{44}$ for arsenic

and antimony.

ARSENIC

Temp (^{o}K)	$^{4P}_{231}(-2B_{44}\sigma_{11}/\sigma_{33}-B_{13}) = P_{123}(4B_{31}\sigma_{11}/\sigma_{33} -3B_{12}+B_{11}+2B_{44})$	
305	$-0.96.10^{2}$	$+1.18.10^{2}$
250	$-5.7.10^{2}$	$+6.7.10^{2}$
215	$-20.7.10^{2}$	$+16.6.10^{2}$
175	-99.10^{2}	$+80 . 10^{2}$
125	$-1.02.10^{5}$	$+0.79.10^{5}$
77	$-3.92.10^{5}$	$+3.56.10^{5}$

ANTIMONY

273	$-1.00.10^{3}$	$+0.97.10^{3}$
225	$-5.50.10^{3}$	$+2.40.10^{3}$
183	$-27.7.10^{3}$	$+14.9.10^{3}$
139	$-17.7.10^{4}$	$+12.7.10^{4}$
77	$-12.5.10^{6}$	$+8.6.10^{6}$

Table 6.9

An assessment of the identity

$^{4P}_{231}(-2B_{44}\sigma_{11}/\sigma_{33}-B_{13}) = P_{123}(4B_{31}\sigma_{11}/\sigma_{33}-3B_{12}+B_{11}+2B_{44})$.

for arsenic and antimony.

deriving equations(4.26). However, since both identities are satisfied within experimental error, the equations may be assumed to result from an adequate approximation to the actual band structure.

CHAPTER VII

THE COMPUTATION OF THE BAND PARAMETERS AND CARRIER MOBILITIES

The remaining task is to solve equations (4.26) using the set of twelve magnetoconductivity coefficients given in table 6.6. The resulting band and mobility data may then be compared to other experimental work (chapter VIII).

VII.1. Previous Methods of Computation

a. Direct solution.

Although theoretically possible, a direct solution by eliminating unknowns is not practicable. The transposed equations from (4.26) involve complex third-order terms of the twelve coefficients. Experimental error in measuring the coefficients is magnified enormously to yield meaningless answers: e.g. negative mobilities. It has already been mentioned (page 149) that the identities between the coefficients, which at first sight seem quite incorrect, may be satisfied by varying the coefficients within the limits of experimental error. Further, because the ellipsoidal model approximates to the truth, any

solution of the nine parameters cannot fit all twelve equations exactly; no unique solution can exist.

b. Freedman and Juretschke's technique

The practical solution is that which provides the closest approximation to all twelve equations. One way of establishing this approximation is to feed values for the nine unknowns into equations (4.26), calculate the coefficients and then compare these values with the experimentally measured ones. The problem is then to decide what values to choose for the nine unknowns, or more simply, what is the solution to the equations ? We have come full circle. But at least we have a process for proving the solution, once we have it. This suggests some kind of trial and error procedure; the most basic would be a systematic selection of values for each variable and a calculation of the coefficients for every choice. Once again we have an impractical problem. If ten values are taken for each of the nine variables then equations (4.26) must be evaluated 10^9 times: a colossal task, even for the biggest computer.

Freedman and Juretschke (1961) combined the ideas of a direct solution and a trial and error procedure to avoid the practical drawbacks of both methods. They rewrote equations (4.26) into a set of eight equations in ten unknowns. Two unknowns were chosen and the remaining

eight calculated by direct solution from the eight equations. This provided a set of parameters to feed directly into equations (4.26) to calculate the twelve coefficients. The two chosen unknowns were swept over a range of values until a best fit between calculated and measured coefficients was obtained. The eight equations are derived as follows:-

Define

$$\mu_x=\mu_1+C_e^2\mu_2+S_e^2\mu_3;\quad \nu_x=\nu_1+C_h^2\nu_2+S_h^2\nu_3.$$

$$\mu_z=S_e^2\mu_2+C_e^2\mu_3;\quad \nu_z=S_h^2\nu_2+C_h^2\nu_3.$$

$$\mu_{xx}=\mu_2\mu_3+\mu_1(S_e^2\mu_2+C_e^2\mu_3);\quad \nu_{xx}=\nu_2\nu_3+\nu_1(S_h^2\nu_2+C_h^2\nu_3). \tag{7.1}$$

$$\mu_{zz}=\mu_1(C_e^2\mu_2+S_e^2\mu_3);\quad \nu_{zz}=\nu_1(C_h^2\nu_2+S_h^2\nu_3).$$

Seven equations follow by direct substitution into (4.26) the eighth is a compound of B_{12}, B_{11} and B_{44} :

$$\sigma_{11} = Ne(\mu_x + \nu_x)/2$$

$$\sigma_{33} = Ne(\mu_z + \nu_z)/2$$

$$-P_{231} = Ne(\nu_{xx} - \mu_{xx})/2c$$

$$-P_{123} = Ne(\nu_{zz} - \mu_{zz})/c$$

$$B_{13} = Ne(\mu_x\mu_{zz} + \nu_x\nu_{zz})2c^2 \qquad (7.2)$$

$$B_{31} = Ne(\mu_z\mu_{xx} + \nu_z\nu_{xx})/2c^2$$

$$-B_{44} = Ne(\mu_z\mu_{zz} + \nu_z\nu_{zz})/2c^2$$

$$3B_{12}-B_{11}-2B_{44} = Ne(\mu_x\mu_{xx} + \nu_x\nu_{xx})/2c^2$$

The symmetry of equations (4.26) is clearly illustrated here. Freedman and Juretschke defined S and f as the two variables to be swept :

$$\mu_1 + \mu_2 + \mu_3 = fS;\ \nu_1 + \nu_2 + \nu_3 = (1-f)S;$$

$$S = (2\sigma_{11} + \sigma_{33})/eN.$$

Choosing S corresponds to choosing N. f is a measure of the contribution of the electrons to the coefficients.

Equations (7.2) were then rewritten to involve f, S and dimensionless variables. A full description of this method of solution may be found in a thesis by Oktu (1967).

VII.2. The Least-Mean-Squares Solution

a. Basic Method.

Freedman and Juretschke's method still has a disadvantage: because a direct solution is used in part, it is inherently biassed in favour of fitting certain coefficients. Only by human intervention with trial and error can the solution be improved. This requires time, trouble and a certain amount of inspired guesswork. And even then the possibility remains that a better solution exists, but has not been found.

A fresh approach has been made. The principle of a direct solution was abandoned. Instead a way has been devised of scanning all nine variables independently: after each evaluation of the equations the fit between calculated and measured coefficients is assessed by a least-mean-squares criterion. This provides a 'feedback' control for the values over which the variables must be swept. The result is steady progress towards the best approximation that can be made by the least-mean-squares condition.

Consider the overdetermined case of three equations in two unknowns:

$$A = f_1(x,y);\ B = f_2(x,y);\ C = f_3(x,y).$$

Define $M = (f_1-A)^2 + (f_2-B)^2 + (f_3-C)^2$.

If all three equations are exact, x and y exist such that

$$f_1 - A = f_2 - B = f_2 - C = 0.$$

and therefore M = 0. If the equations are approximate, then the best values of x and y may be found by minimising M. Figure 7.1 illustrates how this may be accomplished (see Hawgood 1965). The contours are of different values of M and represent a 'pit'. The bottom of the pit is either at M = 0 so that its co-ordinates are the exact solution of the equations, or at a local minimum in M and its co-ordinates represent the best approximation locally to a solution. Suppose an approximate solution has been found or an arbitrary solution chosen (point Z). Then x is varied, keeping y constant to slide across the cross section PQ until M is minimized. Next this procedure is performed for y, keeping x constant (RS). Repetition produces a path that zigzags in towards the pit bottom. At each stage the lowest point on the cross section may be located by recalculating M as the variable (x or y) is incremented stepwise. Alternatively differentiation could be used. Convergence could be speeded considerably by calculating the gradient vector and proceeding along the path of steepest descent. But this is a complex procedure for the many-dimensional case and was not adopted. Another technique is interpolation to various degrees of accuracy by employing linear, quadratic, or cubic functions (Dickinson 1958).

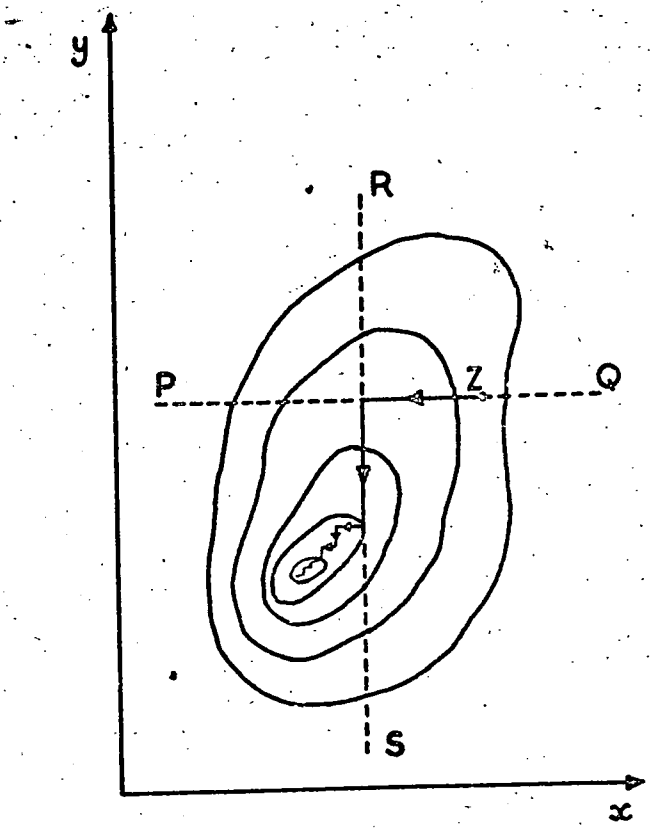

Figure 7.1

The technique used to find a solution to the equations. The contours represent different values of M (after Hawgood 1965).

The extension of the method to the nine dimensions of the equations (4.26) is trivial. Each of the twelve coefficients is calculated by inserting an arbitrary set of parameters into the equations, divided by the corresponding experimental value and then compared to unity to compute a parameter SUMSQ (i.e. M), which is minimised

$$\text{SUMSQ} = \sum_{\sigma,P,B} \left(\frac{\text{calculated coefficient}}{\text{measured coefficient}} - 1.0 \right)^2$$

σ_{ij} and P_{ijk} are weighted because of the smaller experimental error of these coefficients. If SUMSQ could be made equal to zero, then all the calculated coefficients would equal their measured values and a perfect solution would have been found.

b. Computer programme

Figure 7.2 shows the computer programme, written in PL1, devised to perform this searching operation. An analysis of its operation is now given.

Summary of Variables.

Name of Variable	Description
SOLN	9 element array. Stores the values of $\mu_1, \mu_2, \mu_3, C_e, N, \nu_1, \nu_2, \nu_3, C_h$.

```
1   ARSENIC:PROC OPTIONS(MAIN);
2   /* VERSION-NORMALISED AND WEIGHTED COEFFICIENTS. */
3   DCL((SOLN,STEP,MAX,MIN)(9),(EL,HO,COEFF)(12),SMALL,SUMSQ(2))
4   FLOAT,(H,J,I,CYCLE)FIXED BIN);
5   DCL(HOLD(9),Q)FLOAT;
6   ON ENDFILE(SYSIN) STOP;
7   TEMP:GET LIST(MAX,MIN,COEFF,SMALL,J);
8   BEGIN; DCL(CYMAX(J,9)FIXED BIN);
9   GOOD:GET LIST(STEP,SOLN);
10  PUT SKIP LIST(SOLN);
11  I=0; CYCLE=1;
12  KIN=0;
13  HOLD=SOLN;
14  CYMAX=0;
15  CALL EQUATE;
16  PUT SKIP(3) LIST('INITIAL VALUES OF EL,HO,EL+HO,COEFF,RATIO');
17  PUT EDIT(EL,HO,EL+HO,COEFF,(EL+HO)/COEFF)(5(SKIP,2 F(12,3),10 E(9,3)));
18  DO WHILE(CYCLE<=J);
19  DO I=1 TO 9;
20  SUMSQ(1)=Q;
21  IF SUMSQ(1)<SMALL THEN GO TO EXIT;
22  H=1;
23  DO WHILE((SOLN(I)>MIN(I))&(SOLN(I)<MAX(I)));
24          SOLN(I)=SOLN(I)+H*STEP(I);
25  CALL EQUATE;
26  SUMSQ(2)=Q;
27  IF SUMSQ(2)>SUMSQ(1) THEN IF H=1 THEN DO; SOLN(I)=SOLN(I)-STEP(I);
28  H=-1; GO TO SEARCH; END;
29  ELSE GO TO NEXT;
30  SUMSQ(1)=SUMSQ(2);
31  SEARCH;END;
32  CYMAX(CYCLE,I)=CYCLE*100+I;
33  NEXT;SOLN(I)=SOLN(I)-H*STEP(I);
34  CALL EQUATE;
35  END;
36  DO K=1 TO 9;
37  IF (SOLN(K)>(HOLD(K)+STEP(K)*0.1))|(SOLN(K)<(HOLD(K)-STEP(K)*0.1))
38  THEN GO TO NO;
39  END;
40  PUT EDIT('FINER SEARCH INITIATED,CYCLE',CYCLE)(SKIP,A(28),F(3));
41      PUT EDIT(CYCLE,SOLN,SUMSQ)(SKIP,F(3),X(2),3 F(7),F(6,3),F(10,2),
42  3 F(7),F(6,3),X(4),2 F(10,3));
43  STEP=STEP*0.25;
44  NO:CYCLE=CYCLE+1;
45  HOLD=SOLN;
46  END;
47  EXIT:PUT SKIP LIST('FINAL SOLN');
48      PUT EDIT(CYCLE,SOLN,SUMSQ)(SKIP,F(3),X(2),3 F(7),F(6,3),E(10,2),
49  3 F(7),F(6,3),X(4),2 F(10,3));
50  PUT SKIP LIST('FINAL VALUES OF EL,HO,EL+HO,COEFF,RATIO');
51  PUT EDIT(EL,HO,EL+HO,COEFF,(EL+HO)/COEFF)(5(SKIP,2 F(12,3),10 E(9,3)));
52  GO TO TEMP;
```

Figure 7.2.

Computer programme for solving equations (4.26)

```
53  EQUATE:PROCEDURE;
54  DCL (A(9),Z(12))FLOAT;
55  P=-1.0; A=SOLN;
56  AGAIN:IF I>5 THEN DO;
57  A(1)=A(6); A(2)=A(7); A(3)=A(8); A(4)=A(9); P=1.0; END;
58  KIN=KIN+1;
59  COS2=A(4)**2; SIN2=1.0-COS2;
60  X=COS2*A(2)+SIN2*A(3);
61  Y1=COS2*A(3); Y2=SIN2*A(2); Y=Y1+Y2;
62  X1=COS2*SIN2*(A(2)-A(3))**2;
63  X2=SQRT(COS2*SIN2)*(A(2)-A(3))*A(5)*0.4E-29;
64  X3=A(1)*X*A(5)*0.8E-29;
65  A23=A(2)*A(3);
66  Z(1)=(A(1)+X)*A(5)*0.8E-19; Z(2)=Y*A(5)*1.6E-19;
67  Z(3)=(A23+A(1)*Y)*A(5)*0.8E-24*P; Z(4)=X3*P*2.0E5;
68  Z(5)=(A(1)+X)*X3; Z(6)=Y*(A23+A(1)*Y)*A(5)*0.8E-29;
69  Z(7)=Y*X3;
70  Z(8)=(Y2*(A(1)-A(3))**2+Y1*(A(1)-A(2))**2+3*A(1)*X1)*A(5)*0.2E-29;
71  Z(9)=(3*Y2*(A(1)**2+A(3)**2)+3*Y1*(A(1)**2+A(2)**2)
72  +A(1)*(X1+2*A23))*A(5)*0.2E-29;
73  Z(10)=A(1)*X1*A(5)*1.6E-29; Z(11)=A(1)*(X-A(1))*X2;
74  Z(12)=(A23-A(1)*Y)*X2;
75  IF I>5 THEN HO=Z; ELSE EL=Z;
76  IF I=0 THEN DO; I=9; GO TO AGAIN; END;
77  IF I=5 THEN DO;I=10; GO TO AGAIN; END;
78  IF I=10 THEN I=5;
79     Q=(((EL(1)+HO(1))/COEFF(1)-5.0)*1.0)**2
80      +(((EL(2)+HO(2))/COEFF(2)-5.0)*1.0)**2
81      +(((EL(3)+HO(3))/COEFF(3)-1.0)*1.0)**2
82      +(((EL(4)+HO(4))/COEFF(4)-2.0)*1.0)**2
83      +((EL(5)+HO(5))/COEFF(5)-1.0)**2
84      +((EL(6)+HO(6))/COEFF(6)-1.0)**2
85      +((EL(7)+HO(7))/COEFF(7)-1.0)**2
86      +((EL(8)+HO(8))/COEFF(8)-1.0)**2
87      +((EL(9)+HO(9))/COEFF(9)-1.0)**2
88      +((EL(10)+HO(10))/COEFF(10)-1.0)**2
89      +((EL(11)+HO(11))/COEFF(11)-1.0)**2
90      +((EL(12)+HO(12))/COEFF(12)-1.0)**2;
91  END EQUATE;
92; END;
93  END ARSENIC;
```

Figure 7.2 (contd.)

STEP	9 element array. Stores the selected increment (or decrement) of each element of SOLN.
MAX,MIN	9 element arrays. Maximum, minimum allowed values of SOLN.
EL,HO	12 element arrays. Store the calculated electron, hole contributions to the coefficients.
COEFF	12 element array. Stores the measured values of the coefficients.
SMALL	Lower limit of SUMSQ.
SUMSQ	2 element array. Defined on page160
H	Sets STEP to increase (H=+1) or decrease (H=-1)SOLN.
J	Number of cycles required of all nine variables
I	Counter for SOLN
CYCLE	Counts the completed number of cycles.
HOLD	9 element array. Stores values of SOLN
Q	Dummy variable for SUMSQ. Used in subroutine.
CYMAX	2 dimentional array:(J,9). Provides a coded print of stage when SOLN is limited by MAX or MIN.

KIN	Counter for number of subroutine entries.
A	Dummy variable for SOLN. Used in subroutine.
Z	Dummy variable for EL,HO. Used in subroutine.
P	Sets sign (+,-) of hall coefficients in subroutine.
ARSENIC	Name of main programme
EQUATE	Name of subroutine

Programme Operation

The numbers in brackets refer to the relevant lines of the programme.

(1-6)	Initial declarations are made (e.g. establishing the dimensions of the arrays).
(7)	MAX, MIN, COEFF, SMALL, J are read from data cards.
(8)	Declaration of CYMAX is made inside a BEGIN block because J must be read first.
(9)	STEP, SOLN are read from data cards.
(10)	Initial values of SOLN are printed.

(11-14) Initial values of certain variables are established.

(15) Subroutine is entered to calculate the initial values of EL, HO, SUMSQ.

(16-17) Initial values of EL, HO, COEFF are printed.

(18) Proceed if CYCLE ≤ J. Otherwise control goes to line 47 and the programme finishes.

(19) I sets sequential operation of elements of SOLN.

(20) SUMSQ (1) is established from Q of the subroutine.

(21) Final answer has been obtained if SUMSQ (1) < SMALL when control passes to line 47.

(22) H is set for STEP increment.

(23) Proceed if SOLN (I) is within the range MAX (I) to MIN (I). Otherwise control goes to line 32.

(24) SOLN (I) is incremented by STEP (I).

(25) Subroutine recalculates Q.

(26) SUMSQ (2) is made equal to Q.

The next few lines comprise the search procedure which minimises SUMSQ.

(27-31) If SUMSQ(2) ≤ SUMSQ(1) a move towards a better answer has been made; control goes to line 30 where the smaller value SUMSQ(2) replaces SUMSQ(1). Line 31 then returns control to line 23 and the procedure is repeated. Eventually the condition SUMSQ(2) > SUMSQ(1) must occur. Two possibilities arise:

(a) A move has been made away from a minimum value of SUMSQ.

(b) SUMSQ is at a minimum, and a move either way gives a larger value of SUMSQ.

Case (a) is covered by resetting SOLN(I) to its original value, changing H to -1 and repeating the search (lines 27, 28).

Case (b) is covered on this next search, since if SUMSQ(2) is still larger than SUMSQ(1) when H = -1, a minimum has been found. Line 29 then causes the next element of SOLN to be called.

(32) Control is received here only if the MAX, MIN condition of line 23 is violated. CYMAX is coded to record when this occurred.

(33) SOLN(I) is set to the value that produced a minimum value of SUMSQ.

(34) Subroutine recalculates EL, HO, SUMSQ.

(35) Control goes back to line 19 where I is incremented to call the next element of SOLN.

(36-39) Control passes to line 36 when all 9 elements of SOLN have been swept. A test is made to see if the new SOLN differs from the previous SOLN (stored in HOLD). Note that it is not possible to say IF SOLN(K) = HOLD(K), because floating point arithmetic is in use.

(40-43) If the same value of SOLN has been found, then a finer search is initiated by dividing the value of STEP by 4.

(44) CYCLE is incremented by 1.

(45) The new SOLN is duplicated into HOLD.

(46) Control passes back to line 18 which causes another cycle of all 9 elements of SOLN.

(47-51) Control reaches line 47 when the permitted number of cycles has elapsed. Final values are printed.

(52) Control goes back to line 7 which repeats the programme for fresh data (e.g. a different temperature).

The remainder of the programme concerns the subroutine, EQUATE, which evaluates the equations.

(53) Entry to EQUATE.

(54) Declaration of A and Z is made.

(55) P is set to evaluate the electron terms of the hall coefficients. SOLN is read into A.

(56,57) To save computing time, only the terms relevant to the particular variable are computed. i.e. the electron terms are computed for SOLN(1,2,3,4,) and the hole terms for SOLN(6,7,8,9). Both are calculated for SOLN(5). Thus if I>5 the hole variables, A(6,7,8,9) are put into A(1,2,3,4) and P is changed to +1.

(58) KIN is incremented every time the equations are evaluated.

(59-74) These lines are the equations (4.26) written in a form that minimises the computing time.

(75) If I>5, hole terms have been calculated

and Z is put into HO. If I $\leq$ 5 Z goes into EL.

(76) For the initial calculation, when I = 0, both EL and HO must be obtained. Thus I is changed to 9 and EQUATE repeats for the hole terms by going back to line 56. I will be reset to 1, on return to ARSENIC, at line 19.

(77) If I = 5, HO is obtained by changing I to 10 and returning to line 56.

(78) After calculating HO for I = 5, I is reset to 5 before the return to the main programme.

(79-90) Q (i.e. SUMSQ) is computed. Time is saved by not using a DO loop.

(91-93) Terminations.

The programme was run on a large computer (IBM 360/67). Each evaluation of the equations took only 1 mS; 500 cycles of the 9 variables were executed for the data at each temperature. All six temperatures were analysed in a total time of 3 minutes.

VII.3. Results

a. Reassessment of the antimony data.

To test the programme, the data for antimony at ice

temperature (Oktu and Saunders 1967) were reassessed. Improved fits to the coefficients resulted; see table 7.1. The SUMSQ value is improved from 0.29 to 0.05. Seven coefficients are closer to their measured values, four slightly worse and one unchanged. In particular the large discrepancies for B_{33} and B_{44} are removed (1.4 → 1.08 and 1.3 → 1.01). It was hoped that the new method of solving the equations might resolve the anomalous values (see page 180) of Ψ_h and N. But this was not to be. The only significant change is of μ_2 from 110 $cm^2V^{-1}S^{-1}$ to 46 $cm^2V^{-1}S^{-1}$ (see table 7.2).

b. Application to the arsenic data.

To ensure that all solutions have been found, a range of parameters that start the calculation (point Z of figure 7.1) must be tried. Only one acceptable solution, that given in table 7.3 was obtained; convergence to this solution was rapid from widely different starting points. Three other fits to the equations were readily rejected for the following reasons:

1. A higher residual value of SUMSQ indicated a poorer fit than the result given in table 7.3.
2. The electron tilt angle showed no agreement at all with the value found by Priestley et al. (1967).
3. Energy ellipsoids would have to be oblate rather than the expected prolate form.

	ANTIMONY	
	Oktu and Saunders	Reassessed
σ_{11}	0.99	1.00
σ_{33}	1.00	1.00
$-P_{231}$	0.99	1.00
$-P_{123}$	0.99	1.00
B_{13}	0.87	0.84
B_{31}	0.90	0.88
$-B_{44}$	1.30	1.01
B_{11}	1.02	0.95
B_{12}	1.04	1.02
B_{33}	1.40	1.08
$-B_{24}$	1.08	1.05
$-B_{42}$	1.00	0.98
SUMSQ.	0.29	0.05

Table 7.1

Ratios of calculated to measured coefficients for antimony data at ice temperature (Oktu and Saunders 1967) reassessed, to test the new method of solution.

ANTIMONY

	N	μ_1	μ_2	μ_3	ψ_e	ν_1	ν_2	ν_3	ψ_h
Oktu and Saunders	0.422	2740	110	1950	-3^o	3630	180	3220	-24^o
Reassessed	0.406	2230	46	2460	-8^o	3820	210	3170	-21^o

Units : as in table 7.3.

Table 7.2.

The reassessed solution for the antimony data.

The solution given in table 7.3 presents, for the first time, detailed information of carrier densities and mobilities in arsenic over a wide temperature range. The invariance of the ellipsoid tilt angles with temperature is satisfying; the finding that carrier density is essentially temperature independent verifies degeneracy. The anomalous behaviour of μ_2 is not necessarily significant. As is shown in table 7.4, the electron contribution to many coefficients is small; further μ_2 is swamped by μ_1 and μ_3. Thus SUMSQ is very insensitive to the value of μ_2 and an accurate value of μ_2 cannot be obtained. The quality of the fit of the solution is illustrated by the ratios of calculated to measured coefficients (table 7.5). It is interesting that the discrepancies are consistent over the whole temperature range: a point that is amplified later (page 200).

Temp. (^{o}K)	N	μ_1	μ_2	μ_3	ψ_e	ν_1	ν_2	ν_3	ψ_h	'SUMSQ'
305	2.16	460	40	550	-8^{o}	1210	50	680	-50^{o}	0.307
250	2.04	650	50	740	-8^{o}	1570	85	950	-50^{o}	0.274
215	2.03	840	25	950	-8^{o}	1960	120	1220	-50^{o}	0.258
175	1.98	1170	24	1300	-8^{o}	2550	180	1700	-50^{o}	0.257
125	1.90	2020	16	2240	-8^{o}	4140	340	2880	-50^{o}	0.248
77	1.92	4600	0	5300	-8^{o}	8700	830	6600	-51^{o}	0.230

Units: N, $10^{-20}cm^{-3}$; μ, ν, cm^2 $Volt.^{-1}$ $sec.^{-1}$; ψ, degrees.

Table 7.3.

Band and mobility parameters for arsenic,

assuming ellipsoidal energy bands.

Coefficient	Electron Contribution	Hole Contribution	Total	Calculated / Measured
σ_{11}	0.89×10^4	2.82×10^4	3.71×10^4	0.99
σ_{33}	1.88×10^4	1.06×10^4	2.94×10^4	1.00
$-P_{231}$	-47.4	+70.0	+22.5	0.99
$-P_{123}$	- 8.5	+175	+167	1.04
B_{13}	0.021	1.43	1.45	0.71
B_{31}	0.257	0.214	0.472	0.66
$-B_{44}$	0.023	0.268	0.291	1.21
B_{11}	0.043	0.317	0.361	1.03
B_{12}	0.161	0.687	0.849	1.08
B_{33}	0.008	0.401	0.409	0.82
$-B_{24}$	0.011	0.258	0.270	1.07
$-B_{42}$	0.014	0.090	0.104	1.05

Units : conductivity, $ohm^{-1}cm.^{-1}$; Hall, $ohm^{-1}cm.^{-1}Kg^{-1}$; magnetoconductivity, $ohm^{-1}cm.^{-1}Kg^{-2}$.

Table 7.4.

The electron and hole contributions to the magnetoconductivity coefficients at $305^{o}K$. The holes dominate.

Coefficient.	Temperature (^{o}K)					
	305	250	215	175	125	77
σ_{11}	0.99	0.99	0.99	0.99	0.99	1.00
σ_{33}	1.00	1.00	1.00	1.00	1.00	1.00
$-P_{231}$	0.99	0.99	0.99	0.99	0.99	0.99
$-P_{123}$	1.04	1.04	1.04	1.05	1.05	1.04
B_{13}	0.71	0.70	0.70	0.70	0.69	0.70
B_{31}	0.66	0.70	0.72	0.72	0.76	0.79
$-B_{44}$	1.21	1.22	1.21	1.22	1.21	1.25
B_{11}	1.03	1.04	1.03	1.00	0.98	0.95
B_{12}	1.08	1.07	1.07	1.07	1.05	1.00
B_{33}	0.82	0.84	0.85	0.85	0.85	0.87
$-B_{24}$	1.07	1.06	1.06	1.06	1.06	1.07
$-B_{42}$	1.05	1.03	1.04	1.06	1.08	1.07

Table 7.5

The ratios of calculated to measured coefficients for the solution given in table 7.3. Note the systematic deviations from unity of each coefficient over the whole temperature range.

CHAPTER VIII

GALVANOMAGNETIC EFFECTS AND THE FERMI SURFACE OF ARSENIC

VIII.1. A Comparison between Quantum Resonance and Galvanomagnetic Data.

In this concluding chapter the results of the galvanomagnetic measurements are compared with other investigations of electrical properties. No other details of electrical carrier mobilities are known and so the comparisons are with somewhat different types of experiment. In this section three parameters of the Fermi surface - carrier densities ($N = P$) and ellipsoid tilt angles (ψ_e, ψ_h) - are compared to measurements made by quantum resonance experiments; in particular those of Priestley et al. (1967). It should be noted that the mobility tilt angles of table 7.3 are transformed to the tilt angles of the normals to the planes of minimum area of the Fermi pockets. The high mobilities μ_1, μ_3 and ν_1, ν_3 which define the planes of maximum area of the mobility ellipsoids lie in these planes of minimum area of the Fermi ellipsoids. Thus the mobility and energy ellipsoids are orthogonal and it follows that the required tilt angles are obtained by adding 90° to ψ_e and ψ_h ; see figure 8.1. It may be seen from table 8.1 that, considering the simplifications made in the model of the Fermi

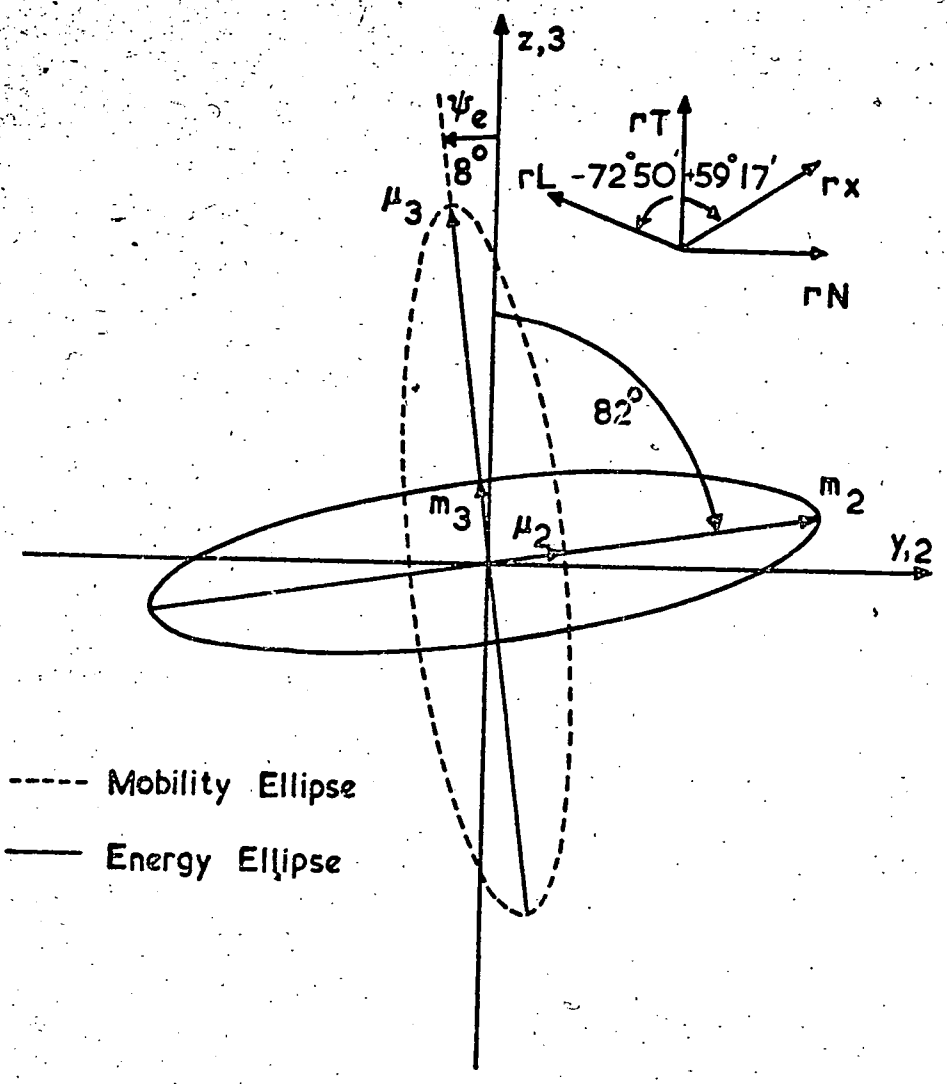

Figure 8.1.

The relation between tilt angle of mobility (-----) and energy (——) surface of the electrons. A tilt of 8° towards ΓL of the high mobility μ_3 is equivalent to a tilt of 82° towards ΓX of the direction normal to the plane of minimum area of the energy ellipsoid.

	Tilt Angle			
	electron pockets		hole pockets	Carrier Densities
	(minimum area)	(maximum area)	(minimum area)	($cm.^{-3}$)
pseudopotential calculation (Lin and Falicov 1966)	80^{o}	171^{o}	44^{o}	
De Haas-van Alphen effect (Priestley et al. 1967)	86^{o}	171^{o}	37^{o}	2.12×10^{20} (at $4.2^{o}K$)
this work	82^{o}	172^{o}	40^{o}	2.16×10^{20} (at $305^{o}K$)
				1.92×10^{20} (at $77^{o}K$)

Table 8.1.

A comparison of the solution of the ellipsoidal model to published details of the Fermi surface of arsenic.

surface, agreement is surprisingly good : carrier densities agree to within 10% and both tilt angles to a few degrees. Indeed the agreement is much better than in the case of antimony, shown in table 8.2 (Oktu and Saunders 1967) where carrier densities and one tilt angle agree to only 50%. This is strange since the de Haas-van Alphen experiments demonstrate that the arsenic Fermi surface deviates from ellipsoidal shape far more than does that of antimony. The answer may be in the assumption that a best fit to the equations (4.26) is the closest physical solution. For antimony, the Fermi surface distortions may be such that forcing the galvanomagnetic data to fit an ellipsoidal model as closely as possible causes N to decrease with a compensating decrease in ψ_h. But since the only meaningful solution to the equations (4.26) is the one that is as near exact as possible, this is only another way of saying that the ellipsoidal model is not sufficient to interpret the effects in antimony as accurately as in arsenic. The dilemma remains; but this argument indicates a possible way to examine the matter further.

Other quantum resonance experiments (Berlincourt 1955, Ketterson and Eckstein 1965, Vanderkooy and Datars 1967) have indicated tilt angles of similar values. The earlier work was not complete due to an ambiguity in assigning electron and hole orbits to their respective pockets : the long ~~long~~ period oscillations, shown by Priestley to arise from the hole necks, were assumed to result from electron pockets; all short period oscillations were attributed

	Tilt Angle				
	electron pockets (Minimum area)	electron pockets (Maximum area)	hole pockets (Minimum area)	hole pockets (Maximum area)	Carrier Densities ($cm.^{-3}$)
pseudopotential calculation (Falicov and Lin 1966)	87.5^{o}	173^{o}	41^{o}		
De Haas-van Alphen effect (Windmiller 1966)	87.7^{o}	173.5^{o}	52.6^{o}		5.5×10^{19} (at $4.2^{o}K$)
Galvanomagnetic effects (Oktu and Saunders 1967)	85^{o}	175^{o}	66^{o}	156^{o}	4.2×10^{19} (at $273^{o}K$) 3.9×10^{19} (at $77^{o}K$)

Table 8.2.

The comparison to table 8.1 for antimony (Oktu and Saunders 1967).

to the hole surfaces.

One further important point is that the galvanomagnetic measurements provide the first direct experimental confirmation of the theoretical prediction by Lin and Falicov (1966) that electrons occupy the high-tilt and holes the medium-tilt pockets.

VIII.2. Fermi Energies : the Seebeck Effect.

Despite the generally good agreement between Priestley et al. (1967) and Lin and Falicov (1966) the effective masses and Fermi energies are in discord. (see table 2.1, 2.2). Galvanomagnetic measurements may be used to determine Fermi energies by an analysis that incorporates the Seebeck effect. Results have already been published for bismuth (Gallo et al. 1963) and antimony (Saunders and Oktu 1968). A similar, brief analysis of the Seebeck effect in arsenic is now presented.

The thermoelectric power, S, of arsenic is a second rank tensor, like the electrical conductivity :

$$S_{ij} \equiv \begin{matrix} S_{11} & 0 & 0 \\ 0 & S_{11} & 0 \\ 0 & 0 & S_{33} \end{matrix}$$

On the assumption of independent contributions to electrical conductivity and thermoelectric power by the electrons and holes, partial Seebeck coefficients P_e, P_h and conductivity coefficients

$(\sigma_{11})_e$, $(\sigma_{11})_h$, $(\sigma_{33})_e$, $(\sigma_{33})_h$ may be defined. Then :-

$$S_{11} = \frac{(\sigma_{11})_e P_e + (\sigma_{11})_h P_h}{(\sigma_{11})_e + (\sigma_{11})_h}$$

and $$S_{33} = \frac{(\sigma_{33})_e P_e + (\sigma_{33})_h P_h}{(\sigma_{33})_e + (\sigma_{33})_h}$$

Substituting for σ_{11} and σ_{33} from equations (4.26) these may be written:

$$S_{11} = \frac{A_x P_e + P_h}{A_x + 1} \qquad (8.1a)$$

and $$S_{33} = \frac{A_z P_e + P_h}{A_z + 1} \qquad (8.1b)$$

where $$A_x = \frac{\mu_1 + C_e^2 \mu_2 + S_e^2 \mu_3}{\nu_1 + C_h^2 \nu_2 + S_h^2 \nu_3}$$

and $$A_z = \frac{S_e^2 \mu_2 + C_e^2 \mu_3}{S_h^2 \nu_2 + C_h^2 \nu_3}$$

A_x and A_z are 'mobility ratios'. Figure 8.2 shows that both are only weakly temperature dependent.

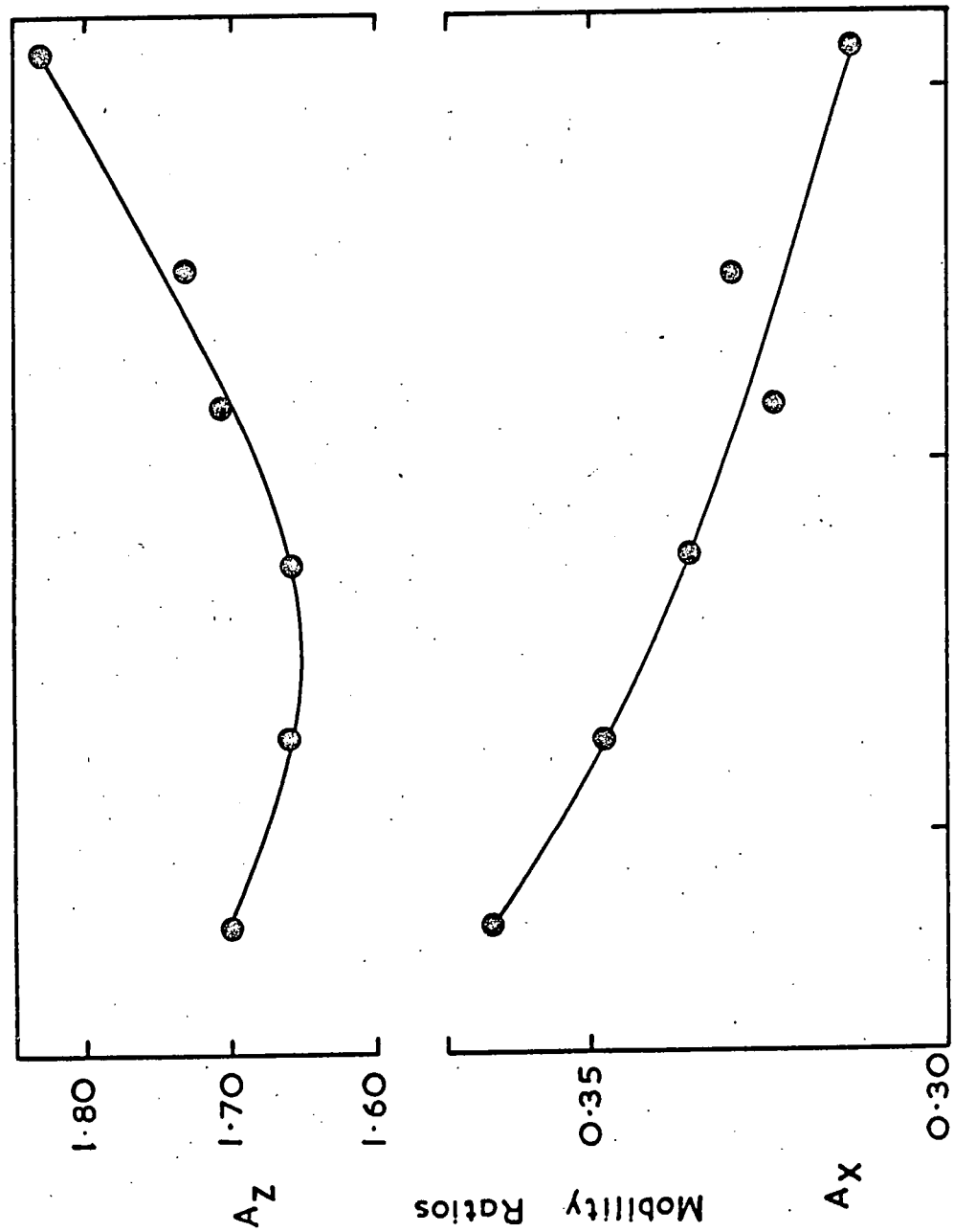

Figure 8.2

The temperature dependence of the mobility ratios.

Equations (8.1) may be rearranged to give:

$$P_e = \frac{(A_x+1)S_{11} - (A_z+1)S_{33}}{A_x - A_z} \qquad (8.2a)$$

$$P_h = \frac{A_x(A_z+1)S_{33} - A_z(A_x+1)S_{11}}{A_x - A_z} \qquad (8.2b)$$

The partial Seebeck coefficient may be evaluated using the mobility ratios of figure 8.2 in conjunction with experimental values of S_{11} and S_{33}. Because published data (Saunders et al 1965), - given in figure 8.3 - leads to a positive value of P_e, brief measurements of S_{11} and S_{33} were made on two of the galvano-magnetic samples. A very simple experimental system was employed. It comprised copper constantan thermocouples at each end of the crystal; partial immersion in liquid nitrogen was used to change the temperature. Absolute thermopowers are shown in figure 8.4. They were obtained by allowing for the thermopower of copper according to the data of Cusack and Kendall (1958). A most significant fact, which was carefully checked, is that S_{33} is negative, not positive as reported by Saunders et al (1965). It follows that P_e is now negative, as anticipated. The non-linearity in S_{33} below $100^{o}K$ resembles a 'phonon-drag' peak. This may be due to the copper measuring leads rather than the arsenic crystal. P_e and P_h, deduced from equations (8.4) are given in figure 8.5. These values are now

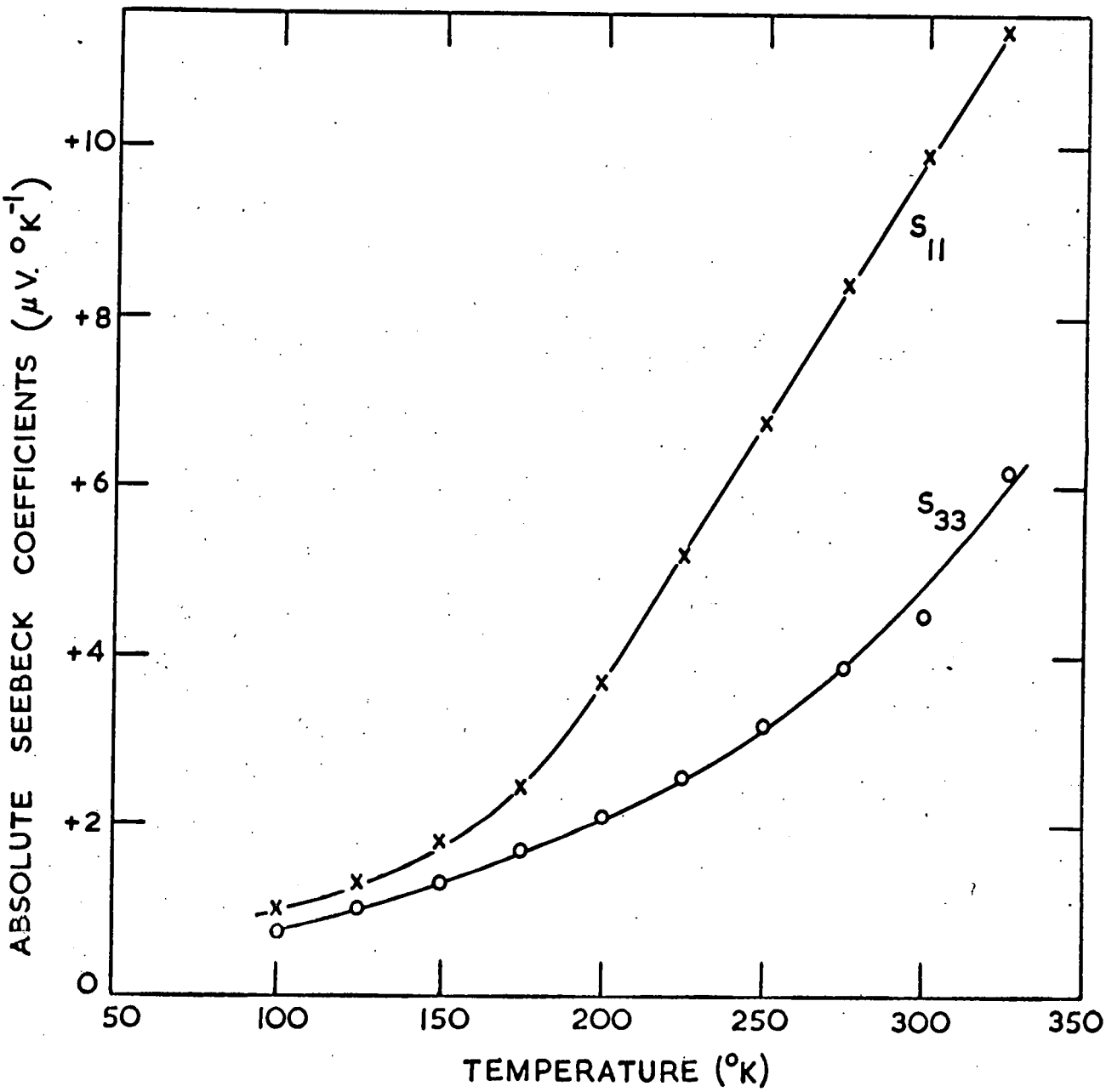

Figure 8·3 The Seebeck coefficients of Arsenic according to Saunders et al. (1965) Note that S_{33} is positive.

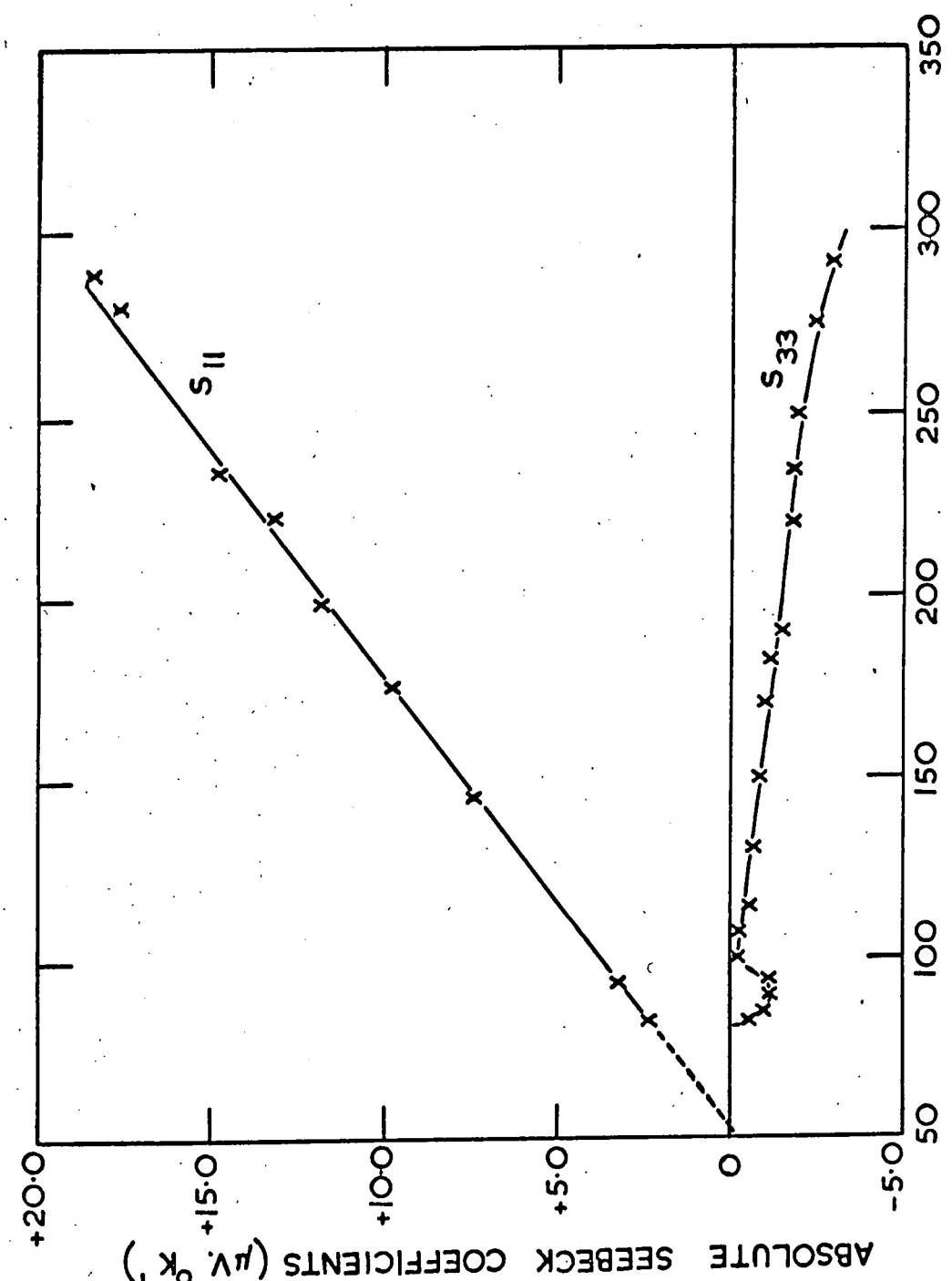

Figure 8·4 The Seebeck coefficients of Arsenic remeasured S_{33} is negative.

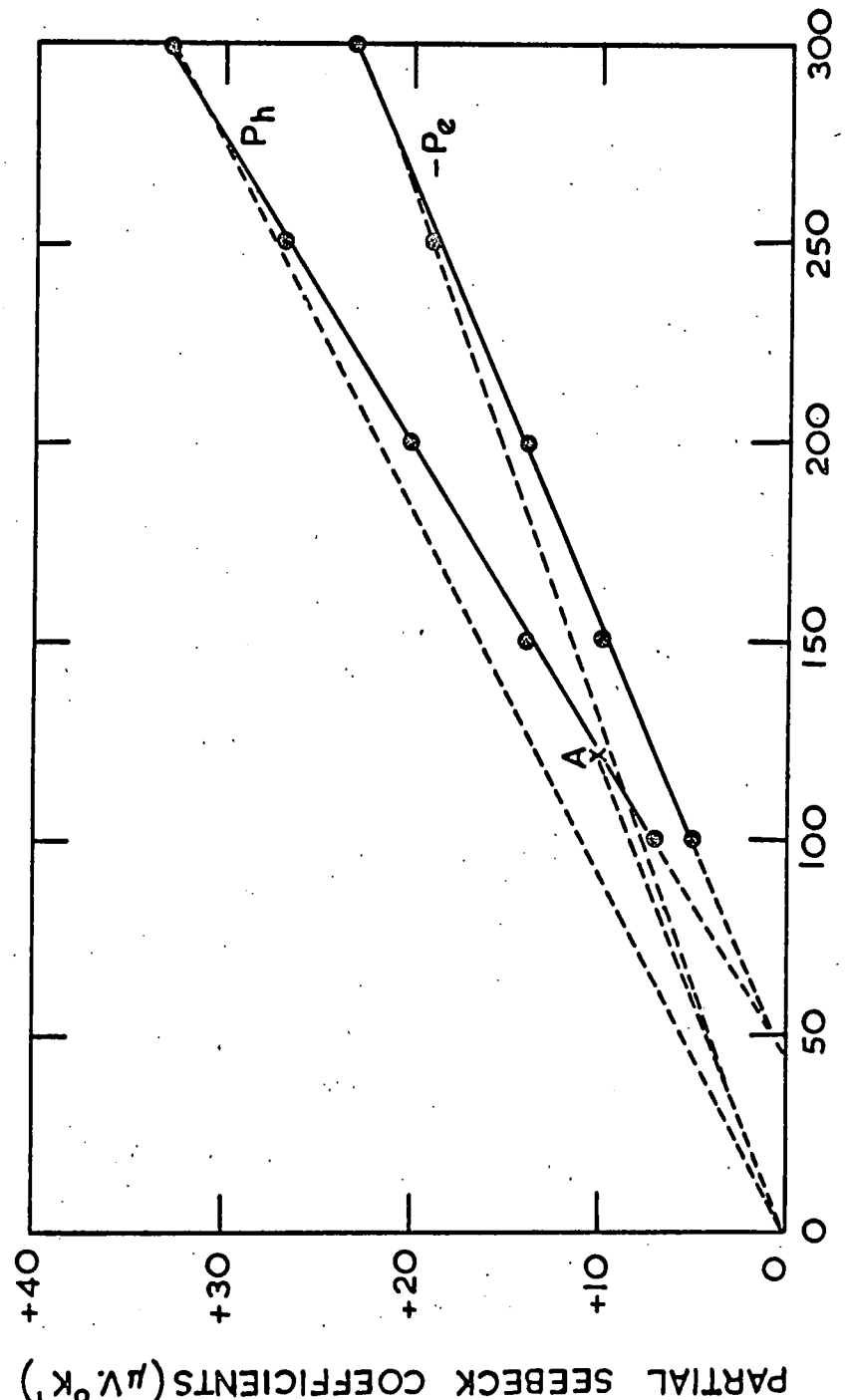

Figure 8.5. The partial Seebeck coefficients of Arsenic.

used to calculate electron and hole Fermi energies on the very restrictive assumption of acoustic mode intra-valley scattering governed by an isotropic relaxation time. A discussion on carrier scattering is the content of the next section. Then :

$$P_e = - \frac{k}{|e|} \frac{(5/2+s)\ F_{3/2+s}\ (\xi_e)}{(3/2+s)\ F_{1/2+s}\ (\xi_e)} - \xi_e$$

$$P_h = + \frac{k}{|e|} \frac{(5/2+s)\ F_{3/2+s}\ (\xi_h)}{(3/2+s)\ F_{1/2+s}\ (\xi_h)} - \xi_h$$

s is the exponent of the energy dependence of the relaxation time; F denotes a Fermi integral :

$$F_j\ (\xi) = \int_0^\infty \frac{x^j}{e^{x-\xi}+ 1}\ dx$$

where ξ is the reduced Fermi energy, $\xi = \frac{E_F}{kT}$.

For degenerate material and acoustic mode scattering when s = -1/2 : (See Smith 1959).

$$P_e = - \frac{\pi^2 k^2}{3|e|} \left(\frac{T}{E_F}\right) = - 2.45 \times 10^{-2} \left(\frac{T}{E_F}\right) \mu V/^oK \quad (8.3a)$$

$$P_h = + \frac{\pi^2 k^2}{3|e|} \left(\frac{T}{E_F^h}\right) = +2.45\times10^{-2} \left(\frac{T}{E_F^h}\right) \mu V/^oK \qquad (8.3b)$$

T is the temperature in ^oK and E_F^e, E_F^h the Fermi energies in eV.

Equations (8.3) state that a plot of P_e, P_h against T should be a straight line through the origin. Then the Fermi energy is proportional to the inverse gradient of this line. Examination of figure 8.5 reveals a problem. The plots are linear, but do not pass through the origin: the linear extrapolations at low temperatures cut the temperature axis at 50^oK. There would not seem to be any significance in the fact that P_e and P_h show the same intercept: both are dominated by S_{11} which also has this intercept (see figure 8.4). It is interesting to examine the data for antimony (Saunders and Oktu 1968). In this case S_{11} and S_{33} like arsenic, do not pass through the origin. But P_e, P_h do because the S_{11}, S_{33} intercepts cancel on substituting in equations (8.2). This problem places doubt on the accuracy of the present arsenic thermopower data. If one proceeds by taking the ratio T/P_e and T/P_h as required by equations 8.3 it leads to the quite unacceptable conclusion that E_F^e and E_F^h increase rapidly with decreasing temperature. E_F^h is proportional to T/P_h, which is the inverse gradient of OA in figure 8.5, and as temperature decreases OA becomes more horizontal, which implies that E_F^h increases.

Four other interpretations of the data are possible :-

1. An experimental error exists.
2. Due, perhaps, to the hole necks, a non-linear approach to zero by P_e, P_h applies .

3. The assumption of intravalley acoustic mode scattering is insufficient.

4. A non-diffusion effect - e.g. phonon drag occurs.

In all of these cases, it is probably fair to assume that the higher temperature data is more accurate and so draw a line through the points at 250°K and 300°K and through the origin. The resulting Fermi energies may be compared to other estimates :-

	E_F^e	meV. E_F^h	-Eg
Seebeck effect - this work	320	220	540
Priestley et al. (1967)	190	177	367
Lin and Falicov (1966)	366	326	728

The general disagreement is obvious. The band overlap, shown as a negative gap, (-Eg) ranges from one third to three quarters of an electron volt. It should be noted that Priestley's values are derived from a parabolic approximation.

VIII.3. Carrier Scattering in Arsenic.

a. Theoretical considerations.

In chapter IV the Boltzmann equation (4.6) is derived on the assumption that the scattering term may be represented by a relaxation time

$$\left[\frac{\partial f_{\underline{k}}}{\partial t}\right]_{\text{scattering}} = \frac{1}{\tau}(f_{\underline{k}} - f_{\underline{k}}^{o})$$

More generally, the scattering term may be written :

$$\left[\frac{\partial f_{\underline{k}}}{\partial t}\right]_{\text{scattering}} = \int \left[f_{\underline{k}'}(1-f_{\underline{k}}) - f_{\underline{k}}(1-f_{\underline{k}'}) \right] Q(\underline{k},\underline{k}')\,d\underline{k}' \qquad (8.4)$$

$f_{\underline{k}}$ is decreased by the scattering of carriers from a state $\underline{k}$ to $\underline{k}'$ and the rate of decrease depends on $f_{\underline{k}}$, the density of carriers in $\underline{k}$ and on $(1 - f_{\underline{k}'})$, the density of vacancies in $\underline{k}'$. The reverse process gives a term $f_{\underline{k}'}(1-f_{\underline{k}})$ and increases $f_{\underline{k}}$. In both cases the probability of a transition between the states is the same : $Q(\underline{k}, \underline{k}')$. The expression must be summed over all allowable states $\underline{k}'$.

The relaxation time approximation is the only simple solution to this equation, and Wilson (1953) has derived expressions for the relaxation times in metals and semimetals for the following assumptions:

1. Elastic scattering between electrons and phonons.
2. $\varepsilon_{\underline{k}}$ is a function (quadratic) of $|\underline{k}|$ and so has spherical symmetry.
3. The frequencies of the lattice vibrations are those of an elastic continuum.

We have two cases :-

$$\text{Metals} \quad : \tau = \frac{2\hbar^2 \Lambda}{(m^*/2)^{\frac{1}{2}} D} \frac{\theta}{T} \varepsilon^{3/2} \qquad (8.5a)$$

$$\text{Semimetals} \quad : \tau = \frac{\hbar^2 D \Lambda}{2(m^*/2)^{\frac{1}{2}}} \frac{\theta}{T} \frac{1}{\varepsilon^{\frac{1}{2}}} \qquad (8.5b)$$

T denotes temperature; Λ and D are constants of the crystal. θ is the Debye temperature and ε the carrier energy.

The semimetallic expression applies if the number of conduction electrons per atom, N_a, is less than 0.25. (In arsenic $N_a \sim 0.005$). The reason for this is as follows. Assuming one closed surface - or, if several, independent scattering - the largest wave-number involved in scattering as far as electrical conduction is concerned is that of a phonon that takes a carrier from one side of the Fermi surface to the other : $2|k_F|$. When N_a is small, $2|k_F|$ is small and scattering is restricted to long wavelength (small wave-number) phonons. The range of integration over $\underline{k}'$-states in equation 8.4 is restricted to give the semimetallic expression.

The most significant difference between these two expressions is the dependence of relaxation time on carrier energy.

Metals : $\tau \propto \varepsilon^{3/2}$

Semimetals : $\tau \propto \varepsilon^{-1/2}$

The basic properties of semimetals - long relaxation times and thus high carrier mobilities - stems from this fact.

The applicability of the assumptions made, in the galvanomagnetic analysis, about the relaxation time approximation is now discussed.

b. The validity of an isotropic relaxation time.

Relaxation time and carrier mobility are linked by the formula :

$$\underline{\mu} = \frac{e\tau}{\underline{m}^*} .$$

If τ is isotropic, then the ratios $\mu_1 : \mu_2 : \mu_3$ should accord with the inverse effective mass ratios $1/m_1 : 1/m_2 : 1/m_3$. Unfortunately, for holes in arsenic, no mass data is quoted by Priestley because of the non-ellipsoidal nature of the surfaces. And earlier mass data (Berlincourt 1955, Datars and Vanderkooy 1965) is unreliable because of the confusion in assigning the carrier orbits to their respective pockets. Even in the electron case there is the restriction that μ_2 is not known accurately (see p173). The only results of the comparison are that the ratio $\mu_3 : \mu_1$ (=1.2:1) accords with the ratio $m_1 : m_3$(=1.5:1) and that the low mobilities μ_2, ν_2 are definitely the heavy mass directions.

In fact the isotropic assumption may be relaxed a little and $\underline{\tau}$ written as a tensor :

$$\underline{\mu} = e\underline{\tau}\tau . \ m^{*-1}$$

Then the isotropic assumption is reasonable if the tensor components are within 2:1 (Herring and Vogt 1956). Using, again, the effective mass data of Priestley et al. (1967), τ_1 and τ_3 for

electrons are presented in table 8.3. The general value of relaxation time may be contrasted to that of other semimetals of different carrier densities (table 8.4).

c. The dependence of mobility on temperature.

It may be seen from formulae 8.5 that an inverse relationship is expected between relaxation time, and thus mobility, and temperature in both metallic and semimetallic cases. Figure 8.6 demonstrates that this law does not hold in arsenic: the temperature exponent of -1.7 for μ_1, μ_3 and ν_3 is even further from -1.0 than the exponent for antimony (-1.5, see Oktu and Saunders 1967).

Clearly, the formula $\tau \propto T^{-1} \varepsilon^{-\frac{1}{2}}$ for scattering in a semimetal is insufficient. This is not surprising considering the simple model of the energy bands that is used to derive the formula. The discrepancy probably stems from the assumption of intra-valley scattering only, which as explained on page 193 concerns only long wavelength phonons. In contrast, inter-valley scattering requires relatively high energy, large-$\underline{k}$ phonons. These are few in number at low temperatures, but as temperature rises their population increases. Thus if intervalley scattering is involved, its contribution will increase with temperature so that carrier mobility will fall faster than the simple formula indicates. Herring (1955) has examined this situation for non-degenerate multivalley semiconductors. The temperature exponent can increase from -1.5 up to -3.0 depending on the proportion of inter to intra-valley scattering, the frequency of the intervalley mode and the

	Temperature (^{o}K)					
Relaxation times	305	250	215	175	125	77
Electrons : τ_1	0.42	0.60	0.87	1.08	1.87	4.2
τ_3	0.33	0.44	0.56	0.77	1.33	3.25

Units : 10^{-13}sec.

Table 8.3.

Relaxation times in arsenic.

Element	Carrier Density ($cm.^{-3}$)	Relaxation Time (Secs)
Bismuth	4.6×10^{17}	$\sim 10^{-11}$
Graphite	2.2×10^{18}	$\sim 2 \times 10^{-12}$
Antimony	5.5×10^{19}	$\sim 7 \times 10^{-13}$
Arsenic	2.1×10^{20}	$\sim 3 \times 10^{-13}$

Table 8.4.

Average relaxation times at $77^{o}K$ for some semimetallic elements.

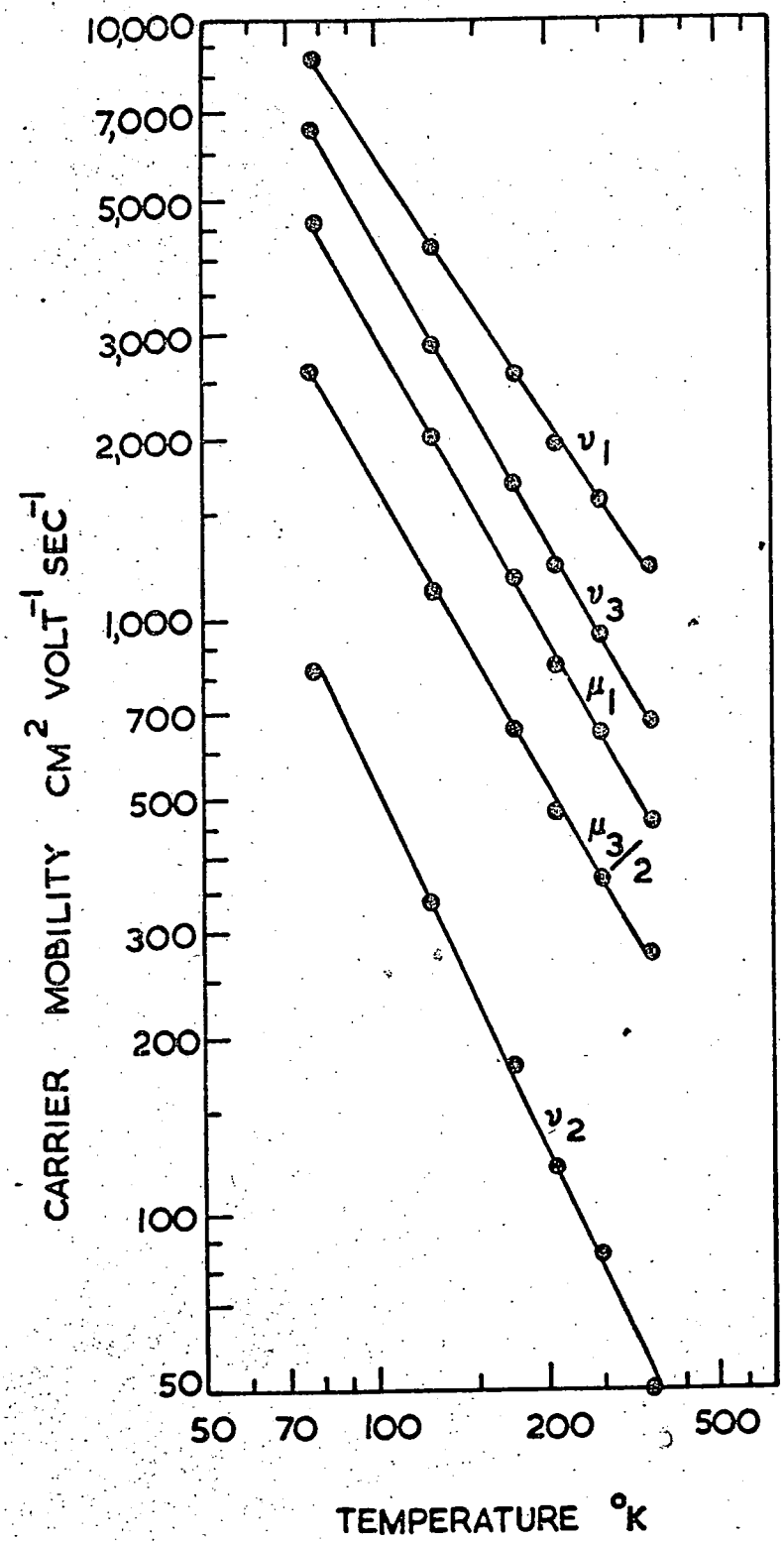

Figure 8.6.

Mobility-temperature dependence. μ_1, μ_3 and ν_3 show a slope of -1.7. ν_1 shows -1.5 and ν_2 -2.0. The values of μ_3 are halved to avoid confusion of points.

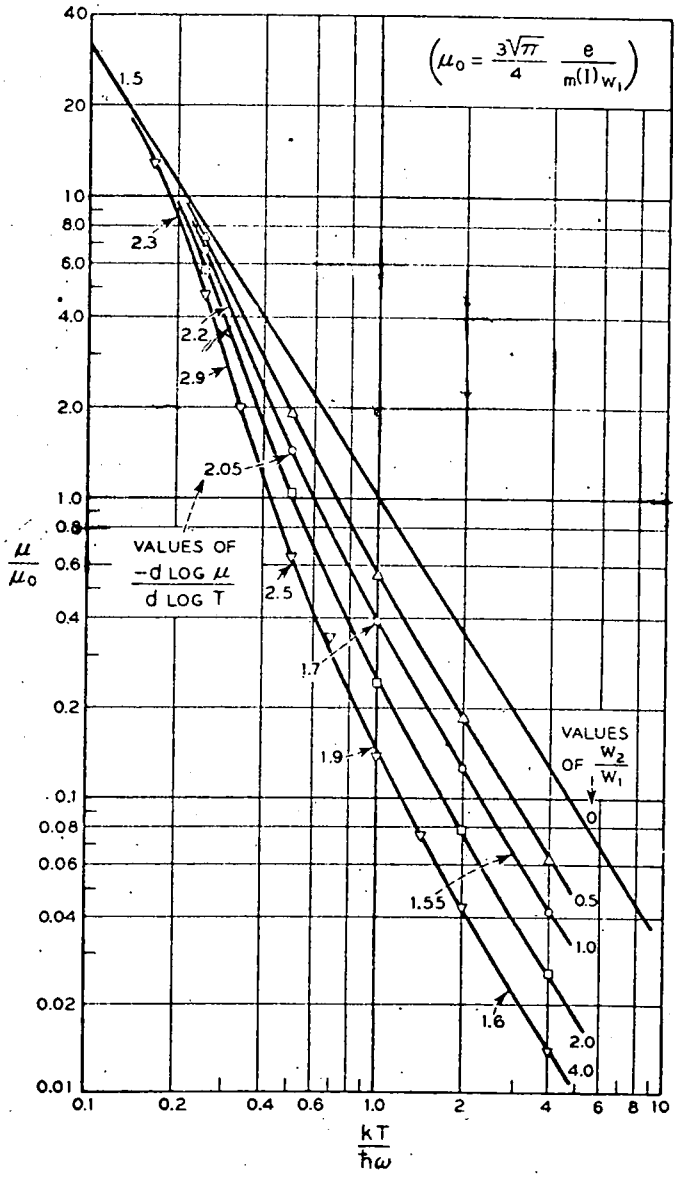

Figure 8.7.

Mobility-temperature curves for various proportions of intra to intervalley scattering. The quantities ω_1 and ω_2 measure the strength of the coupling of the carriers to intra and intervalley modes respectively; ω is the frequency of the intervalley mode. (after Herring 1955).

temperature range: see figure 8.7. The 'turn-up' in μ/μ_o (centre of figure 8.7) may be compared to a similar 'turn-up' in the conductivity of arsenic at low temperatures (figure 6.7 on page 146).

VIII.4. Further Observations.

a. The Fermi surface 'necks'

It is clear from table 7.5 that consistent discrepancies exist between the measured and calculated values of B_{13}, B_{31}, B_{44}, B_{33}. Assuming no systematic experimental error, these discrepancies plausibly reflect the most noticeable departure of the Fermi surface from ellipsoidal shape: the 'necks' which contain low-mass, highly-mobile holes. Despite the low number of carriers in these 'necks' compared to the main pockets, some B_{ij} may be significantly affected because of their dependence on the cubes of mobilities. As a qualitative argument we may assume that the holes in these necks have a density Q equal to 1% of N and an average mobility, γ_{av}, that is five time the average mobility of the principal carriers.

i.e. $Q \approx N/100$; $\gamma_{av} \approx 5\mu_{av} \approx 5\nu_{av}$.

Then :-

$$\sigma_{ij} = Ne\mu_{av} + Pe\nu_{av} + Qe\gamma_{av} = Ne\mu_{av}(2 + 5/100);$$

i.e. the low-mass holes contribute 2½% to σ_{ij}

$$P_{ijk} = Ne\mu_{av}^2 + Pe\nu_{av}^2 + Qe\gamma_{av}^2 = Ne\,\mu_{av}^2(2 + 25/100)$$

a contribution of 9% to P_{ijk}

$$B_{ij} = Ne\mu_{av}^3 + Pe\nu_{av}^3 + Qe\gamma_{av}^3 = Ne\mu_{av}^3(2 + 125/100)$$

a contribution of 38% to B_{ij}

Thus the carriers in the necks may affect some B_{ij} outside the general experimental error. Possibly they completely dominate certain of the higher order galvanomagnetic tensors.

b. Interband transitions.

Maltz and Dresselhaus (1968) have examined the band structure of arsenic from measurements of infra-red magnetoreflectivity. They report a band gap of 0.346 eV between band extrema at T in the Brillouin zone. This does not agree with Lin and Falicov's pseudopotential calculation which predicts a smallest band gap of 1 eV at T. A disagreement of this nature is not particularly surprising. The pseudopotential parameters in Lin and Falicov's calculation have been adjusted so that the results fitted the de Haas-van Alphen data i.e. to fit details of the band structure close to the Fermi energy. It is not perhaps unlikely that other details might disagree. Indeed, as has already been observed, the calculation does not even predict the observed effective masses or Fermi energies.

c. Electronic specific heat.

Ignoring the hole necks, overall close agreement is manifest between the galvanomagnetic analysis and data from the de Haas-van Alphen effect. A further success of the ellipsoidal approximation

to the Fermi surface is the agreement between the calculated value (0.192 mJ. mol^{-1}. $^{o}K^{2}$, Priestley et al. 1967). and measured value (0.194 $\pm$ 0.007, Culbert 1967; 0.186 $\pm$ 0.002, Taylor et al.1967). of the temperature coefficient of the electronic specific heat.

VIII.5. Conclusion

In chapter II the objective of comparing Lin and Falicov's and the ellipsoidal model of the Fermi surface was set. The conclusion is that the ellipsoidal model fits various experimental data remarkably well. This is rather surprising. Lin and Falicov's work suggests that the arsenic Fermi surface deviates even more from ellipsoidal than does that of antimony. And the analysis of the galvanomagnetic effects in antimony has revealed anomalies that have been ascribed to the non-ellipsoidal nature of the pockets. Possibly the arsenic parameters are relatively insensitive to the particular non-ellipsoidal shape. Alternatively, we have seen that the Lin and Falicov surface does not agree with some experimental data. Perhaps the true Fermi surface of arsenic is less distorted than they suggest.

A number of questions remain only approximately answered; much interesting work remains to be done. Generally, there are two main topics: carrier scattering and non-ellipsoidal energy surfaces. Both of these could benefit greatly from the modern developments in numerical techniques and computing power.

The matter of carrier scattering is perhaps the most unknown factor. Only the most basic ideas have been incorporated in this

work. The dependence of carrier mobility on temperature shows that there is strong reason to doubt the approximations. Perhaps a starting point would be to examine the points made by Herring (1955) and rework them for degenerate statistics. With experimental data now available on mobilities and effective masses practical application should be possible. Further experimental help may come from measurements of the thermomagnetic effects which are very sensitive to scattering mechanisms. Of immediate concern is a detailed measurement of the Seebeck effect in arsenic, extending to low temperatures to establish how the thermoelectric power goes to zero at $0^{o}K$.

The first stage in extending the galvanomagnetic analysis to a non-ellipsoidal Fermi surface is to perform a three-band fit to the arsenic data to accommodate the hole necks. This will add another five unknowns to equations (4.26) to give twelve equations in fourteen unknowns: to obtain a unique solution, two of these must be fixed. To extend to the general non-ellipsoidal case will probably be extremely difficult. Allgaier (1966) has made some first steps by substituting a non-ellipsoidal, non-parabolic function (Cohen 1961) into the tensor coefficient integrals (4.17,18,19) to explain the low-field Hall coefficient of tin telluride. The results are somewhat qualitative. To improve on the present quantitative fit to the arsenic data will be hard. Numerical evaluation of the integrals (4.17-19) fed with complete details of Lin and Falicov's model of the Fermi surface

might be possible. Additional experimental data could come from measurements of the higher order galvanomagnetic tensors.

Of more immediate interest is a fresh analysis of bismuth using the new method of computation. Previous experimental work has now been shown to be inaccurate due to the violation of the low-field condition $\mu H << 1$. To keep to second order effects in bismuth H must not exceed 100 gauss (Bate). A new look at the hole tilt angle and carrier density discrepancies of antimony might also be fruitful.

In general, the time now seems ripe for development that will lead to a new understanding of transport effects in semimetals.

REFERENCES

Abeles, B. and Meiboom, S. 1954, Phys.Rev., 95, 31.

Abeles, B. and Meiboom, S. 1956, Phys.Rev., 101, 544.

Allgaier, R.S. 1966, Phys.Rev., 152, 808.

Barrett, C.S. 1952, Structure of Metals (New York) p.337

Bate, R.T., private communication

Beer, A.C. 1963, Galvanomagnetic effects in semiconductors (Solid state physics : Seitz and Turnbull. Suppl.4)

Berlincourt, T.G. 1955, Phys.Rev., 99, 1716.

Blackman, L.C., Saunders, G., and Ubbelohde, A.R. 1961, Proc.Roy.Soc., A,264, 19.

Brice, J.C. 1965, (a), p.125, The growth of crystals from the melt. (Amsterdam, North-Holland)

Brice, J.C. 1965(b), p.125, The growth of crystals from the melt. (Amsterdam, North-Holland)

Brice, J.C. 1965(c) p.118, The growth of crystals from the melt. (Amsterdam, North-Holland).

Bridgman, P.W. 1932/33, Proc. Am. Acad. Sci., 68, 39.

Burton, W.K. Cabrera, N. and Frank, F.C. 1951, Phil.Trans., 243, 299.

Butler, J.F., Calawa, A.R. and Harman, T.C. 1966, Appl. Phys.Lett., 9, 427.

Calawa, A.R. Harman, T.C. Fin, N. and Youtz, P. 1968, Trans.Met.Soc.AIME, 242, 374.

Cohen, M.L. 1961, Phys.Rev. 121, 387.

Cohen, M.L. Falicov, L.M. and Golin, S. 1964, IBM J.Res.Dev. 8, 215.

Culbert, H. 1967, Phys.Rev. 157, 560.

Cusack, N. and Kendall, P. 1958, Proc.Phys.Soc. 72, 898.

Datars, W.R. and Vanderkooy, J. 1965, Bull.Am.Phys.Soc. 10, 110.

Datars, W.R. and Vanderkooy, J. 1966, J.Phys.Soc.Japan, 21, 657.

Dauphinee, T.M. and Mooser E. 1955, Rev.Sci.Instrm., 26, 660.

Debye, P.P. and Conwall, E.M. 1954, Phys.Rev., 93, 693.

Dickinson, J.R. 1958, Trans.E.I.C., 2, 157.

Donoghue, J.J. and Eatherley, W.P. 1951, Rev.Sci.Instrum., 22, 513.

Drabble, J.R. Groves, R.D. and Wolfe, R. 1958, Proc.Phys.Soc., 71 430.

Drabble, J.R. and Wolfe, R. 1956 Proc.Phys.Soc. B69, 1101.

Epstein, S. and Juretschke, H.J. 1963, Phys.Rev., 129, 1148.

Falicov, L.M. and Golin, S. 1965, Phys.Rev. 137, A871.

Falicov, L.M. and Lin, P.J. 1966, Phys.Rev., 141, 562.

Faulkner, E.A. McGlashan, M.L. and Stubley, D. 1965, J.Chem.Soc.PartII, 2837.

Faulkner, E.A. and Stannett, R.H.O. 1964, Elect.Engng. 36, 159.

Freedman, S.J. and Juretschke, H.J. 1961, Phys.Rev., 124, 1379.

Gallo, C.F. Chandrasekhar, B.S., and Sutter P.H. 1963, J.Appl.Phys. 34, 144.

Gautier, A. 1903, Compt.Rend., 135,1115.

Golin, S. 1965, Phys.Rev. 140, A993.

Goodman, C.H.L. 1966, J.Sci.Instrum., 43, 393.

Hampshire, D.W.H., and Petersen D. 1967, Elec. Engng., 39, 38.

Harman, T.C. Honig, J.M. and Tarmy, B.M. 1964, Adv.Ener. Conv., 5, 1.

Harman, T.C. Honig, J.M. and Jones, L. 1964, Adv. Ener. Conv., 5, 183.

Hawgood, J., 1965, Numerical methods in Algol, (London: McGraw-Hill) p.72.

Herring, C. 1955, Bell syst.tech.jour. 34, 237.

Herring, C. and Vogt, E. 1956, Phys.Rev., 101, 944.

Hutchinson, W.P. Pulsford, E.W. and White, A.G., 1954, J.Sci. Instrum. 31, 421.

Jewell, A.J. 1967, J.Sci.Instrum., 44, 81.

Johnson, J.F.W. 1855, The chemistry of common life (London) 2, 201.

Jones, H. 1936, Proc.Roy.Soc., A147, 653.

Jones, H. and Zener, C. 1934, Proc.Roy.Soc., A145, 268.

Juretschke, H.J. 1955, Acta Cryst. 8, 716.

Kapitza, P. 1929, Proc.Roy.Soc. A123, 292.

Keepin, G.R. 1950, J.Appl.Phys., 21, 260.

Ketterson, J.B. and Eckstein, Y. 1965, Phys.Rev., 140, A1355.

Krickorian, J.B. and Sneed, R.J. 1966, J.Appl.Phys., 37, 3665.

Lark-Horovitz, K. and Johnson V.A. 1959, Methods of experimental physics, 6 B p.159.

Lin, P.J. and Falicov, L.M. 1966, Phys.Rev., 142, 441.

Maltz, M. and Dresselhaus, M.S. 1968, Phys.Rev.Lett., 20, 919.

McLean, D. 1957, Grain boundaries in metals (Oxford: Clarendon P.)

McLennan, J.C. Niven, C.D. and Wilhelm, J.O. 1928, Phil.Mag., 6, 666.

Mellor, J.W. 1929, A comprehensive treatise on inorganic and theoretical chemistry., 9, 7.

Metz, E.P.A. Miller, R.C. and Magelsky, R. J.Appl.Phys. 33, 2016.

Miyamoto, N. and Nishizawa, J.I. 1967, Rev.Sci.Instrm., 38, 360.

Mott, N.F. and Jones, H. 1936, Theory of the properties of metals and alloys (Oxford : Clarendon Press) p.167.

Nancollas, G.H. and Hardy, J.A. 1967, J.Sci.Instrum. 45, 290.

Onsager, L. 1931, Phys.Rev., 38, 2265.

Oktu, O. 1967, Thesis : University of Durham.

Oktu, O. and Saunders, G.A. 1967, Proc.Phys.Soc., 91, 156.

Palmer, T.M. 1966, Electr.Engng. 38, 467.

Priestley, M.G. Windmiller, L.R. Ketterson, J.B. and Eckstein, Y. 1967, Phys.Rev., 154, 671.

Putley, E.H. 1960 (a), p.43, The Hall effect and related phenomena. (London : Butterworths)

Putley, E.H. 1960 (b), p.50, The Hall effect and related phenomena. (London : Butterworths).

Reid, W.T., 1941, Temperature, Its measurement and control in science and industry (New York : Reinhold) p.611.

Sagar, A. and Faust, J.W. 1967, J.Appl.Phys., 38, 482.

Saunders, G.A. and Lawson, A.W. 1965, J.Appl.Phys. 36, 1787.

Saunders, G.A. Miziumski, C., Cooper, G.S. and Lawson, A.W. 1965, J.Phys.Chem.Solids. 26, 1299.

Saunders, G.A. and Oktu, O. 1968, J.Phys.Chem.Solids, 29, 327.

Smith, R.A. 1959, Semiconductors, (Cambridge University Press) p.

Sonnenschein, F.L., 1869, Handbuch der gerichtlichen Chemi. (Berlin) p.212.

Stout, M.B. 1960, Basic electrical measurements (Prentice Hall), chap.7.

Sybert, J.R. Mackey, H.J. and Hathcox, K.L. 1968, Phys. Rev., 166, 710.

Tanaka, K. Suri, S.K. and Jain, A.L., 1968, Phys.Rev., 170, 664.

Taylor, J.B. Bennett, S.L. and Heyding, R.D. 1965, J.Phys.Chem.Solids., 26, 69.

Taylor, W.A. McCollum, D.C. Passenheim, B.C. and White, H.W. 1967, Phys.Rev., 161, 652.

Topping, J. 1962, Errors of observation and their treatment. (Inst. of Physics). p.102.

Vanderkooy, J. and Datars W.R 1967, Phys.Rev., 156, 571.

Vogel, F.L. Pfann W.G. Corey, H.E. and Thomas, E.E. 1953, Phys.Rev., 90, 489.

Volger, J. 1950, Phys.Rev., 79, 1023.

Weisberg, L.R. and Celmer, P.R. 1963, J.Electrochem.Soc. 110, 56.

Wernick, J.H. Hobstetter, J.N. Lovell, L.C. and Dorsi, D. 1958, J.Appl.Phys., 29, 1013.

White, G.K. 1953, Proc.Phys.Soc., A66, 559.

White, G.K. 1959, Experimental techniques in low-temperature physics (Oxford : Clarendon Press).chap.7.

Wilson, A.H. 1953, The Theory of Metals (London : Cambridge University Press), p.224.

Wilson, W. and Stone, N.W.B. 1957, J.Sci.Instrum., 34,327.

Windmiller, L.R. 1966, Phys.Rev., 149, 472.

Wood, L.A. 1932, Phys.Rev., 41, 231.

Woodhams, F.W.D. Carlow, J.S. and Meads, R.E. 1966, J.Sci.Instrum., 43, 333.

Wright, D.A. 1959, Elect.Engng. 31, 659.

Zabetakis, M.G. Craig, R.S., and Sterrett, K.F. 1957, Rev.Sci.Instrum., 28, 497.

Ziman, J.M. 1964, Principles of the theory of solids, (Cambridge University Press) p.179.

PUBLICATIONS

To date, the contents of this thesis are embodied in the following publications:

1. Single-crystal growth from the Vapour and etch pit studies in arsenic. A. P. Jeavons and G. A. Saunders, 1968, Brit J. Appl. Phys. (J.Phys.D), Ser.2, 1 869.
2. Correlation between the galvanomagnetic effects and the Fermi surface of arsenic. A.P. Jeavons and G. A. Saunders, 1968, Phys. Lett., 27A, 19.
3. The low field, magnetoresistivity tensor and the Fermi surface of arsenic, 1969, Proc. Roy. Soc., to be published.

A. P. Jeavons.
June 1969.

BRIT. J. APPL. PHYS. (J. PHYS. D), 1968, SER. 2, VOL. 1. PRINTED IN GREAT BRITAIN

Single-crystal growth from the vapour and etch pit studies in arsenic

A. P. JEAVONS and G. A. SAUNDERS

Department of Applied Physics, University of Durham

MS. received 13*th November* 1967, *in revised form* 18*th January* 1968

Abstract. Strain-free single crystals of the rhombohedral (α) semimetallic form of arsenic have been grown from the vapour. Large crystals can only be grown when the deposition temperature is above a critical value of about 700°C. Temperature fluctuations must be kept within 0·2 degC to prevent development of a severe mosaic structure. Dislocations have been examined by etching techniques. Either trigonal or hexagonal pits may be produced at the same site of emergence of dislocations on the (111) cleavage planes; the etch determines the pit shape.

1. Introduction

Single crystals of the rhombohedral semimetallic form of arsenic are required for measurements, now in progress, of the low-field magnetoresistivity tensor. Arsenic sublimes readily (triple point 817°C at 35 atm pressure); but small crystals only have previously been grown from the vapour phase (McLennon *et al.* 1928, Berlincourt 1955). Large strain-free crystals have now been obtained from the vapour above a critical temperature of about 700°C. Dislocation defects in these crystals have been detected and examined by etching techniques.

Crystals can be grown by the Bridgman technique from the melt in sealed, heavy walled quartz tubes (Weisberg and Celmer 1963, Saunders and Lawson 1965). But melt growth has disadvantages. Arsenic expands on freezing, and crystals tend to be strained. Only one crystallographic orientation usually results: the (111) plane parallel, or nearly so, to the crystal length. To withstand the pressure of 40 atm or more involved, the ratio of the inside diameter to the wall thickness of the containing quartz tube should be at least 2 : 1. A boule diameter of about 1 cm becomes a practical maximum. Ketterson and Eckstein (1965) have obtained larger crystals from the melt in a heavy walled quartz bomb with a conical growth region to prevent strain. But the manufacture of their container is highly specialized, and the cost prohibitive, particularly in view of its once-only use.

As an alternative technique, growth from the vapour has been investigated. The problem of strain is immediately overcome, and, if growth could be effected at temperatures 50 degC or more below the triple point, bigger crystals could be obtained using thinner walled quartz tubes at the considerably reduced vapour pressure (10 atm at 730°C) involved.

2. The critical temperature for arsenic single-crystal growth from the vapour

Preliminary studies were made of the effects of temperature on deposition of arsenic from the vapour. Ten gramme samples, sealed *in vacuo* in pointed quartz tubes, were lowered at 3 mm h^{-1} from a high-temperature plateau region in a furnace. Several runs were made; the plateau temperature was increased from 500°C to 750°C in steps of 50 degC. Initially, a polycrystalline boule of grain size about 1 mm^3 was obtained; lateral growth was incomplete. Grain size and lateral growth increased with temperature, the former to about 10 mm^3 at 650°C. At 700°C a sharp change to single-crystal growth took place. Lateral growth was now complete and crystal facets had formed at the tail.

The occurrence of a critical temperature for ordered growth is well known, for instance in metal crystals (Keepin 1950) and in pyrolytic graphite (Blackman *et al.* 1961), and for epitaxial deposition. Single-crystal growth upon a substrate will occur, if the freshly deposited atoms forming a monolayer are hot enough, and thus sufficiently mobile to migrate to surface kink sites before the next monolayer condenses (Burton *et al.* 1951).

Thus to form a single crystal at a given growth rate the substrate must attain a sufficiently high temperature. This simple model has been verified experimentally for the epitaxial deposition of germanium (Krikorian and Sneed 1966).

A reliable method for growing large single crystals from the vapour has been developed following the finding of a critical temperature.

3. The growth furnace and experimental details

The furnace used consists of a well-insulated mullite tube 70 cm long and 4 cm bore mounted vertically inside a rectangular Sindanyo box. Four independently controlled heater windings, of Kanthal wire, supplied from stabilized mains, ensure wide adjustment of temperature profile. Initially, crystals possessed a severe mosaic structure that proved to be due to thermal fluctuations during growth. Therefore, the mullite tube is lined with stainless steel to smooth any temperature undulations between the heater turns. 'Gouy' modulation is incorporated in a switching galvanometer controller, to stabilize temperature to within $\frac{1}{8}$ degC over long intervals. In this method the galvanometer pointer is pulsed from a multi-vibrator square-wave generator by about 5 degC about the mean temperature. Switching of the power to the furnace occurs each time the pointer passes the set temperature and proportional control ensues (see Goodman (1966) and Jewell (1967) for a detailed explanation). The reference junction of the sensing thermocouple is immersed in oil in a Dewar. Smooth lowering of the sample is effected through a support rod clamped to a platform driven down by three geared motor-rotated screw legs.

The quartz growth tube, illustrated in figure 1 (plate†), has the following dimensions: length 30 cm, internal diameter 2·0 cm and wall thickness 1·5 mm. A simple pointed end does not seed successfully because contact with the steel support rod destroys the temperature gradient at the tip, and several longitudinal crystals develop. To overcome this, a 2 cm length of 3 mm quartz rod is fused to the tip as a spacer, and the tube is constricted near the bottom for single seed selection. An 8 cm long blank with both ends closed, containing air at atmospheric pressure, is made from a quartz tube of close fit to the inside of the growth tube. Both growth tube and blank are cleaned for 3 hours with 1 : 1 HF/HNO_3, followed by concentrated HF, then distilled water and finally 'Analar' acetone. Baking for 24 hours at 900°C and 10^{-5} torr completes the cleaning. 50 g of 99·9995% purity arsenic followed by the blank are put in the tube. To distil off any oxide present, the tube is heated to 300°C under vacuum for 3 hours. The tube is then closed by sealing onto the blank.

The growth furnace temperature profile, shown in figure 2, has two major features, a hump and a plateau. The tube is sited with the tip just above the hump, so that the arsenic charge sublimes to the cooler upper part of the container, where it adheres to the glass.

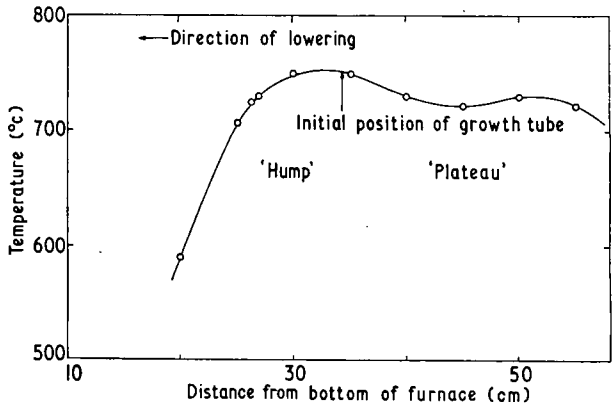

Figure 2. The growth furnace temperature profile.

† Plates at end of issue.

The bulk of the tube must be maintained at a fairly uniform temperature to disperse the charge and prevent the formation of a plug which can fracture the tube by expanding when it encounters the temperature maximum. Crystals grow by progressive condensation, as the tube cools on the lower side of the hump. The growth rate was 0·1 mm h^{-1}. A 50 g crystal, 2 cm in diameter and 5 cm long, may be grown in about seven days.

The resulting crystals show a perfect mirror cleavage on the (111) face, always parallel or nearly so, to the crystal length, as for melt crystals. X-ray photographs yield pin-point spots with no trace of spreading, asterism or splitting. Further studies, now discussed, have been made by etch pit techniques.

4. Dislocation etch pits in arsenic

Cleaved (111) faces of the crystals have been etched and examined microscopically. Etches were composed of different proportions of hydrofluoric, nitric and glacial acetic acids (see table). Pits of trigonal and hexagonal shape are found with overall densities averaging from 10^4 cm^{-2} in vapour grown to 10^5 cm^{-2} in melt grown crystals.

Details of etching and resultant pit shapes

Etch composition			Etch time	Pit shape
HF	HNO_3	CH_3COOH		
2	1	1 (etch A)	2 s	Trigonal
3	1	0 (etch B)	1 s	Truncated trigonal and round
4	1	0 (etch C)	1 s	Hexagonal

Straight lines, mutually orientated at 120°, are observed, see figure 3 (plate), along the [10$\bar{1}$] directions. Those which terminate do so (figure 4 (plate)) in an etch pit. Different patterns of lines appear on separated faces of a cleaved crystal. These are slip lines; slip occurs on cleaving. The primary slip system in arsenic comprises the (111) as glide plane and the [10$\bar{1}$] as slip directions and this system cannot give rise to slip lines on the (111) plane. The lines result from slip in the *xz* plane, a secondary glide plane. If the associated slip direction is the [111], then the etch pits at the ends of the slip lines would mark screw dislocations.

The etch pits are well defined; on further etching they enlarge whilst retaining their general shape and, except in a few cases, their number. Pits match on opposite cleaved faces. Also the etch pattern repeats with consecutive cleaving. Clearly the pits are sited at the points of emergence of dislocations on the (111) plane. Rows of closely spaced etch pits are observed in all crystals. By counting the line pit density at intersections and applying the method developed by Vogel *et al.* (1953) and extended to antimony by Wernick *et al.* (1958), these rows have been shown to indicate arrays of parallel edge dislocations defining low-angle grain boundaries.

Arsenic exhibits hexagonal as well as trigonal pits. The pit shape is characteristic of the etch used (see table); a trend (figure 5 (plate)) is extant from trigonal to hexagonal with increasing hydrofluoric acid concentration. To answer the question whether the different shaped pits arise at different sites, one-half of a cleaved crystal was etched to produce trigonal pits and the other to give hexagonal pits. With very few exceptions the pit patterns were identical. Every dislocation can produce both types of pits; the etch is the determining factor. Both kinds of pits are pyramidal and have edges parallel to the [10$\bar{1}$] directions. But hexagonal pits have a stepped internal structure, while trigonal pits are smooth. Many pits are symmetrical; the dislocations are parallel to the [111] axis. The existence of dislocations at a very acute angle to the cleavage plane is indicated by some highly antisymmetric pits (figure 6 (plate)). Shallow grooves, like those shown in figure 4, suggest networks of dislocations actually in the cleavage plane.

That both trigonal and hexagonal pits can be produced in arsenic probably results from its lamellar crystal structure. Each atom has three nearest neighbours at 2·51 Å (the short

bond) and three others at 3·15 Å (the long bond) which reflects as a pairing of layers. Each pair can be considered as one puckered hexagonal layer. Removal of these hexagonal layers will produce hexagonal etch pits. But, if the layers are attacked singly, in the normal way, trigonal pits will result since the [111] axis has $\bar{3}$ symmetry. For bismuth and antimony, which are closer to cubic in structure (the rhombohedral angle α being 57° 14′ and 57° 7′ respectively) than arsenic ($\alpha = 54° 10'$), the long and short bonds are almost equal, and only trigonal pits are observed. In bismuth telluride ($\alpha = 24° 10'$) both types of pits are found (Sagar and Faust 1967).

Acknowledgments

The authors would like to thank Mr. R. I. Cottam for assistance in the etching studies.

References

BERLINCOURT, T. G., 1955, *Phys. Rev.*, **99**, 1716.
BLACKMAN, L. C., SAUNDERS, G., and UBBELOHDE, A. R., 1961, *Proc. Roy. Soc.* A, **264**, 19.
BURTON, W. K., CABRERA, N., and FRANK, F. C., 1951, *Phil. Trans.*, **243**, 299.
GOODMAN, C. H. L., 1966, *J. Sci. Instrum.*, **43**, 393.
JEWELL, A. J., 1967, *J. Sci. Instrum.*, **44**, 81.
KEEPIN, G. R., 1950, *J. Appl. Phys.*, **21**, 260.
KETTERSON, J. B., and ECKSTEIN, Y., 1965, *Phys. Rev.*, **140**, 1355.
KRIKORIAN, E., and SNEED, R. J., 1966, *J. Appl. Phys.*, **37**, 3665.
MCLENNAN, J. C., NIVEN, C. D., and WILHELM, J. O., 1928, *Phil. Mag.*, **6**, 666.
SAGAR, A., and FAUST, J. W., 1967, *J. Appl. Phys.*, **38**, 482.
SAUNDERS, G. A., and LAWSON, A. W., 1965, *J. Appl. Phys.*, **36**, 1787.
VOGEL, F. L., PFANN, W. G., COREY, H. E., and THOMAS, E. E., 1953, *Phys. Rev.*, **90**, 489.
WEISBERG, L. R., and CELMER, P. R., 1963, *J. Electrochem. Soc.*, **110**, 56.
WERNICK, J. H., HOBSTETTER, J. N., LOVELL, L. C., and DORSI, D., 1958, *J. Appl. Phys.*, **29**, 1013.

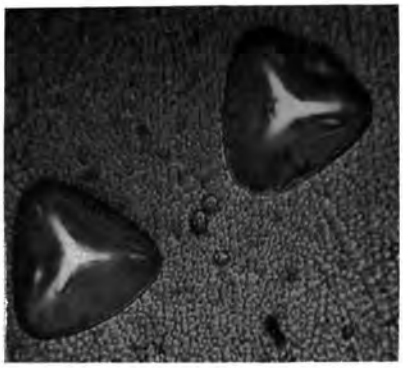

(*a*)

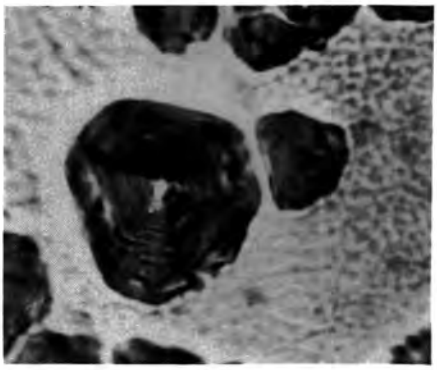

(*b*)

(*c*)

Figure 5. (*a*) Trigonal pits (etch A, see table) (× 500). (*b*) A truncated pit (etch B) (× 500). (*c*) Hexagonal pits (etch C) (× 500).

Figure 6. Etch pits produced from dislocations directed at an acute angle to the surface (etch A) (× 500).

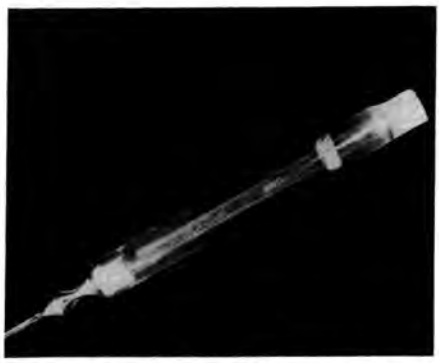

Figure 1. The quartz growth tube.

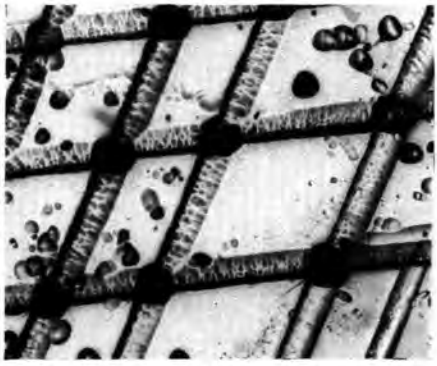

Figure 3. Duplex slip on the (111) cleavage face. The scarp and dip topography arises from etching at the surface steps (× 500).

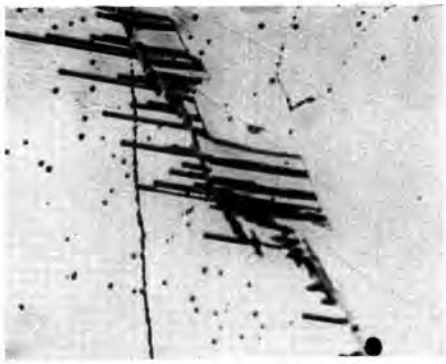

Figure 4. Slip lines on the (111) face, terminating in etch pits. The network of faint lines is considered to mark dislocations lying in the (111) plane (× 50).

Reprinted from

PHYSICS LETTERS

Volume 27A, number 1, 20 May 1968

CORRELATION BETWEEN THE GALVANOMAGNETIC EFFECTS AND THE FERMI SURFACE OF ARSENIC

A. P. JEAVONS and G. A. SAUNDERS

pp. 19–20

NORTH-HOLLAND PUBLISHING COMPANY

AMSTERDAM

CORRELATION BETWEEN THE GALVANOMAGNETIC EFFECTS AND THE FERMI SURFACE OF ARSENIC

A. P. JEAVONS and G. A. SAUNDERS
Department of Applied Physics, The University of Durham, UK

Received 23 April 1968

Magnetoresistivity tensor data in arsenic are analysed using a two carrier, multivalley, ellipsoidal band model. Results agree reasonably with a recent theoretical determination of the Fermi surface. Discrepancies probably arise from the non-ellipsoidal nature of the hole surface.

Pseudopotential band structure calculations for arsenic predict that the electrons occupy three nearly ellipsoidal pockets and the holes a "crown" comprising six pockets connected by six small necks [1]. Recent measurements of the De Haas-Van Alphen effect are consistent with this model [2]. Here we show that the galvanomagnetic effects in arsenic can be interpreted using a more simple form of the Fermi surface: three tilted electron ellipsoids and six tilted hole ellipsoids.

Measurements, at temperatures between 77°K and 305°K, of all twelve components of the magnetoresistivity tensor to second order in magnetic field are now complete on single crystal samples of arsenic grown from the vapour phase [3]. The theoretical basis of the work can be found in a previous paper concerning antimony [4]. But the method of computation is quite different; a least squares fit of the measured components has been obtained using an IBM 360/67 computer. A set of nine parameters - the electron (μ_1, μ_2, and μ_3) and hole (ν_1, ν_2, and ν_3) mobilities along the ellipsoid axes, the tilt angles (ψ_e and ψ_h) of the major axis away from the trigonal axis and the carrier density (N) in each band - is chosen as a trial solution. The twelve magnetoconductivity tensor components are then

Table 1

Magnetoresistivity components	ρ_{11}	ρ_{33}	$-R_{231}$	$-R_{123}$	A_{13}	A_{31}	$-A_{44}$	A_{11}	A_{12}	A_{33}	A_{24}	A_{42}
	($\mu\Omega$cm)		($10^{-2}\mu\Omega$cm/kG)		($10^{-4}\mu\Omega$cm/kG^2)							
Measured values	26.8	34.1	2.08	11.5	9.7	8.2	1.9	2.5	5.5	5.8	1.8	1.0
Magnetoconductivity components	σ_{11}	σ_{33}	$-P_{231}$	$-P_{123}$	B_{13}	B_{31}	$-B_{44}$	B_{11}	B_{12}	B_{33}	B_{24}	B_{42}
	($10^4\Omega^{-1}$cm^{-1})		(Ω^{-1}cm^{-1}kG^{-1})		(Ω^{-1}cm^{-1}kG^{-2})							
Measured values	3.75	2.93	22.8	160	2.04	0.72	0.24	0.35	0.78	0.50	0.25	0.10
Calculated: Electron part	1.89	1.88	-47.4	-8.5	0.021	0.257	0.023	0.043	0.161	0.008	0.011	0.014
Hole part	2.82	1.06	+70.0	+175	1.43	0.214	0.268	0.317	0.687	0.401	0.258	0.090
Total	3.71	2.94	+22.5	+167	1.45	0.47	0.29	0.36	0.85	0.41	0.27	0.10
Ratio: $\frac{\text{Cal.comp.}}{\text{Meas.comp.}}$	0.99	1.00	0.99	1.04	0.71	0.66	1.21	1.03	1.08	0.82	1.07	1.05

Solution:	N	μ_1	μ_2	μ_3	ψ_e	ν_1	ν_2	ν_3	ψ_h
	(cm^{-3})	(cm^2/volt sec)				(cm^2/volt sec)			
	2.16×10^{20}	460	40	550	82°	1210	50	680	40°

Table 2

	Tilt angle		
	Electron pockets (minimum area)	Electron pockets (maximum area)	Hole pockets (minimum area)
Pseudopotential calculation [1]	80°	171°	44°
De Haas-Van Alphen effect [2]	86°	171°	37°
Galvanomagnetic effects (this work)	82°	172°	40°

Electron effective mass ratios, in ellipsoidal approximation, from ref. 2

$$m_1 : m_2 : m_3 = 1.5 : 20 : 1 .$$

Inverse electron mobility ratios (this work)

$$1/\mu_1 : 1/\mu_2 : 1/\mu_3 = 1.2 : 14 : 1 .$$

	Carrier density (cm^{-3})
De Haas-Van Alphen effect	2.12×10^{20} (at 4.2 °K)
This work	2.16×10^{20} (at 305°K)

calculated, compared to the measured components and the trial solution is altered systematically until a "best fit" is obtained. Full results at 305°K are presented in table 1.

The Fermi surface parameters so obtained are compared with previous work in table 2. In view of the simplifications made, agreement is surprisingly good. We confirm the theoretical assignment [1] of electrons to the high-tilt and holes to the low-tilt pockets. The similarity between electron effective mass ratios and inverse mobility ratios indicates an approximately isotropic relaxation time. Discrepancies exist for B_{13}, B_{31}, B_{44} and B_{33} (see table 1). Plausibly this reflects the departure of the Fermi surface shape from ellipsoidal, in particular the existence of the necks, which contain a small number of highly mobile holes. A significant contribution to the B_{ij} could result, as these components depend upon the cube of the mobility.

References

1. P.J. Lin and L.M. Falicov, Phys. Rev. 142 (1966) 441.
2. M.G. Priestley, L.R. Windmiller, J.B. Ketterson and Y. Eckstein, Phys. Rev. 154 (1967) 671.
3. A.P. Jeavons and G.A. Saunders, Brit. Appl. Phys. to be published.
4. Ö. Öktü and G.A. Saunders, Proc. Phys. Soc. 91 (1967) 156.

* * * * *

ROYAL SOCIETY—PROCEEDINGS—A.

~~Proof for correction and return to Royal Society.~~

Proof to be retained by the Authors.

Not to be communicated to any Journal for publication.

PROOF COPY

The low field, magnetoresistivity tensor and the Fermi surface of arsenic

By A. P. Jeavons† and G. A. Saunders

Department of Applied Physics, The University of Durham

(*Communicated by A. R. Ubbelohde, F.R.S.—Received 7 October* 1968)

Measurements are presented, at selected temperatures between 305 and 77 °K, of the twelve coefficients that define the low-field magnetoresistivity tensor of arsenic. A two-carrier multivalley ellipsoidal model of the energy bands is invoked to determine carrier densities and mobilities and tilt angles of the Fermi ellipsoids. In agreement with recent theoretical calculations and measurements of the de Haas–van Alphen effect, the electrons are sited in pockets tilted at $+82°$ to the trigonal axis and holes in pockets tilted at $+40°$. Equal carrier densities are essentially temperature independent, ranging from $1{\cdot}9 \times 10^{20}$ cm^{-3} at 77 °K to $2{\cdot}1 \times 10^{20}$ cm^{-3} at 305 °K. Carrier mobility temperature dependences are close to $T^{-1{\cdot}7}$, considerably greater than the expected $T^{-1{\cdot}0}$, probably owing to intervalley scattering. Experimental techniques and a new method of computation are described.

1. Introduction

The group *V* elements arsenic, antimony and bismuth are semimetals in consequence of an energy band overlap. Carrier transport is characterized by high mobilities and long relaxation times; the semimetals are most suitable for experimental studies of band structure and for testing new aspects of electron transport theory. In bismuth the carriers are particularly mobile and transport effects are dramatic: the findings of a large, field dependent Hall coefficient and of oscillations in the magnetic susceptibility (de Haas–van Alphen effect) at helium temperatures were signposts to earlier explorers of solid state physics. Galvanomagnetic effects in these materials are markedly anisotropic and have been quantitatively interpreted only by invoking a multivalley model of the ellipsoidal energy bands (Abeles & Meiboom 1956; Freedman & Juretschke 1961; Epstein & Juretschke 1963). Recently, attention has been concentrated on antimony. Its Fermi surface has been determined both experimentally (Windmiller 1966) and theoretically (Falicov & Lin 1966); the galvanomagnetic effects, studied over a wide temperature range (Öktü & Saunders 1967), fit the predicted model.

Here a detailed study of the galvanomagnetic effects in the remaining element, arsenic, is presented. Previous information is sparse: the resistivity temperature dependence (McLennan, Niven & Wilhelm 1928) and the anisotropy of resistivity (Bridgman 1965; Taylor, Bennett & Heyding 1965) have been measured; magnetoresistance, first looked at by Kapitza (1929), has now been examined at helium temperatures (Sybert, Mackay & Hathcox 1968).

Because the galvanomagnetic effects in arsenic are small, their measurement has required considerable experimental refinements, which are described here in detail.

† Now at: Cavendish Laboratory, Cambridge.

An improved method of computation of band and mobility parameters is also reported. But first, the nature of the Fermi surface is discussed.

2. Crystal structure and Fermi surface of arsenic

Of the three allotropic forms of arsenic the α-form crystallizes, like bismuth and antimony, in the rhombohedral, $A7$ structure of point group $\bar{3}m$ with two atoms per unit cell. The symmetry elements of this structure comprise three diad (x) axes normal to three mirror planes, mutually orientated at 120°, which intersect in an inversion triad (z) axis. Bisectrix (y) axes, one in each mirror plane, complete three orthogonal (x, y, z) sets. An alternative nomenclature is 1, 2 and 3 for x, y and z respectively.

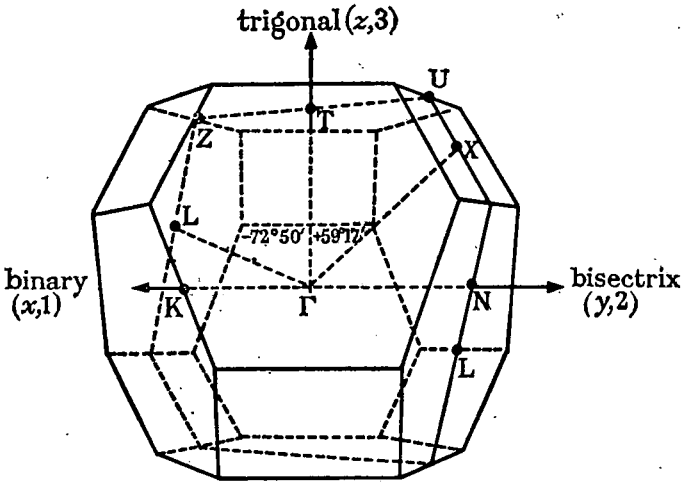

Figure 1. The first Brillouin zone of the arsenic lattice. The three axes binary, bisectrix and trigonal form a right-handed orthogonal set; the positive sense of rotation is towards X in the first y–z quadrant.

Figure 1 illustrates the Brillouin zone; symmetry points and one binary–bisectrix–trigonal system are labelled. It is important to note that these reference axes may be chosen in two ways: either the centre (X) of a rectangular face of the centre (L) of an irregular hexagonal face may lie in the first y–z quadrant. We follow the convention adopted by Windmiller (1966): the axes are chosen as a right-handed set with X in the first y–z quadrant. Then ΓX is at $+59°\,17'$ from ΓT and rotations towards ΓL are negative.

Considerations of crystal chemistry (Cohen, Falicov & Golin 1964) show that the $A7$ structure causes a small overlap of the fifth and sixth energy bands and semimetallic behaviour results with equal populations of electrons and holes. Detailed calculations are now available (Falicov & Golin 1965; Golin 1965; Lin & Falicov 1966). These accord with the results of quantum resonance experiments: the de Haas–van Alphen effect (Berlincourt 1955; Priestley, Windmiller, Ketterson &

Eckstein 1967), cyclotron resonance (Datars & Vanderkooy 1966) and ultrasonic attenuation (Ketterson & Eckstein 1965); the essential features of the Fermi surface are established. There are three electron pockets centred on each L point in the Brillouin zone and a multiply-connected hole surface around T. Each electron pocket can be considered as a prolate ellipsoid. One principal axis is parallel to the binary direction and the other two lie in the mirror plane (TZLNXUΓ). One of these is the longest axis; it is tilted away from the trigonal axis ΓT by approximately $+80°$. The hole surface, called a 'crown' (figure 2) may be thought of as six carrot-shaped pockets joined by six thin cylinders or 'necks'. Each pocket is bisected by the mirror plane and is tilted by about $+40°$ away from the trigonal axis.

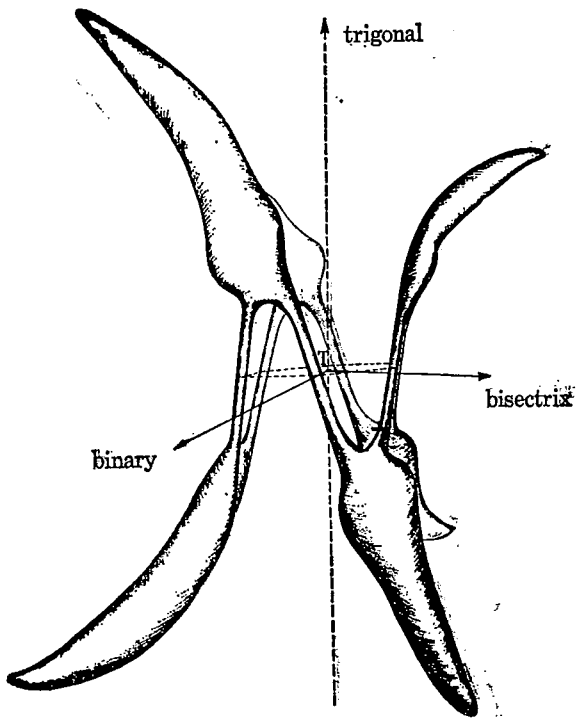

FIGURE 2. The hole surface or 'crown' of arsenic. It is centred on the T point of the Brillouin zone (after Lin & Falicov 1966).

Reported here are systematic measurements, made at selected temperatures between 77 and 305 °K, of the coefficients that define the isothermal magneto-resistivity tensor to second order in magnetic field. To a first approximation, the data are interpreted on the basis of a simplified form of the Fermi surface: three electron and six hole ellipsoids. There were two objectives: to determine the important carrier properties—density and mobility—as a function of temperature and to test agreement between the simplified ellipsoidal model and Lin and Falicov's model of the Fermi surface.

3. Experimental design

The orthogonal set of axes binary–bisectrix–trigonal (1–2–3) forms a most convenient Cartesian reference system for the generalized form of Ohm's law that relates the current density **J** to the electric field **E** in an anisotropic medium in a magnetic field **H**:

$$\left.\begin{aligned} E_1 &= \rho_{11}(\mathbf{H})\,J_1+\rho_{12}(\mathbf{H})\,J_2+\rho_{13}(\mathbf{H})\,J_3,\\ E_2 &= \rho_{21}(\mathbf{H})\,J_1+\rho_{22}(\mathbf{H})\,J_2+\rho_{23}(\mathbf{H})\,J_3,\\ E_3 &= \rho_{31}(\mathbf{H})\,J_1+\rho_{32}(\mathbf{H})\,J_2+\rho_{33}(\mathbf{H})\,J_3,\\ \text{i.e.}\quad E_i &= \rho_{ij}(\mathbf{H})\,J_j \quad\text{or}\quad J_i=\sigma_{ij}(\mathbf{H})\,E_j, \end{aligned}\right\} \tag{1}$$

where $\rho_{ij}(\mathbf{H})$ is the magnetoresistivity tensor and $\sigma_{ij}(\mathbf{H})$, its inverse, the magnetoconductivity tensor.

Transport phenomena are expressed by the Boltzmann equation; Jones & Zener (1934) showed that a solution in the form of a power series in **H** is valid. If $\mu H \ll 1$ (μ is the carrier mobility), convergence is rapid and only terms to H^2 are required to explain the galvanomagnetic effects. Accordingly, $\rho_{ij}(\mathbf{H})$ is defined as follows:

$$\rho_{ij}(\mathbf{H}) = \rho_{ij}+R_{ijk}H_k+A_{ijkl}H_kH_l.$$

Juretschke (1955) has shown by use of the Onsager relation, $\rho_{ij}(\mathbf{H}) = \rho_{ji}(-\mathbf{H})$, and point group symmetry that, for the $A7$ structure, the nine components of $\rho_{ij}(\mathbf{H})$ can be defined by twelve independent coefficients: two resistivity coefficients ρ_{11} and ρ_{33}, two Hall coefficients R_{231} and R_{123}, actually the negatives of the conventionally defined Hall coefficients, and eight magnetoresistance coefficients A_{1111} (short notation A_{11}), A_{1122} (A_{12}), A_{1133} (A_{13}), A_{3311} (A_{31}), A_{2323} (A_{44}), A_{2223} (A_{24}), A_{3333} (A_{33}) and A_{2322} (A_{42}).

The definitions are

$$\left.\begin{aligned} \rho_{11}(\mathbf{H}) &= \rho_{11}+A_{11}H_1^2+A_{12}H_2^2+A_{13}H_3^2-2A_{24}H_2H_3,\\ \rho_{22}(\mathbf{H}) &= \rho_{11}+A_{12}H_1^2+A_{11}H_2^2+A_{13}H_3^2+2A_{24}H_2H_3,\\ \rho_{33}(\mathbf{H}) &= \rho_{33}+A_{31}H_1^2+A_{31}H_2^2+A_{33}H_3^2,\\ \rho_{23}(\mathbf{H}) &= R_{231}H_1-A_{42}H_1^2+A_{42}H_2^2+2A_{44}H_2H_3,\\ \rho_{31}(\mathbf{H}) &= R_{231}H_2+2A_{44}H_3H_1-2A_{42}H_1H_2,\\ \rho_{12}(\mathbf{H}) &= R_{123}H_3-2A_{24}H_3H_1+(A_{11}-A_{12})\,H_1H_2, \end{aligned}\right\} \tag{2}$$

$\rho_{32}(\mathbf{H})$, $\rho_{13}(\mathbf{H})$, and $\rho_{21}(\mathbf{H})$ follow since $\rho_{ij}(\mathbf{H}) = \rho_{ji}(-\mathbf{H})$.

The twelve coefficients may be determined experimentally by orientating suitable samples in a magnetic field so that only one or two coefficients contribute to each measurement. As an example, consider the configuration shown in figure 3. **J** is in the binary (1) direction and (**H**) is in the trigonal (3) direction. The probes measure only E_1. Therefore

$$J_1 = J;\quad J_2 = J_3 = 0.$$
$$H_3 = H;\quad H_1 = H_2 = 0.$$
$$E_1 = E.$$

Thus, from (1) $$E = \rho_{11}(\mathbf{H})J.$$

$\rho_{11}(\mathbf{H})$ comes from (2)

$$\rho_{11}(\mathbf{H}) = \rho_{11} + A_{13}H^2.$$

Hence $$E_1 = (\rho_{11} + A_{13}H^2)J \quad \text{or} \quad E/J = A_{13}H^2 + \rho_{11},$$

and a graphical plot of E/J against H^2 has a gradient A_{13} and an intercept ρ_{11}. All coefficients have been measured at six temperatures between 77 and 305 °K on three samples. Overlap occurs; some coefficients could be measured in two ways on the same sample and most were remeasured on samples of other orientations. For further detail see Epstein & Juretschke (1963).

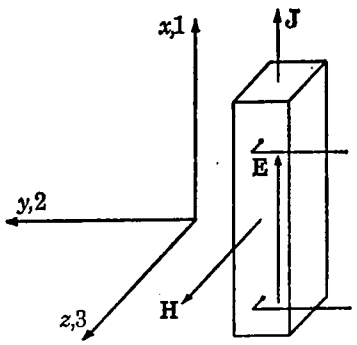

FIGURE 3. An illustration of sample orientation and field alinements used to measure ρ_{11} and A_{13}.

4. SAMPLE PREPARATION AND EXPERIMENTAL APPARATUS

Single crystals of arsenic were grown from 99·9995% pure material from the vapour phase (Jeavons & Saunders 1968). Crystal perfection was good; back reflexion Laue photographs exhibited pin-point spots evidencing unstrained material which is difficult to obtain from the melt. Dislocation etch pit density was about $10^4\,\mathrm{cm}^{-2}$ on the (111) (x–y) plane. Rectangular bar samples ($2 \times 0{\cdot}2 \times 0{\cdot}2$ cm) were spark cut from crystals orientated by reference to the (111) cleavage plane and the slip lines thereon that mark the three binary axes. Considerable care was necessary when cutting to prevent fracture or cracking due to the strong (111) cleavage; it was found essential to avoid cutting in the trigonal direction. Voltage probes were of 0·002 in. diameter copper wire soldered to the sample with a low-melting point (95 °C) alloy (32% Pb + 16% Sn + 52% Bi) and positioned well away from the sample ends to minimize Hall field shorting; contact diameter was about 0·01 in. To detect any longitudinal thermal gradient, copper-constantan thermocouples were soldered to each end. The sample was mounted rigidly, on an alinement mechanism, at one end only to prevent sample damage due to contraction on cooling. All wires to the sample were run inside a vertical, 0·5 in. diameter, german silver tube that supported the copper sample holder inside the cryostat: a stainless-steel Dewar vessel inside a pyrex glass tail Dewar vessel. To facilitate

isothermal conditions, for measurements at 305 °K the metal Dewar contained industrial paraffin, and the glass Dewar vessel ice/water. At lower temperatures the ice/water was replaced by liquid nitrogen and the paraffin by isopentane, liquid down to 113 °K. The non-flammable, five-component eutectic mixture used by Öktü & Saunders (1967) was not used owing to its appreciable electrical conductivity.

Preliminary measurements had shown that the galvanomagnetic effects in arsenic are an order of magnitude smaller than in antimony; room temperature magnetoresistance is about 0·05 % kG^{-2}. Therefore to measure the coefficients to an accuracy of 1 % requires a system with a resolution of 5 parts in 10^6 and thus a drift stability of approximately 1 in 10^6. At room temperature the resistivity of arsenic is such that a primary current of 5 A through the sample produced some 3 mV between the probes; the necessary resolution is equivalent to 15 nV and the noise level to 3 nV. To satisfy these stringent conditions, several important refinements, now described, were incorporated into the measuring system, basically a d.c. potentiometer.

The preamplifier-galvanometer detector usually used with the high precision decade potentiometer proved unsatisfactory for measuring at the nanovolt level and an electronic millimicrovoltmeter (Keithley type 149) modified to chop at 120 Hz instead of 100 Hz (twice mains frequency), to overcome mains pick-up interference, was used instead. Careful screening and layout of instruments to avoid hum-loops was imperative. Stray thermal e.m.f.s were limited by carefully cleaning all copper connexions and using 'low-thermal' solder (70 % Cd + 30 % Sn) wherever soldering was absolutely necessary; certain tap-key connexions inside the potentiometer were shorted with copper wire. The rheostat used to balance out the *IR* drop for Hall measurements was made from copper wire and submerged in a small oil bath. Usually, primary current stability is achieved by separate monitoring and manual control. This method proved impractical in this case and a transistorized current stabiliser (Palmer 1966) immersed in an oil bath, was used. A second, similar controller regulated the potentiometer current supply.

The only other problem was that of sample temperature stability. From temperature variations a voltage drift can appear from two sources: the Seebeck effect ($\sim 10\ \mu V/°K$ at room temperature) and the bulk resistance change (the temperature coefficient is 0·45 % $°K^{-1}$). On both counts it transpires that a temperature regulation to within 0·0001 °K is prerequisite to achieve the overall stability of 1 in 10^6. The work on antimony (Öktü & Saunders 1967) required stabilization to 0·05 °C, obtained by setting the metal Dewar interspace pressure and then balancing the heat leak by manual adjustment of electrical heating, a time consuming operation and impractical to the fine limit required for the present work. Therefore a system of automatic control of electrical heating (Jeavons & Saunders unpublished), a development of a temperature measuring system due to Faulkner, McGlashan & Stubley (1965), was devised. Figure 4 shows a block diagram of the electronic apparatus; operation is straightforward. The copper-resistance thermometer in the cryostat senses any temperature change and produces an out-of-balance signal from

the a.c. Wheatstone bridge. This is amplified, passed through a phase-sensitive detector and power amplified (d.c.) to feed back to the heater in the cryostat. The liquid surrounding the sample was not stirred; convection currents proved sufficient to give the required stability after a few hours equilibration time.

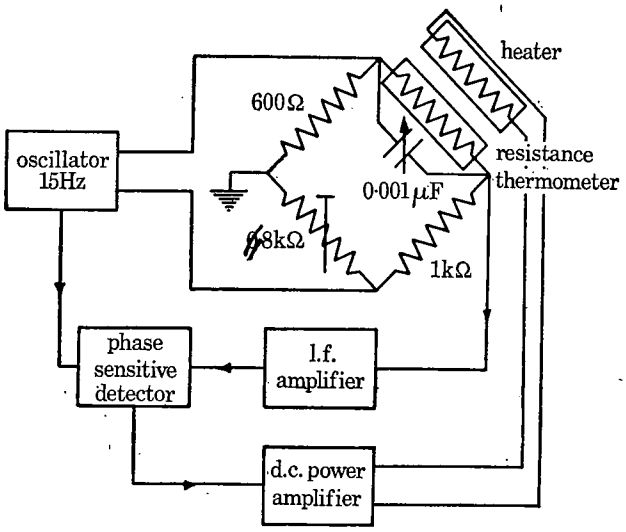

Should be 8kΩ

FIGURE 4. A block diagram of the system of automatic temperature control.

5. MEASUREMENT TECHNIQUE

The standard procedure of reversing the primary current was not used because of interference from the Peltier effect arising from the use of a large primary current (5 A) for this relatively highly conductive semimetal. The required galvanomagnetic voltages are proportional to current; it is necessary to eliminate error voltages independent of current. These arise from Seebeck voltages due to standing temperature gradients in the sample and contact potentials in the sample or measuring circuit; usually they are removed by reversing the current and averaging. However, in this work we found that a temperature gradient could appear along the sample due to Peltier heat being absorbed at one current contact and emitted at the other. Since the Peltier effect is proportional to current, reversing the current reverses this temperature gradient; the error voltage is an intimate part of the ohmic voltage and cannot be averaged away. To overcome this a trick was adopted: the sample being mounted at one end only, heat transference from this end was better than from the other and, coupled with Joule heating in the sample, was used to produce a temperature gradient that opposed the Peltier gradient. Isothermal conditions could be attained by adjusting the current to obtain a balance between these two effects. Fortunately the optimum current value was also acceptable from considerations of sensitivity and practicability.

Magnetic field reversal was employed to remove error voltages due to inexact probe positioning on the sample and to separate Hall and magnetoresistance

coefficients. The magnet was calibrated initially by nuclear magnetic resonance and subsequently a systematic procedure was used to avoid hysteresis errors. Sample alinement in the magnetic field was achieved mechanically by reference to the plane pole-tip faces. The magnet, not the sample, was rotated to establish the various orientations.

It was hoped that automatic plotting of galvanomagnetic potentials against magnetic field on an X–Y recorder would be possible. But it was not; even at a slow sweep rate of five minutes per kilogauss, the steadily increasing magnetic field induced a direct voltage of 0·1 μV via the loop area enclosed by the probe leads. Point by point plotting at static magnetic fields was necessary; the stability of the equipment enabled a field range of 0·7 to 4·7 kG in twelve steps to be covered without the need to restandardize the potentiometer.

6. Experimental results

Figure 5 shows graphical plots that determine R_{123}, R_{231}, A_{12} and A_{13} at the temperature 250 °K. The graphs demonstrate two important points: (*a*) the straight line plot indicates that the low-field condition $\mu H \ll 1$ is not violated up to 8 kG, and (*b*) drift is within the desired limit of 15 nV. Accurate values of all the magnetoresistivity coefficients were obtained from a least-mean-squares fit to the measurements by a computer; the values averaged over the three samples are presented in table 1. Marked anisotropy is evident; in particular the two Hall coefficients are in the ratio 1:5·5 at all temperatures, except at 77 °K where R_{231} decreases. The five coefficients A_{11}, A_{12}, A_{13}, A_{31} and A_{33} are all positive; A_{44} is negative. A_{42} and A_{24} are both positive or both negative depending on the choice of reference axes. For the particular system defined in §2 they are negative. The errors quoted in table 1 arise partly from the measurement of sample dimensions and partly from the galvanomagnetic-voltage measurement. The only other coefficient values available for comparison are those of ρ_{11} and ρ_{33} at 293 °K (Taylor *et al.* 1965). Agreement is close for ρ_{11}; the values of ρ_{33} differ by 10% (table 2).

Table 1. The measured values of the twelve magnetoresistivity coefficients of arsenic

temp. (°K)	resistivity ρ_{11}	resistivity ρ_{33}	Hall $-R_{231}$	Hall $-R_{123}$	magnetoresistivity A_{13}	A_{31}	$-A_{44}$	A_{11}	A_{12}	A_{33}	$-A_{24}$	$-A_{42}$
305	26·8	34·1	2·08	11·5	9·7	8·2	1·9	2·5	5·5	5·8	1·8	1·0
250	21·0	26·2	2·35	12·5	13·8	11·3	2·6	3·5	8·1	7·8	2·2	1·3
215	16·8	20·5	2·55	13·1	18·4	13·7	3·2	4·8	11·0	9·2	2·8	1·6
175	12·9	15·2	2·66	13·7	25·0	18·8	4·5	6·7	15·0	12·7	4·1	2·2
125	8·0	9·2	2·63	14·4	42	31	7·7	11·8	27	20·0	6·0	3·9
77	3·63	3·95	1·88	14·7	81	66	17	26	63	40	11·5	8·1
approx. error (%)	3	3	5	5	5	5	15	5	5	5	15	15

Units: resistivity, 10^{-6} Ω cm; Hall, 10^{-8} Ω cm kG^{-1}; magnetoresistivity, 10^{-10} Ω cm kG^{-2}.

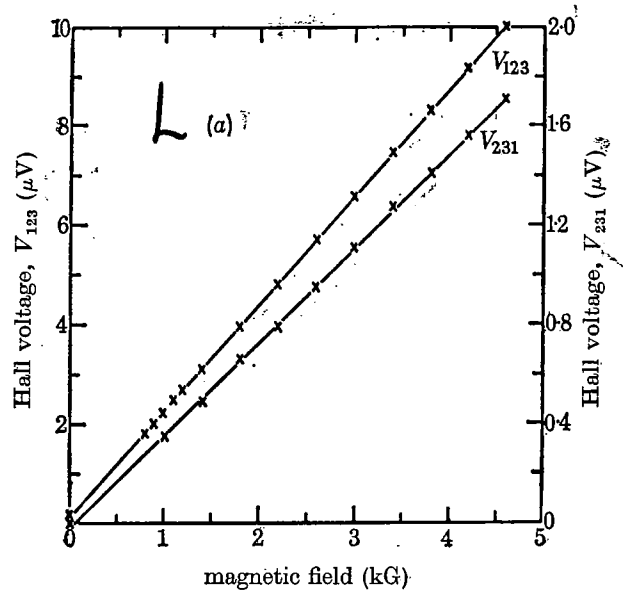

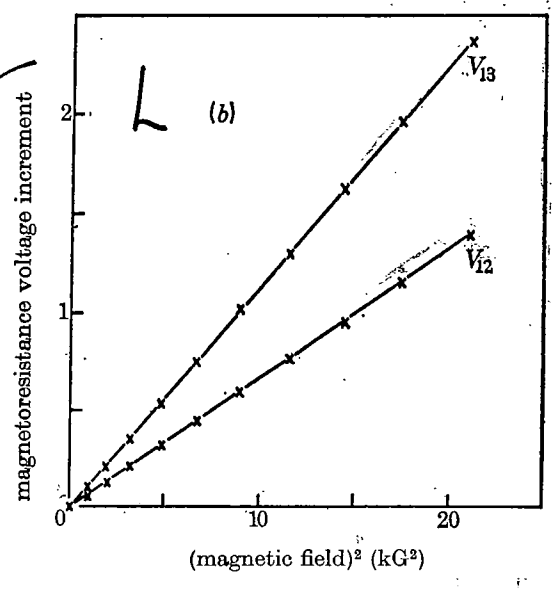

FIGURE 5(*a*). The magnetic field dependence of V_{123} and V_{231}. V_{123} and V_{231} are directly proportional to R_{123} and R_{231}. (*b*) The magnetic field dependence of V_{13} and V_{12}. V_{13} and V_{12} are directly proportional to A_{13} and A_{12}.

TABLE 2. A COMPARISON OF MEASUREMENTS OF ρ_{11} AND ρ_{33} AT 293 °K

	ρ_{11}	ρ_{33}
	($\mu\Omega$ cm)	
this work	25·2 (3 %)	32·1 (3 %)
Taylor *et al.* (1965)	25·5 ± 0·5	35·6 ± 1·9

While the magnetoresistivity tensor is measured experimentally, theory is more conveniently handled in terms of the magnetoconductivity tensor. Juretschke (1955) has derived the formulae that transform from one tensor to the other. There are twelve magnetoconductivity coefficients; each is directly related to corresponding magnetoresistivity coefficients:

$$\left.\begin{aligned}
\sigma_{11} &= \frac{1}{\rho_{11}}, & \sigma_{33} &= \frac{1}{\rho_{33}},\\
P_{123} &= \frac{R_{123}}{\rho_{11}^2}, & P_{231} &= \frac{R_{231}}{\rho_{11}\rho_{33}},\\
B_{11} &= \frac{A_{11}}{\rho_{11}^2}, & B_{33} &= \frac{A_{33}}{\rho_{33}^2},\\
B_{24} &= \frac{A_{24}}{\rho_{11}^2}, & B_{42} &= \frac{A_{42}}{\rho_{11}\rho_{33}},\\
B_{12} &= \frac{A_{12}}{\rho_{11}^2}+\frac{R_{231}^2}{\rho_{11}^2\rho_{33}}, & B_{13} &= \frac{A_{13}}{\rho_{11}^2}+\frac{R_{123}^2}{\rho_{11}^3},\\
B_{31} &= \frac{A_{31}}{\rho_{33}^2}+\frac{R_{231}^2}{\rho_{11}\rho_{33}^2}, & B_{44} &= \frac{A_{44}}{\rho_{11}\rho_{33}}-\frac{1}{2}\frac{R_{123}R_{231}}{\rho_{11}^2\rho_{33}}.
\end{aligned}\right\} \qquad (3)$$

Table 3 lists values of these magnetoconductivity coefficients. Graphs against $\log T$ of $\log \sigma_{ij}$ give slopes of $-1{\cdot}4$, of $\log P_{ijk}$ give $-3{\cdot}0$ and of $\log B_{ij}$ give $-4{\cdot}3$. This is a reflection of a carrier mobility-temperature dependence close to $T^{-1{\cdot}5}$, since basically $\sigma_{ij} = f(\mu, \upsilon)$, $P_{ijk} = f(\mu^2, \upsilon^2)$ and $B_{ij} = f(\mu^3, \upsilon^3)$. This point is amplified later.

TABLE 3. THE VALUES OF THE TWELVE MAGNETOCONDUCTIVITY COEFFICIENTS CALCULATED FROM TABLE 1 USING EQUATIONS (3)

	conductivity		inverse Hall		magnetoconductivity							
temp. (°K)	σ_{11}	σ_{33}	$-P_{231}$	$-P_{123}$	B_{13}	B_{31}	$-B_{44}$	B_{11}	B_{12}	B_{33}	$-B_{24}$	$-B_{42}$
305	3·73	2·93	2·3	16·0	2·0	0·72	0·24	0·35	0·78	0·50	0·25	0·10
250	4·76	3·82	4·3	28	4·8	1·68	0·60	0·79	1·88	1·14	0·50	0·23
215	5·92	4·88	7·4	46	10·0	3·3	1·20	1·69	4·0	2·18	0·96	0·47
175	7·75	6·58	13·6	82	24	8·4	2·8	4·0	9·7	5·5	2·5	1·04
125	12·3	10·9	35	220	102	38	13·1	17·9	43	23·9	9·0	5·2
77	27·5	25·3	131	1120	1070	430	150	197	470	256	87	56
approx. error (%)	3	3	10	10	10	10	20	10	10	10	20	20

Units: conductivity, $10^4\ \Omega^{-1}\ \mathrm{cm}^{-1}$; inverse Hall, $10\ \Omega^{-1}\ \mathrm{cm}^{-1}\ \mathrm{kG}^{-1}$; magnetoconductivity, $\Omega^{-1}\ \mathrm{cm}^{-1}\ \mathrm{kg}^{-2}$.

7. COMPUTATION AND SOLUTION

There are nine band parameters to the multivalley ellipsoidal model of the Fermi surface: total carrier density, $N(=P)$; three electron mobilities along the axes of each electron ellipsoid (μ_1, μ_2, μ_3) corresponding hole mobilities (υ_1, υ_2, υ_3) and the

ellipsoid tilt angles (ψ_e, ψ_h) having cosines (C_e, C_h) and sines (S_e, S_h). The equations connecting these variables to the magnetoconductivity coefficients were originally derived by Drabble & Wolfe (1956). The important assumptions are independent contributions to electric current from each valley and an isotropic relaxation time in k-space. The equations are

$$\sigma_{11} = Ne\{(\mu_1 + C_e^2\mu_2 + S_e^2\mu_3) + (\upsilon_1 + C_h^2\upsilon_2 + S_h^2\upsilon_3)\}/2,$$
$$\sigma_{33} = Ne\{(S_e^2\mu_2 + C_e^2\mu_3) + (S_h^2\upsilon_2 + C_h^2\upsilon_3)\},$$
$$-P_{231} = Ne[\{\upsilon_2\upsilon_3 + \upsilon_1(S_h^2\upsilon_2 + C_h^2\upsilon_3)\} - \{\mu_2\mu_3 + \mu_1(S_e^2\mu_2 + C_e^2\mu_3)\}]/2c,$$
$$-P_{123} = Ne[\{\upsilon_1(C_h^2\upsilon_2 + S_h^2\upsilon_3)\} - \{\mu_1(C_e^2\mu_2 + S_e^2\mu_3)\}]/c.$$

The rest of the equations are written more conveniently by including only the electron terms, those of the holes being identical in form and simply added on:

$$B_{13} = Ne(\mu_1 + C_e^2\mu_2 + S_e^2\mu_3)\{\mu_1(C_e^2\mu_2 + S_e^2\mu_3)\}/2c^2,$$
$$B_{31} = Ne(S_e^2\mu_2 + C_e^2\mu_3)\{\mu_2\mu_3 + \mu_1(S_e^2\mu_2 + C_e^2\mu_3)\}/2c^2,$$
$$-B_{44} = Ne(S_e^2\mu_2 + C_e^2\mu_3)\{\mu_1(C_e^2\mu_2 + S_e^2\mu_3)\}/2c^2,$$
$$B_{11} = Ne\{S_e^2\mu_2(\mu_1 - \mu_3)^2 + C_e^2\mu_3(\mu_1 - \mu_2)^2 + 3C_e^2S_e^2\mu_1(\mu_2 - \mu_3)^2\}/8c^2,$$
$$B_{12} = Ne\{3S_e^2\mu_2(\mu_1^2 + \mu_3^2) + 3C_e^2\mu_3(\mu_1^2 + \mu_2^2) + C_e^2S_e^2\mu_1(\mu_2 - \mu_3)^2 + 2\mu_1\mu_2\mu_3\}/8c^2,$$
$$B_{33} \equiv (-B_{12} + 3B_{11} - 2B_{44})/2 = NeC_e^2S_e^2\mu_1(\mu_2 - \mu_3)^2/c^2,$$
$$B_{24} = NeC_eS_e\mu_1(\mu_2 - \mu_3)(-\mu_1 + C_e^2\mu_2 + S_e^2\mu_3)/4c^2,$$
$$B_{42} = NeC_eS_e(\mu_2 - \mu_3)\{\mu_2\mu_3 - \mu_1(S_e^2\mu_2 + C_e^2\mu_3)\}/4c^2.$$

Carrier densities and all mobilities are defined to be positive. μ_1 and υ_1 are directed along the binary axis; μ_2, μ_3 and υ_2, υ_3 are along the other ellipsoid axes in the mirror plane. ψ_e and ψ_h are defined as the tilt of μ_3 and υ_3 away from the trigonal axis. The set of operations $C \rightleftarrows S$, $\mu_2 \rightleftarrows \mu_3$, $\upsilon_2 \rightleftarrows \upsilon_3$ corresponds to a transformation between the two x–y–z sets mentioned earlier, when B_{24} and B_{42} change sign and all other coefficients are unchanged. The equations apply equally well to three or six ellipsoids; since the contributions are additive, the number of carriers per pocket is obtained by dividing N by three or six respectively. The task now remaining is to solve the twelve equations for the nine band parameters and compare N, ψ_e and ψ_h with the Fermi surface data of other workers.

Although theoretically possible, a direct solution by eliminating unknowns is not practicable. Even a small error in the measured value of a magnetoconductivity coefficient is magnified greatly by the complexity of the terms involved. The method developed by Freedman & Juretschke (1961) relies on obtaining an exact solution to eight equations incorporating nine of the twelve coefficients and then recalculating to find a self-consistent fit all round. This technique is inherently biased in favour of fitting certain coefficients. If it were possible that the ellipsoidal band model and assumptions were completely true, this would be acceptable. To obtain a fairer assessment of the experimental data, a computer program producing a least-mean-squares best fit to all twelve coefficients was devised.

Consider the overdetermined case of three equations in two unknowns:

$$A = f_1(x, y); \quad B = f_2(x, y); \quad C = f_3(x, y).$$

Define $$M = [(f_1 - A)^2 + (f_2 - B)^2 + (f_3 - C)^2].$$

If all three equations are exact, x and y exist such that

$$f_1 - A = f_2 - B = f_3 - C = 0$$

and therefore $M = 0$. If the equations are approximate, then best values of x and y may be found by minimizing M. Figure 6 illustrates how this may be accomplished (Hawgood 1965). The contours are of different values of M, and represent a 'pit'.

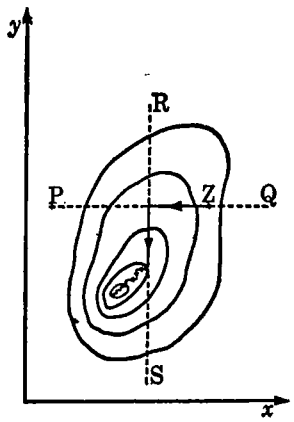

FIGURE 6. The technique used to find a solution to the equations. The contours represent different values of M (after Hawgood 1965).

The bottom of the pit is either at $M = 0$ so that its coordinates are the exact solution of the equations, or at a local minimum in M and its coordinates represent the best approximation locally to a solution. Suppose an approximate solution has been found or an arbitrary solution chosen (point Z). Then x is varied, keeping y constant, to slide across the cross-section PQ until M is minimized. Next this procedure is performed for y, keeping x constant (RS). Repetition produces a path that zigzags in towards the pit bottom. At each stage the lowest point on the cross-section may be located by recalculating M as the variable (x or y) is incremented stepwise. Alternatively differentiation could be used. Convergence could be speeded considerably by calculating the gradient vector and proceeding along the path of steepest descent. But this is a complex procedure for the many-dimensional case and was not adopted.

The extension of the method to the nine dimensions of the equations (4) is trivial. Each of the twelve coefficients is calculated, by inserting an arbitrary set of parameters into the equations (4), divided by the corresponding experimental value and then compared to unity to compute a parameter $SUMSQ$ (i.e. M), which is minimized

$$SUMSQ = \sum_{\sigma, P, B} \left[\frac{\text{calculated coefficient}}{\text{measured coefficient}} - 1{\cdot}0\right]^2$$

σ_{ij} and P_{ijk} were weighted because of the smaller experimental error of these coefficients. If *SUMSQ* could be made equal to zero, then all the calculated coefficients would equal their measured values and a perfect solution would have been found. A large computer (IBM 360/67) was used. Each evaluation of the set of equations took only 1 ms; 500 cycles of the nine variables were executed at each temperature. All six temperatures were analysed in a total time of 3 min. To test the program, the results for antimony (Öktü & Saunders 1967) were reassessed. Improved fits to the experimental coefficients resulted (Heavons & Saunders unpublished).

To ensure that all solutions have been found, a range of the parameters that start the calculation (point Z of figure 6) must be tried. Only one acceptable solution, that given in table 4, was obtained; convergence to this solution was rapid from widely different starting points. The quality of the fit of this solution is illustrated by the set of ratios of calculated to measured coefficients (table 5). Three other fits to the equations were readily rejected for the following reasons:

1. A higher residual value of *SUMSQ* indicated a poorer fit than the result given in table 4.

TABLE 4. BAND PARAMETERS OF ARSENIC, ASSUMING ELLIPSOIDAL ENERGY BANDS
SUMSQ ASSESSES THE DEGREE OF APPROXIMATION OF THE SOLUTION

temp. (°K)	N	μ_1	μ_2	μ_3	ψ_e	v_1	v_2	v_3	ψ_h	*SUMSQ*
305	2·16	460	40	550	−8°	1210	50	680	−50°	0·307
250	2·04	650	50	740	−8°	1570	85	950	−50°	0·274
215	2·03	840	25	950	−8°	1960	120	1220	−50°	0·258
175	1·98	1170	24	1300	−8°	2550	180	1700	−50°	0·257
125	1·90	2020	16	2240	−8°	4140	340	2880	−50°	0·248
77	1·92	4600	0	5300	−8°	8700	830	6600	−51°	0·230

Units: N, 10^{20} cm^{-3}; μ, v, cm^2 V^{-1} s^{-1}; ψ, degrees.

TABLE 5. THE RATIOS OF CALCULATED TO MEASURED COEFFICIENTS FOR THE SOLUTION GIVEN IN TABLE 4. NOTE THE SYSTEMATIC DEVIATIONS FROM UNITY OF EACH COEFFICIENT OVER THE WHOLE TEMPERATURE RANGE

	temperature (°K)					
coefficient	305	250	215	175	125	77
σ_{11}	0·99	0·99	0·99	0·99	0·99	1·00
σ_{33}	1·00	1·00	1·00	1·00	1·00	1·00
$-P_{231}$	0·99	0·99	0·99	0·99	0·99	0·99
$-P_{123}$	1·04	1·04	1·04	1·05	1·05	1·04
B_{13}	0·71	0·70	0·70	0·70	0·69	0·70
B_{31}	0·66	0·70	0·72	0·72	0·76	0·79
$-B_{44}$	1·21	1·22	1·21	1·22	1·21	1·25
B_{11}	1·03	1·04	1·03	1·00	0·98	0·95
B_{12}	1·08	1·07	1·07	1·07	1·05	1·00
B_{33}	0·82	0·84	0·85	0·85	0·85	0·87
$-B_{24}$	1·07	1·06	1·06	1·06	1·06	1·07
$-B_{42}$	1·05	1·03	1·04	1·06	1·08	1·07

2. The electron tilt angle showed no agreement at all with the value found by Priestley *et al.* (1967).

3. Energy ellipsoids would have to be oblate rather than the expected prolate form.

TABLE 6. ELECTRON AND HOLE CONTRIBUTIONS TO THE MAGNETOCONDUCTIVITY COEFFICIENTS AT 305 °K (THE HOLES DOMINATE)

coefficient	electron contribution	hole contribution	total	calculated / measured
σ_{11}	$0{\cdot}89 \times 10^4$	$2{\cdot}82 \times 10^4$	$3{\cdot}71 \times 10^4$	0·99
σ_{33}	$1{\cdot}88 \times 10^4$	$1{\cdot}06 \times 10^4$	$2{\cdot}94 \times 10^4$	1·00
$-P_{231}$	−47·4	+70·0	+22·5	0·99
$-P_{123}$	−8·5	+175	+167	1·04
B_{13}	0·021	1·43	1·45	0·71
B_{31}	0·257	0·214	0·472	0·66
$-B_{44}$	0·023	0·268	0·291	1·21
B_{11}	0·043	0·317	0·361	1·03
B_{12}	0·161	0·687	0·849	1·08
B_{33}	0·008	0·401	0·409	0·82
$-B_{24}$	0·011	0·258	0·270	1·07
$-B_{42}$	0·014	0·090	0·104	1·05

The solution shown in table 4 presents, for the first time, detailed information of carrier densities and mobilities in arsenic over a wide temperature range. The invariance of the ellipsoid tilt angles with temperature (see table 4) is satisfying; the finding that carrier density is essentially temperature independent verifies degeneracy. The anomalous behaviour of μ_2 is not necessarily significant. As is shown in table 6, the electron contribution to many coefficients is small; further, μ_2 is swamped by μ_1 and μ_3. An accurate value of μ_2 cannot be obtained.

8. CONCLUSIONS

The correspondence of the solution to Fermi surface details is summarized in table 7. The high mobilities (μ_1, μ_3; ν_1, ν_3) lie in the plane of minimum area of the Fermi pockets. The tilt of this minimum area is obtained by adding 90° to the tilts calculated from the equations (ψ_e, ψ_h); see figure 7. Considering the simplifications made for the model of the Fermi surface, agreement is surprisingly good. Other workers have measured tilt angles of similar values. We confirm the theoretical assignment (Lin & Falicov 1966) of electrons to the high-tilt and holes to the medium-tilt pockets. Electron inverse mobility ratios are compared with effective mass data to assess the validity of an isotropic relaxation time. In fact this assumption may be relaxed a little and $\boldsymbol{\tau}$ written as a tensor (Herring & Vogt 1956)

$$\boldsymbol{\mu} = e\boldsymbol{\tau}/\mathbf{m}^*.$$

Then the isotropic assumption is reasonable, if the tensor components are within 2:1. τ_1 and τ_3 for electrons are given in table 8. τ_2 cannot be assessed because μ_2 is

TABLE 7. A COMPARISON OF THE SOLUTION OF THE ELLIPSOIDAL MODEL TO PUBLISHED DETAILS OF THE FERMI SURFACE OF ARSENIC

	tilt angle			
	electron pockets		hole pockets	
	(minimum area)	(maximum area)	(minimum area)	carrier densities (cm^{-3})
pseudopotential calculation (Lin & Falicov 1966)	80°	171°	44°	—
de Haas–van Alphen effect (Priestley *et al.* 1967)	86°	171°	37°	$2{\cdot}12 \times 10^{20}$ (at 4·2 °K)
this work	82°	172°	40°	$2{\cdot}16 \times 10^{20}$ (at 305 °K) $1{\cdot}92 \times 10^{20}$ (at 77 °K)

Electron effective mass ratios, in ellipsoidal approximation (Priestley *et al.* 1967)

$$m_1 : m_2 : m_3 :: 1{\cdot}5 : 20 : 1.$$

Inverse electron mobility ratios (this work), $1/\mu_1 : 1/\mu_3$

temp (°K)	305	250	215	175	125	77
	1·2:1	1·14:1	1·13:1	1·11:1	1·13:1	1·15:1

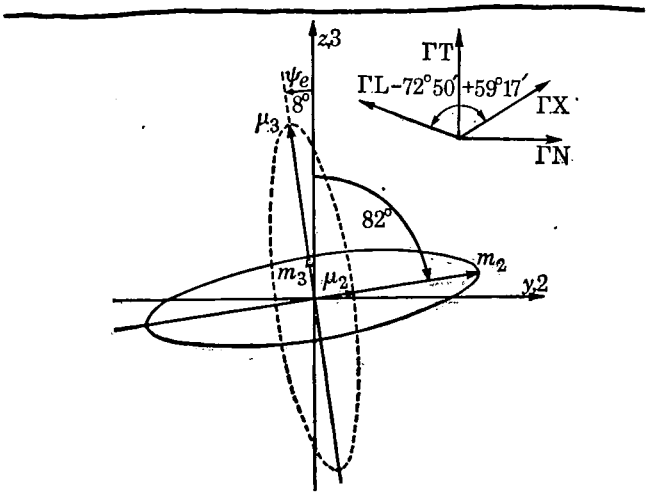

FIGURE 7. The relation between tilt angles of mobility (---) and energy (—) surfaces of the electrons. A tilt of 8° towards ΓL of the high mobility μ_3 is equivalent to a tilt of 82° towards ΓX of the direction normal to the plane of minimum area of the energy ellipsoid.

TABLE 8. VALUES OF RELAXATION TIMES IN ARSENIC CALCULATED FROM OUR MOBILITY DATA AND THE EFFECTIVE MASSES MEASURED BY PRIESTLEY ET AL. (1967) ASSUMING THE FORMULA $\mu_i = e\tau_i/m_i . \tau_2$ CANNOT BE ASSESSED AS μ_2 IS NOT KNOWN

	temperature (°K)					
relaxation times	305	250	215	175	125	77
electrons: τ_1	0·42	0·60	0·87	1·08	1·87	4·2
τ_3	0·33	0·44	0·56	0·77	1·33	3·25

Unit: 10^{-13} s.

not known accurately. The non-ellipsoidal nature of the hole pocket prevents any quantitative comparison of hole mobilities and effective masses. Indeed various mass data (Berlincourt 1955; Datars & Vanderkooy 1966; Tanuma, Ishizawa & Ishiguro 1966) show only qualitative consistency. But in general the low mobility, v_2, is in the heavy mass direction.

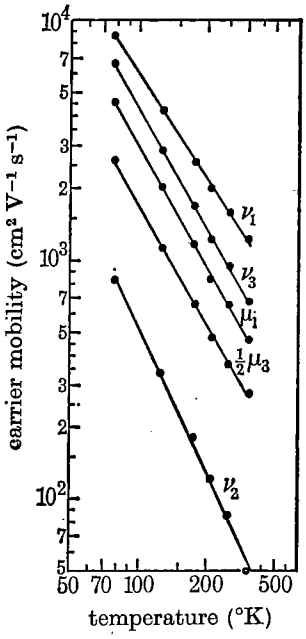

FIGURE 8. Mobility-temperature dependence. μ_1, μ_3 and v_3 show a slope of $-1{\cdot}7$. v_1 shows $-1{\cdot}5$ and v_2 $-2{\cdot}0$. The values of μ_3 are halved to avoid confusion of points.

Figure 8 shows the temperature dependence of the mobilities. The temperature exponent of $-1{\cdot}7$ for μ_1, μ_3, v_3 is even further from the expected $-1{\cdot}0$ than that of antimony ($-1{\cdot}5$). It is clear now that the formula for scattering in a semimetal, $\tau = AT^{-1}E^{-\frac{1}{2}}$ (Wilson 1953) is insufficient. Additional scattering, of an intervalley nature, seems the most probable answer. Because of the low carrier densities and thus the small Fermi surface compared to the metallic case, Wilson assumed only intravalley scattering of carriers by long-wavelength (small-wavenumber) phonons. Intervalley scattering requires relatively high energy, large-k phonons. These are few in number at low temperatures, but as temperature rises their population, and thus the contribution to carrier scattering, increases so that carrier mobility falls faster than the simple formula indicates. Herring (1955) has analysed this situation for non-degenerate multivalley semiconductors; the mobility-temperature exponent can increase from $-1{\cdot}5$ up to $-2{\cdot}5$ depending mainly on the proportion of inter- to intra-valley scattering.

It may be seen from table 5 that consistent discrepancies exist for B_{13}, B_{31}, B_{44} and B_{33}. Assuming no systematic experimental error, these discrepancies plausibly reflect the most significant departure of the Fermi surface from ellipsoidal shape:

the 'necks' which contain low mass holes. Despite the low number of carriers in these 'necks' compared to the main pockets, some B_{ij} may be significantly affected because of their dependence on the cubes of considerably higher mobilities. A three-band fit to the magnetoconductivity coefficients is now in hand.

Maltz & Dresselhaus (1968) have examined the band structure of arsenic from magnetoreflectivity in the infrared; they report disagreement with a theoretical band gap at T. It has already been observed (Priestley *et al.* 1967) that the theoretical effective masses and Fermi energy do not agree at all well with experiment and that

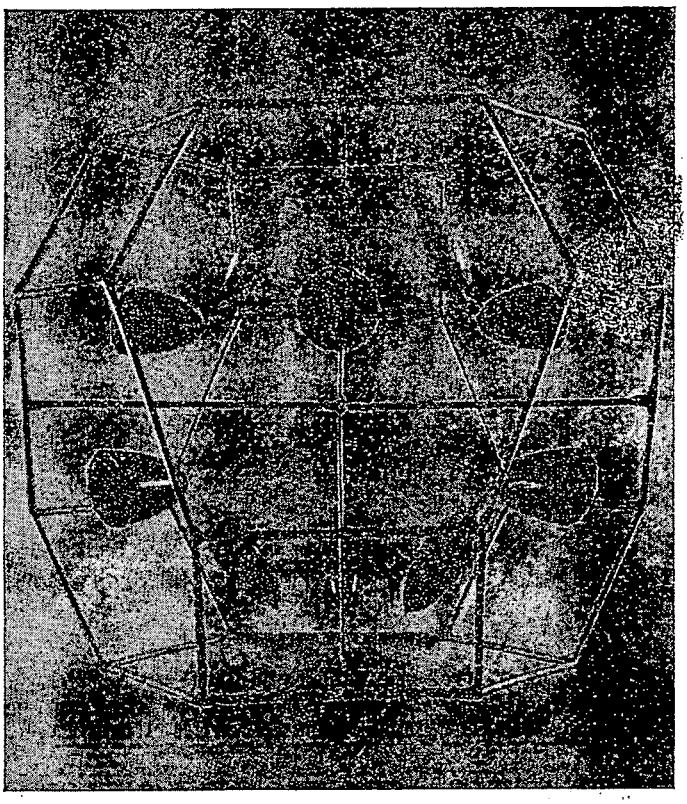

FIGURE 9. The ellipsoidal model of the Fermi surface of arsenic deduced from the galvanomagnetic effects. The photograph is taken in the bisectrix direction. The six half-ellipsoids (dark colour) are the electron pockets and six full ellipsoids (light colour) are the hole pockets.

the theoretical surface fails to explain one hole period (the 'δ' oscillation). Figure 9 shows the complete ellipsoidal Fermi surface deduced from the galvanomagnetic effects, located in the Brillouin zone. Apart from the hole necks, overall close agreement is manifest between this model and data from the de Haas–Van Alphen effect. A further success of the ellipsoidal approximation of the Fermi surface is the agreement between the calculated value (0·192 mJ mole^{-1} °K^2, Priestley *et al.* 1967) and measured value (0·194 ± 0·007, Culbert 1967; 0·186 ± 0·002, Taylor *et al.* 1967)

T END OF FIGURE CAPTION:

Surfaces are not ellipsoids of revolution

of the temperature coefficient, γ, of the electronic specific heat. Possibly the warping of the hole pockets is less pronounced than that proposed by Lin & Falicov (1966).

References

Abeles, B. & Meiboom, S. 1956 *Phys. Rev.* **101**, 544.
Berlincourt, T. G. 1955 *Phys. Rev.* **99**, 1716.
Bridgman, P. W. 1932/33 *Proc. Am. Acad. Sci.* **68**, 39.
Cohen, M. H., Falicov, L. M. & Golin, S. 1964 *IBM J. Res. Dev.* **8**, 215.
Culbert, H. 1967 *Phys. Rev.* **157**, 560.
Datars, W. R. & Vanderkooy, J. 1966 *J. Phys. Soc. Japan* **21**, 657.
Drabble, J. R. & Wolfe, R. 1956 *Proc. Phys. Soc.* B **69**, 1101.
Epstein, S. & Juretschke, H. J. 1963 *Phys. Rev.* **129**, 1148.
Falicov, L. M. & Golin, S. 1965 *Phys. Rev.* **137**, A 871.
Falicov, L. M. & Lin, P. J. 1966 *Phys. Rev.* **141**, 562.
Faulkner, E. A., McGlashan, M. L. & Stubley, D. 1965 *J. Chem. Soc.* Part II, 2837.
Freedman, S. J. & Juretschke, H. J. 1961 *Phys. Rev.* **124**, 1379.
Golin, S. 1965 *Phys. Rev.* **140**, A 993.
Hawgood, J. 1965 *Numerical methods in Algol*, p. 72. London: McGraw-Hill.
Herring, C. 1955 *Bell Syst. Tech. J.* **34**, 237.
Herring, C. & Vogt, E. 1956 *Phys. Rev.* **101**, 944.
Jeavons, A. P. & Saunders, G. A. 1968 *Br. J. appl. Phys.* (*J. Phys. D*), Ser. 2, **1**, 869.
Jones, H. & Zener, C. 1934 *Proc. Roy. Soc.* A **145**, 268.
Juretschke, H. J. 1955 *Acta Crystallogr.* **8**, 716,
Kapitza, P. 1929 *Proc. Roy Soc.* A **123**, 292.
Ketterson, J. B. & Eckstein, Y. 1965 *Phys. Rev.* **140**, A 1355.
Lin, P. J. & Falicov, L. M. 1966 *Phys. Rev.* **142**, 441.
Maltz, M. & Dresselhaus, M. S. 1968 *Phys. Rev. Lett.* **20**, 919.
McLennan, J. C., Niven, C. D. & Wilhelm, J. O. 1928 *Phil. Mag.* **6**, 666.
Öktü, Ö. & Saunders, G. A. 1967 *Proc. Phys. Soc.* **91**, 156.
Palmer, T. M. 1966 *Elect. Engng* **38**, 467.
Priestley, M. G., Windmiller, L. R., Ketterson, J. B. & Eckstein, Y. 1967 *Phys. Rev.* **154**, 671.
Sybert, J. R., Mackey, H. J. & Hathcox, K. L. 1968 *Phys. Rev.* **166**, 710.
Tanuma, S., Ishizawa, Y. & Ishiguro, S. 1966 *J. Phys. Soc. Japan* **21**, suppl. 662.
Taylor, J. B., Bennett, S. L. & Heyding, R. D. 1965 *J. Phys. Chem. Solids* **26**, 69.
Taylor, W. A., McCollum, D. C., Passenheim, B. C. & White, H. W. 1967 *Phys. Rev.* **161**, 652.
Wilson, A. H. 1953 *The theory of metals*, p. 264. Cambridge University Press.
Windmiller, L. R. 1966 *Phys. Rev.* **149**, 472.